

Chapter 2

General Properties of Bulk SiC

The fabrication and properties of silicon carbide crystals have been extensively studied because as a wide bandgap semiconductor, silicon carbide is ideal for electronic applications requiring high temperature, high frequency, and high power. The electrical and electronic properties as well as device applications of bulk silicon carbide have been reviewed [1–3]. In this chapter, which provides a self-contained framework to facilitate the understanding of the properties of silicon carbide nanostructures, the basic properties of silicon carbide crystals are reviewed.

2.1 SiC Polytypes

Similar to silicon, silicon carbide is a covalently bonded semiconductor. In the crystalline form, each silicon atom is covalently bonded to four neighboring carbon atoms to form a tetrahedron (Fig. 2.1) and vice versa. There are two types of tetrahedrons in the silicon carbide crystal. The first type is obtained by rotating another tetrahedron along its c -axis by 180° , and one type of tetrahedron is the mirror image of the other when the c -axis is parallel to the mirror. The c -axis denotes the direction normal to the Si–C double-atomic layers. In each layer, the silicon (or carbon) atoms have a close-packed hexagonal arrangement. There are three types of sites (named A , B , C) in arranging the Si–C double-atomic layers, and each layer is normal to the c -axis (Fig. 2.2).

The three types of double-atomic layers A , B , and C form a periodical series with a specified repeating unit along the c -axis forming a specific polytype of the silicon carbide crystal. For example, in 3C-SiC (Fig. 2.3), the stacking sequence of the double-atomic layers is ABCABC... The letter “C” in “3C-SiC” denotes the cubic crystal structure and “3” refers to the number of double-atomic layers in one repeating unit (ABC). 3C-SiC is the only polytype with the cubic crystal structure

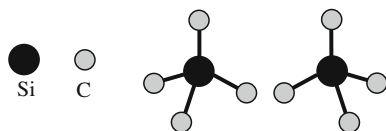


Fig. 2.1 Two types of tetrahedrons forming the building blocks of all SiC crystals with each tetrahedron consisting of one Si atom and four covalently bonded nearest-neighboring C atoms. One type is obtained by rotating another type around its c -axis (vertical here) by 180°

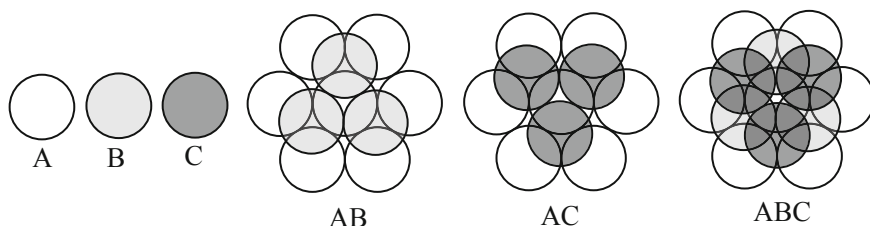


Fig. 2.2 Three types (A, B, C) of Si-C double-atomic layer arrangement along the c -axis (stacking direction) through close-packed spheres. The c -axis is normal to the paper plane

that is also referred to as β -SiC. The dominant polytypes in silicon carbide are hexagonal. The three most common hexagonal polytypes are 2H, 4H, and 6H and their stacking sequences are ABAB..., ABCBACB..., and ABCACBAB-CACB..., respectively. Similarly, “H” refers to the hexagonal crystal structure and the number before “H” denotes the number of double-atomic layers in one repeating unit. There are other types of silicon carbide crystals, for instance, 15R-SiC where “R” stands for the rhombohedral crystal structure. It should be noted that one Si (or C) atomic layer in the stacking sequence can have a local cubic (k) or hexagonal (h) environment with respect to the immediate neighbors, as shown in Fig. 2.3. 3C-SiC has only k -type atoms, and 2H-SiC has only h -type atoms. The atomic number ratio $k:h$ is 1:1 in 4H-SiC and 2:1 in 6H-SiC.

As a result of the different stacking sequence of the double-atomic layers, different polytypes of silicon carbide have distinct electronic structures as well as electrical and optical characteristics. For instance, the indirect bandgaps at room temperature of 3C-SiC, 6H-SiC, and 4H-SiC are 2.2 eV, 2.86 (or 3.02) eV, and 3.2–3.3 eV, respectively. The bandgap depends on the temperature and even the measured room-temperature bandgap of a specific polytype may vary in a small range depending on the uncertainty in determining the optical absorption edge and measurement conditions in different laboratories.

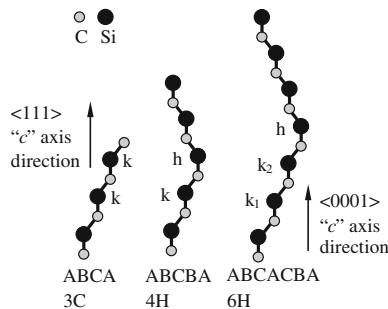


Fig. 2.3 Si–C double-atomic layer arrangement in the three most common polytypes of SiC. The c -axis denotes the stacking direction and k and h denote atoms with the localized cubic and hexagonal crystal symmetry, respectively

2.2 Interstellar Origin

SiC can be produced on earth and also found in outer space. For example, presolar SiC grains have been found in meteorites. Their morphology has been extensively studied by electron microscopy and the elemental and isotopic compositions analysis by mass spectrometry.

Including silicon carbide, five types of presolar matters have been identified in chondrites, namely diamond (about 2.6 nm), graphite (0.8–7 μm), silicon carbide (0.05–20 μm), silicon nitride, and aluminum oxide [4]. The anomalous isotopic compositions of Si, C, O, and N demonstrate that the grains have a presolar origin. Studies on presolar diamond, graphite, and silicon carbide in chondrites show that the abundance is correlated with the chemical and physical properties of the meteorites [5, 6]. Among the various types of presolar grains, silicon carbide grain is the most extensively studied because it contains many elements including minor and trace elements. The strontium isotopic composition determined from individual circumstellar SiC grains extracted from the Murchison meteorite by resonant ionization mass spectrometry confirms the grain origin of s -process nucleosynthesis at moderate neutron densities [7].

The polytype distribution of circumstellar SiC has been identified by transmission electron microscopy on presolar silicon carbide in the Murchison carbonaceous meteorite [8]. Only 3C-SiC and 2H-SiC and their intergrowth have been observed (Fig. 2.4). It has been speculated that the structural simplicity results from the low pressure in the circumstellar outflow and corresponding low silicon carbide condensation temperature.

Much effort has been made to explore the origin of the SiC grains. The barium isotopic anomaly observed from SiC meteorite grains is considered to stem from the s -process nucleosynthesis in carbon stars that suffer recurrent He shell instability on the asymptotic giant branch (AGB) [9]. Additionally, the Xe, Nd, and Sm anomalies in the same SiC grains show clearly the s -signature and the

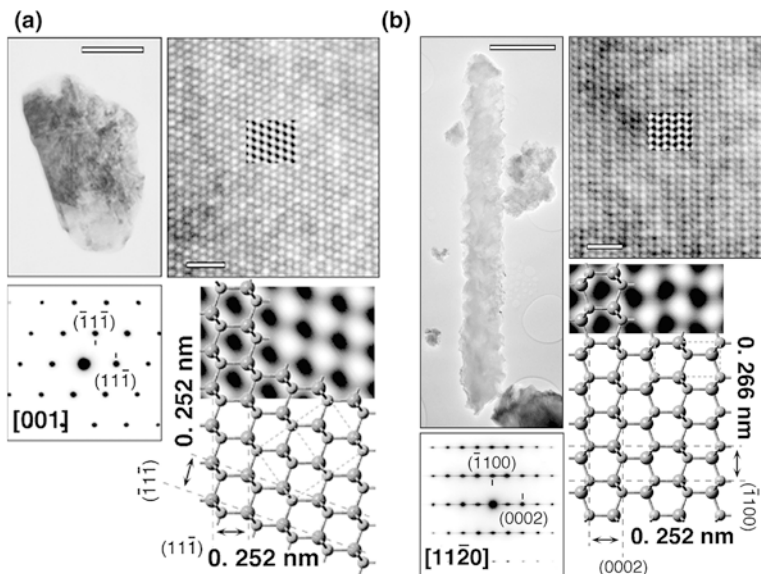


Fig. 2.4 Circumstellar 3C-SiC (a) and 2H-SiC (b) from Murchison carbonaceous chondrite KJE. Each panel contains the TEM image (*top left*, scale bar: 0.1 μm), selected-area electron diffraction (SAED) pattern (*bottom left*), high-resolution TEM (HRTEM) image (*top right*, scale bar: 1 nm), and atomic model of the [011] (for 3C-SiC) or [1120] (for 2H-SiC) zone axis superimposed on a simulated lattice image (*bottom right*). The tetrahedral stacking direction in the HRTEM image and atomic model is horizontal. Reprinted with permission from [8]. Copyright 2003, AAAS

corresponding interpretation corroborates the carbon-star origin. Another group has studied the isotopic compositions of the carbon, nitrogen, magnesium, silicon, and titanium in the single interstellar silicon carbide grains (with sizes 1–10 μm) extracted from the Murchison carbonaceous chondrite [10]. Scanning electron microscopy (SEM) images of these SiC grains are displayed in Fig. 2.5. All the grains exhibit crystalline features but their morphology varies from euhedral to a fine-grained surface, indicating agglomerates of smaller subgrains. Although many grains possess the hexagonal (Fig. 2.5b) and tetrahedral (Fig. 2.5c) shape, electron diffraction and Raman scattering indicate that the grains are β-SiC. The C and N isotopic compositions along with *s*-process Kr, Xe, Ba, and Nd suggest that the AGB or Wolf-Rayet stars are possible sources of the SiC grains. However, the existing models of nucleosynthesis in these stellar sites cannot account for the details of all the observed isotopic compositions.

The isotopic ratios of 124 presolar SiC grains of types A and B (defined as having $^{12}\text{C}/^{13}\text{C} < 10$) in an acid-resistant residue of the Murchison carbonaceous meteorite along with that of 28 previously analyzed A + B grains have been studied [11]. The most likely sources of the A + B grains with solar *s*-process abundance are J-type carbon stars although the origin of these stars is still unclear. Born-again AGB stars are possible sources of the A + B grains with enhanced

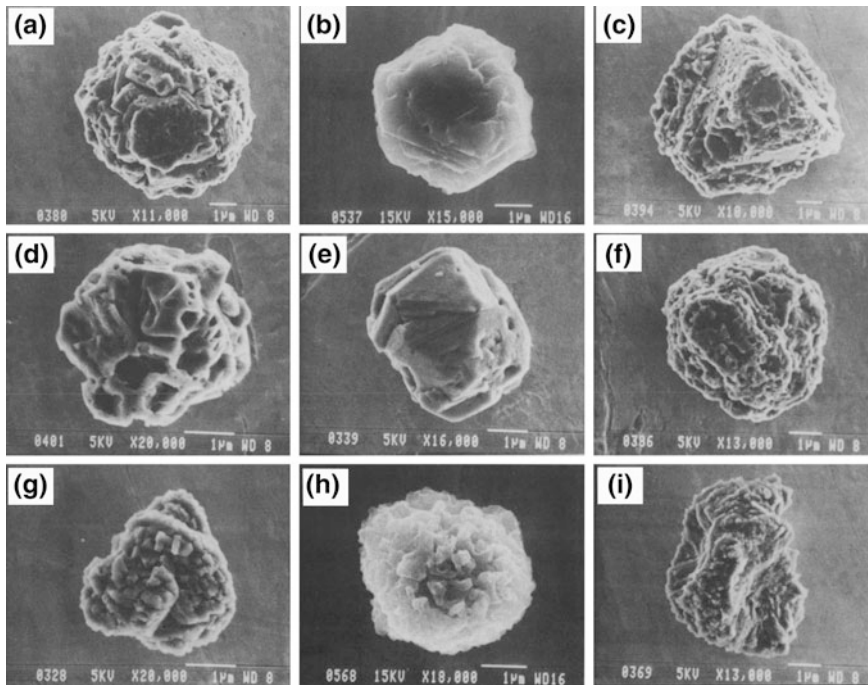
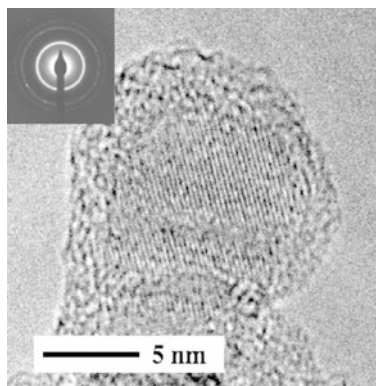


Fig. 2.5 Scanning electron microscopy images of SiC grains extracted from Murchison carbonaceous chondrites KLG (**b** and **h**) and KJH (**a**, **c**, **d**, **e**, **f**, **g**, and **i**). The grains show crystalline features. The morphology varies from euhedral (**a**, **b**, **c**, and **e**) to fine-grained surface indicating agglomerates of smaller subgrains (**g**, **h**, and **i**). Many grains have the hexagonal (**b**) and tetrahedral (**c**) shape. Electron diffraction and Raman scattering studies indicate that the grains are β -SiC. Reprinted with permission from [10]. Copyright 1994, IOP Publishing/on behalf of American Astronomical Society

s-process elemental abundance. In a comparative study, the strontium, zirconium, molybdenum, and barium isotopic compositions predicted for the mass-losing envelopes of AGB stars of solar metallicity and mass 1.5, 3, and $5 M_{\odot}$ are compared with the measurements of single presolar SiC grains from the Murchison meteorite [12]. The predicted isotopic compositions in the envelopes of low-mass AGB stars of solar metallicity agree with the isotopic ratios determined from individual presolar SiC grains, whereas the prediction for intermediate mass stars excludes them as the source of these grains. A multiplicity of low-mass AGB stars with metallicity close to that of the sun with different mass and neutron exposure is required to explain the measured spread in the heavy element isotopic compositions among single presolar SiC grains.

The individual β -SiC nanoparticles with average diameters of 10–20 nm (Fig. 2.6) have been synthesized by laser-induced pyrolysis of gas-phase starting materials [13]. The infrared spectra perfectly match the absorption or emission band profile of the $11 + \mu\text{m}$ feature observed from carbon-rich AGB stars conducted by the *Infrared Space Observatory*. The 7.5–13.5- μm infrared spectra of

Fig. 2.6 High-resolution TEM image of one particle showing the β -SiC core as determined by the lattice fringe spacing and electron diffraction pattern (*inset*). Reprinted with permission from [13]. Copyright 2003, IOP Publishing/on behalf of American Astronomical Society



32 identified or potential carbon stars have been investigated [14]. Four carbon stars, including AFGL 3068, IRAS 02408 + 5458, AFGL 2477, and AFGL 5625, show the 11- μm SiC feature in absorption. Figure 2.7 shows the self-absorption fits of the infrared absorption spectra of two carbon stars. All of the observed SiC features can be fitted well by α -SiC grains. The observation shows no unambiguous evidence of the presence of β -SiC around these stars. This result seems abnormal since β -SiC is the most commonly observed polytype in meteorites.

Although many studies have suggested that the carbon stars are the sources of SiC grains, other investigations point out that the SiC grains in the meteorites may originate from supernovae. The C, N, Si, Mg–Al, Ca, and Ti isotopic compositions of five single SiC grains 2–9 μm in size extracted from the Murchison carbonaceous meteorite have been determined by ion microprobe [15]. The Ca and Ti anomalies suggest their origin of explosive nucleosynthesis in supernovae and the in situ decay of the radioactive precursors ^{44}Ti and ^{49}V in SiC grains can form in the supernova ejecta. However, no simple formation mechanism can provide a consistent explanation of the isotopic compositions of those grains. Large excess of ^{44}Ca arising from the radioactive decay of short-lived ^{44}Ti , and in ^{46}Ti , ^{49}Ti , and ^{50}Ti has been observed from four graphite grains and five type-X SiC grains extracted from the Murchison meteorite [16]. These grains must have a supernova origin since ^{44}Ti is only produced in supernovae. Furthermore, the Si, C, N, Al, O, and Ti isotopic compositions require a type II supernova source and suggest heterogeneous mixing of different supernova regions including the nickel core. By using secondary ion mass spectrometry, the isotopic compositions of C, N, O, and Si in 849 small (about 1 μm) individual SiC grains extracted from the Murchison meteorite have been determined [17]. The isotopic compositions of the major elements C and Si of most grains are similar to those observed from larger grains, suggesting an AGB star origin of these grains. Highly anomalous isotopic compositions have been found from a nitride grain that comprises Si_3N_4 with little carbon. The isotopic features of C, N, and Si resemble those of the rare type-X SiC grains, suggesting that these two rare constituents of circumstellar matters are formed in type II supernovae. In another study, the type-X SiC particles extracted chemically from meteorites are demonstrated to have chemical and isotopic

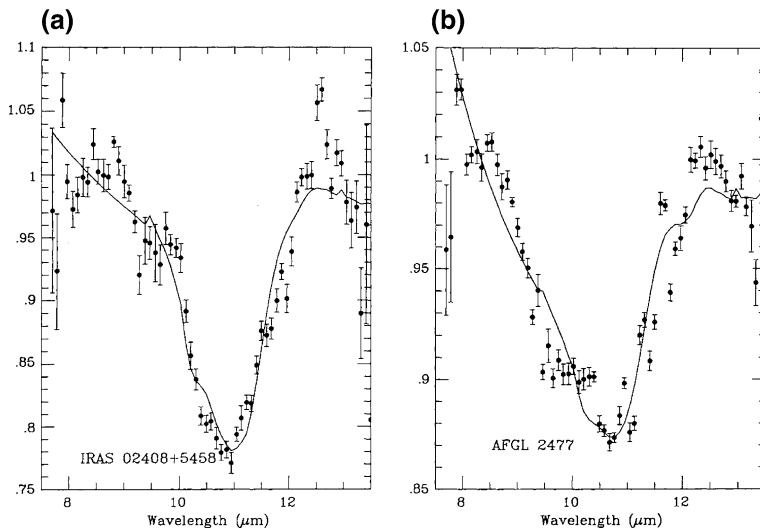


Fig. 2.7 Flux calibrated and normalized infrared spectra of two carbon stars **a** IRAS 02408+5458 and **b** AFGL 2477, showing absorption features with best χ^2 -fits using self-absorbed SiC. Reprinted with permission from [14]. Copyright 1997, Oxford University Press/on behalf of Royal Astronomical Society

compositions resembling those from explosive helium burning in ^{14}N -rich matter [18]. It is proposed that these particles are from type Ia supernovae that explode with a cap of helium atop their CO structure. The enhanced abundance of C and Si suggests that silicon carbide is in fact the natural condensate, and it is speculated that the dust grows within the interior of type Ia supernovae during expansion.

2.3 Electronic Structures

SiC is an indirect semiconductor with a wide bandgap. The most common polytypes, 3C, 6H, 4H, and 2H, have room-temperature bandgaps of 2.2 eV, 2.86 (or 3.02) eV, 3.2–3.3 eV, and 3.3 eV (exciton energy gap), respectively. Note that the bandgap subtracted by exciton binding energy is the exciton energy gap. The electronic structure of silicon carbide crystals has been extensively studied by empirical-pseudopotential, tight-binding, and first-principle methods.

The electronic band structures of the four polytypes (3C, 2H, 4H, and 6H) of silicon carbide are calculated using local atomic pseudopotentials for carbon and silicon [19]. The calculated indirect bandgaps of the 3C, 2H, 4H, and 6H polytypes are 2.40, 3.35, 2.80, and 2.45 eV, respectively. The indirect bandgap increases with increasing hexagonality of the polytype, and the trend is qualitatively consistent with experimental results. However, the calculated bandgaps of the 4H and 6H polytypes are significantly smaller than the reported experimental values. This

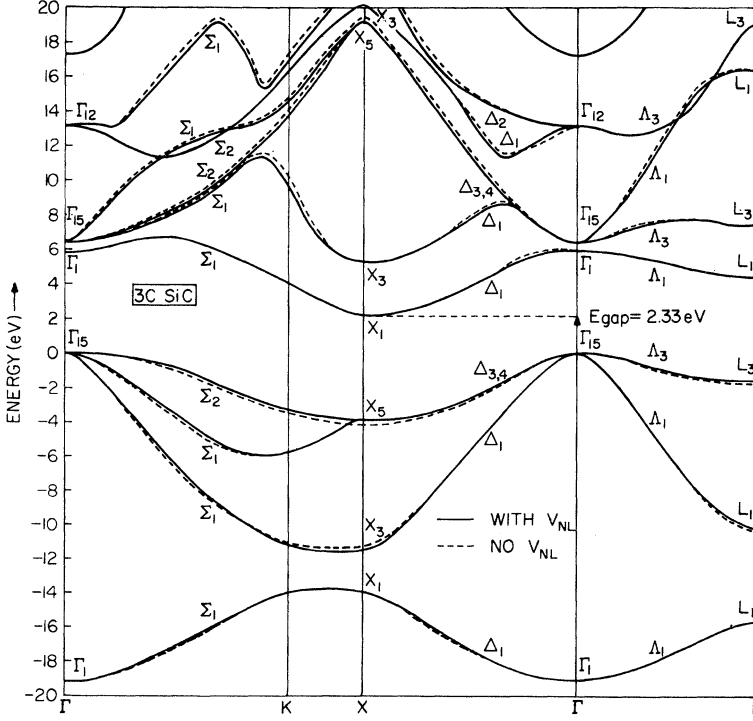


Fig. 2.8 Calculated electronic band structure of 3C-SiC with (solid line) and without (dashed line) inclusion of a nonlocal angular momentum-dependent potential in the pseudopotential. Reprinted with permission from [20]. Copyright 1972, American Physical Society

is because the energy levels in 4H- and 6H-SiC are calculated without further adjustment of the pseudopotentials, unlike the cases of 3C- and 2H-SiC. The calculated direct bandgaps at Γ differ relatively slightly among the four polytypes, and they are 5.14, 4.46, 4.60, and 4.40 eV for the 3C, 2H, 4H, and 6H polytypes. The energy band structure of 3C-SiC has been calculated by the nonlocal empirical-pseudopotential method [20], which shows that 3C-SiC is an indirect gap semiconductor with the valence-band maximum at Γ_{15v} and conduction-band minimum at X_{1c} (Fig. 2.8). The calculated threshold of the indirect transition is 2.33 eV corresponding to the Γ_{15v} - X_{1c} transition. This agrees well with the experimental value of 2.39 eV [21]. The threshold of the direct transition is 5.90 eV that corresponds to the Γ_{15v} - Γ_{1c} transition.

By interpreting the SiC polytypes as natural superlattices consisting of mutually twisted cubic layers, a method has been developed to calculate the electron band structure of any polytype based on an empirical-pseudopotential description of cubic SiC [22]. The indirect gaps of all SiC polytypes with hexagonality below 50 % are obtained. The calculated bandgaps of hexagonal and rhombohedral polytypes are in excellent agreement with experimental data (Table 2.1). The results also reveal the nearly linear relationship between the indirect gap and the

Table 2.1 Hexagonality and energy gaps (eV) of several SiC polytypes. Reprinted with permission from [22]. Copyright 1994, American Physical Society

Polytype (Ramsdell)	Polytype ABC	Hexagonality (percent)	Theory	Experiment
3C	ABC	0	2.40	2.390
10H	ABCABCACB	20	2.66	
8H	ABCABACB	25	2.76	2.80
6H	ABCACB	33.3	3.05	3.023
15R	ABCACBCABACACB	40	3.03	2.986
4H	ABCB	50	3.28	3.263
2H	AB	100	4.04	3.330

hexagonality, in agreement with experiments. 2H-SiC is an exception and its gap can be reproduced only with the proper choice of the interface position.

The electronic structure and wave function of 3C-SiC can be calculated using the first-principle Hartree–Fock–Slater model based on the discrete variational method [23]. The calculated first indirect gap is 2.5 eV that is close to the experimental value of 2.39 eV. The quasiparticle energy of 3C-SiC is evaluated using the first-principle density functional theory (DFT) by adopting the local density approximation (LDA) and nonlocal, norm-conserving pseudopotentials [24]. The localized Gaussian orbital basis sets are utilized. The self-energy operator is evaluated utilizing the *GW* approximation, and it provides energy correction to the LDA calculation. The calculated indirect bandgap is 2.33–2.35 eV that is in good agreement with the experimental value. Another theoretical calculation employing the density functional theory and local density approximation provides the electronic structures of 3C-, 6H-, 4H-, and 2H-SiC (Fig. 2.9) [25]. The calculated indirect bandgaps of 3C-, 6H-, 4H-, and 2H-SiC are 1.27, 1.96, 2.18, and 2.10 eV, respectively. The energy gap increases with increasing hexagonality with the exception of the 2H polytype. The calculation generally underestimates the transition energies in DFT-LDA. This matches the generally accepted notion that the DFT-LDA calculation generally underestimates the fundamental bandgap in semiconductors and insulators by 30–60 %. After introduction of the quasiparticle correction (1.13 eV) to the DFT-LDA band structures, the calculated indirect bandgaps agree with the experimental result. The full-potential linearized augmented-plane-wave method in the density functional theory and local density approximation including spin–orbit interaction has been employed to calculate the bandgaps of 3C-, 2H-, 4H-, and 6H-SiC [26, 27]. The calculated bandgaps are smaller than the measured values by about 1.1 eV. The shape of the bands is consistent with the results obtained from other types of calculation.

The self-consistent ab initio pseudopotential calculation of the electronic properties of 3C, 2H, 4H, and 6H SiC has been performed [28]. The calculated bandgaps are underestimated as well, ranging from 1.04 to 1.28 eV, as a result of the use of the LDA in the calculation. Different polytypes show similar valence-band widths, and

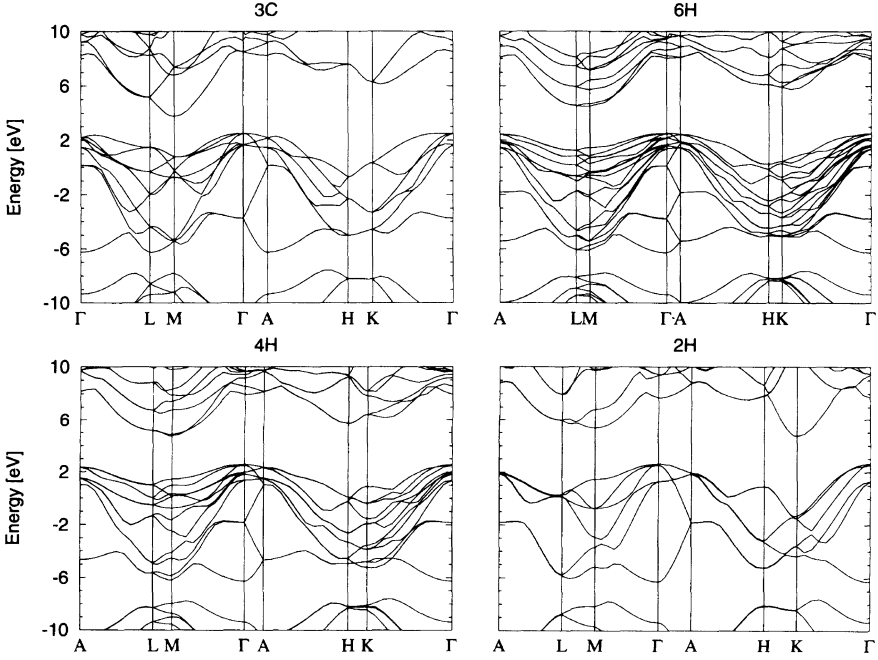


Fig. 2.9 Electronic band structures of 3C-, 6H-, 4H-, and 2H-SiC derived by the first-principle density functional theory using the local density approximation. Reprinted with permission from [25]. Copyright 1994, American Physical Society

they are 15.33, 15.37, 15.41, and 15.49 eV for 3C, 6H, 4H, and 2H polytypes, respectively. The valence-band width increases slightly with hexagonality. In contrast, the bandgap and conduction-band minimum vary significantly as the hexagonality increases. The electronic excitation properties of various SiC polytypes, 6H, 4H, 2H, and 3C, have been studied by combining the first-principle pseudopotential method in the framework of DFT-LDA and proper calculation of the quasiparticle effect [29]. The quasiparticle shifts added to the density functional eigenvalues are evaluated using a model dielectric function and an approximate treatment of the electron self-energy concerning local-field effects and dynamic screening. The calculated indirect bandgaps are in good agreement with the measured values, for instance, 2.59 and 3.25 eV for the 3C and 6H polytypes, respectively.

The dependence of the minimum bandgap and gaps at the relevant k -points on the hexagonality of the SiC polytypes have been summarized [30], as shown in Fig. 2.10. The minimum at K increases from 2H to 3C but shows some nonmonotonic oscillations for the lower-hexagonality polytypes. The dashed line in this figure indicates the well-known linear relationship between the minimum indirect bandgap and hexagonality. This law applies to all hexagonalities. This is the absolute minimum gap except the value very close to 100 % hexagonality. This linear relationship and small deviations very close to 3C can be explained [22].

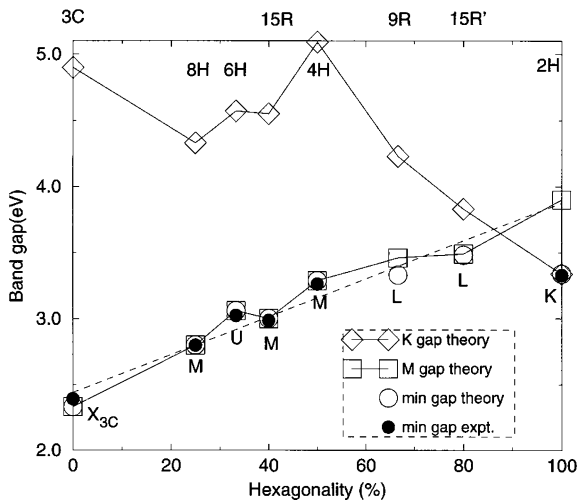


Fig. 2.10 Plot of the minimum and k -specific bandgaps of the SiC polytypes as a function of hexagonality. The 1-eV self-energy correction is added to all the LDA calculated gaps. The labels of the minimum gaps indicate their locations in the Brillouin zones and the M , L , U , and K signs refer to the hexagonal Brillouin zones. For 15R, the M point corresponds to rhombohedral X_R and for 15R' and 9R, the hexagonal L point corresponds to the L_R point. Reprinted with permission from [30]. Copyright 1997, Wiley-VCH Verlag GmbH & Co. KGaA

2.4 Defects

There are many intrinsic defects in as-grown or irradiated silicon carbide crystals, for example, point defects and higher-dimensional defects [31]. Point defects mainly consist of silicon vacancies, carbon vacancies, divacancies, and antisite. The higher-dimensional intrinsic defects comprise dislocations, micropipes, and stacking faults. There are other types of extrinsic defects in silicon carbide crystals associated with impurities. The presence of intrinsic and extrinsic defects in silicon carbide crystals can significantly degrade the performance of SiC-based devices. Moreover, some defects may serve as luminescence centers or nonradiative recombination centers consequently affecting the luminescence properties of silicon carbide. Therefore, identification of these defects, knowledge of the characteristics, and finding approaches to mitigate the effects of these defects are crucial to the application of silicon carbide to electronic devices and light-emitting diodes.

2.4.1 Intrinsic Point Defects

2.4.1.1 Vacancies

Si vacancies in silicon carbide have been extensively studied. Electron spin resonance (ESR) spectroscopy is used to study the electron irradiation-induced defects in

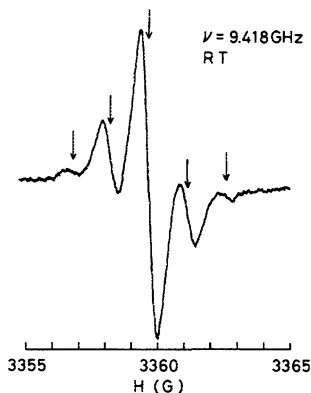


Fig. 2.11 Room-temperature electron spin resonance spectrum of 3C-SiC irradiated by 1-MeV electrons with a fluence of $3 \times 10^{18} \text{ cm}^{-2}$. The arrows indicate five lines of the *T1* center. Reprinted with permission from [32]. Copyright 1989, AIP Publishing LLC

3C-SiC epitaxial films prepared by chemical vapor deposition [32]. An isotropic ESR center (named *T1* center) (Fig. 2.11) that consists of five lines equally spaced at about 1.5 G and has a *g* value of about 2.0029 is observed. This center in electron-irradiated 3C-SiC can be annealed in three stages (150, 350, and 750 °C). The *T1* center is a point defect at the Si site that has 12 second nearest-neighbor Si atoms, and this defect is supposed to be the isolated vacancy at the Si sublattice site. Photoluminescence (PL) reveals a dominant PL line at 1.913 eV, and it disappears after annealing at 100 and 700 °C [33]. The annealing results of the PL line and fractions annealed in each annealing stage agree well with those obtained for the *T1* ESR center, indicating that the 1.913 eV PL line stems from silicon vacancies in 3C-SiC.

The negatively charged Si vacancy in neutron-irradiated 4H-SiC has been identified by electron paramagnetic resonance and electron nuclear double resonance spectroscopy [34]. The magnetic resonance parameters of the negatively charged Si vacancy are nearly the same for 3C-, 4H-, and 6H-SiC. The ligand hyperfine interactions for the nearest- and next-nearest-neighbor shell of the Si vacancy in 3C-SiC are calculated based on the density functional theory using the local density approximation. The calculated result agrees well with the experimental data, thus supporting the assignment of the defect center and determination of the spin state ($S = 3/2$) also helps to identify the defect.

The irradiation-induced photoluminescence spectrum acquired from the electron-irradiated 4H- and 6H-SiC epitaxial layers and corresponding optically detected magnetic resonance signals from this band have been investigated [35]. The number of no-phonon lines in the deep PL band is equal to the number of inequivalent sites in the respective polytype. These lines are at 1,352 meV (*V2*) and 1,438 meV (*V1*) for 4H-SiC and at 1,366 meV (*V3*), 1,398 meV (*V2*), and 1,433 meV (*V1*) for 6H-SiC (Fig. 2.12). The intensity of the PL lines decreases remarkably after short annealing at 750 °C. Electron spin resonance measurement

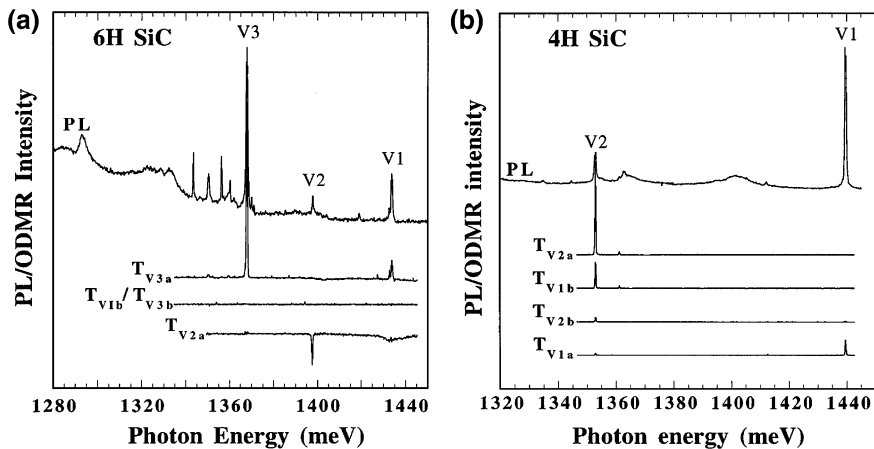


Fig. 2.12 Deep PL band (*top*) and excitation spectrum (*below*) of the various optically detected magnetic resonance signals that are detected from the PL band for the **a** 6H-SiC and **b** 4H-SiC. The samples are 2.5-MeV electron-irradiated epitaxial layers prepared by chemical vapor deposition. Reprinted with permission from [35]. Copyright 2000, American Physical Society

combined with theoretical calculation suggests that the no-phonon lines in the PL originate from internal transitions from an excited state of the neutral Si vacancy at the inequivalent sites in 4H- and 6H-SiC. Moreover, comparison of the characteristics of the triplet states between the polytypes indicates that the V2 lines correspond to the hexagonal sites and V1 and V3 to the cubic sites. The silicon vacancies (V_{Si}) in 3C- and 2H-SiC in all possible charge states are studied using spin-polarized ab initio local spin-density calculation [36]. For the neutral, single, and double negative charge states, the exchange coupling overcomes the Jahn-Teller energies, and the silicon vacancy is found in the high-spin ground state with T_d symmetry. A weak Jahn-Teller effect occurs in the low-spin configuration.

The defects in solids can be ideal centers for generating single-photon emission, which has wide application in quantum communication and quantum computation. This has been demonstrated by the studies of the nitrogen-vacancy defect centers in diamond and nanodiamond [37] showing the virtues of good localization and antiphotobleaching [38, 39]. Silicon carbide as a group IV material also has excellent characteristics [37] that are similar and even superior in some aspects to diamond and thus can be utilized as single-photon sources. The Si vacancy in SiC has been investigated as a promising quantum system for single-defect and single-photon spectroscopy in the infrared region, by electron paramagnetic resonance, optically detected magnetic resonance, and high-resolution PL excitation spectroscopy [40]. The photoluminescence spectra of Si vacancies acquired from 6H- and 4H-SiC are shown in Fig. 2.13. They contain zero-phonon lines accompanied by phonon replicas. The number of zero-phonon lines generally agrees with that of the inequivalent lattice sites in the SiC polytypes. These lines arise at 865 nm (V1), 887 nm (V2), and 906 nm (V3) in 6H-SiC and at 862 nm (V1) and 917 nm (V2) in

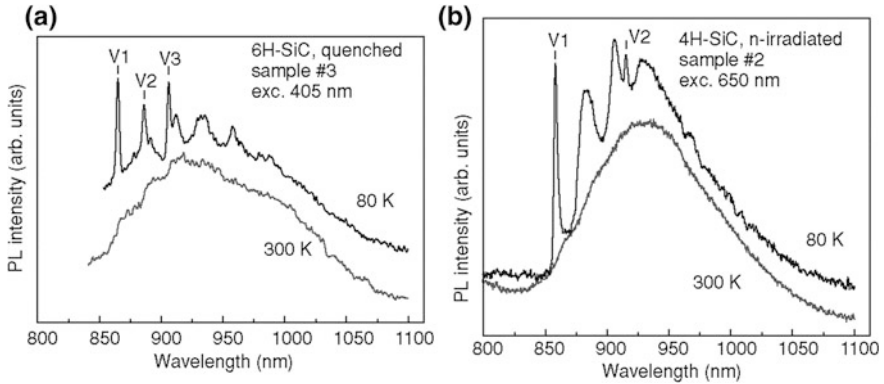


Fig. 2.13 **a** PL spectra acquired from neutron-irradiated 6H-SiC at 80 K and room temperature excited by 405 nm light. **b** PL spectra of neutron-irradiated 4H-SiC at 80 K and room temperature excited by 650-nm light. Reprinted with permission from [40]. Copyright 2011, American Physical Society

4H-SiC. The optically induced inverse population of the ground-state spin sublevels of the silicon vacancies (V_{Si}) is realized in 4H- and 6H-SiC upon irradiation with unpolarized light at low temperature and room temperature [41]. The PL intensity of the zero photon lines changes by a factor of 2–3 at zero magnetic field upon absorption of radio waves with energy equal to the fine structure splitting of spin sublevels of the silicon vacancy ground state. This brings the hope of magnetic resonance detection of a single vacancy. Unlike the intentionally created nitrogen-vacancy defect in diamond, the silicon vacancy is an intrinsic defect and its coherence time is expected to be longer than that of the nitrogen-vacancy defect. The electron spin of the Si vacancy can be controlled by the low-energy radio wave in the range 20–150 MHz, and it is two orders of magnitude smaller than that of the nitrogen-vacancy defect in diamond. Therefore, the Si vacancy in SiC is a very favorable defect in spintronics and quantum information processing.

Except for the silicon vacancy, the carbon vacancy has been investigated. An electron paramagnetic resonance spectrum is obtained from electron-irradiated *p*-type 4H- and 6H-SiC at a temperature above 25 K [42]. This defect center has the C_{3v} symmetry with an electron spin of 1/2, and its configuration is depicted in Fig. 2.14. The detailed hyperfine structure due to its interaction with the four nearest silicon neighbors is obtained by high-frequency electron paramagnetic resonance spectroscopy. In this way, the defect is identified as the positively charged carbon vacancy (V_C^+). Its *g* values and hyperfine tensor are almost the same in both polytypes, and they are independent of the inequivalent lattice sites. The deep levels in *n*-type 4H-SiC epilayers fabricated by chemical vapor deposition are studied by deep-level transient spectroscopy [43]. The Z_1/Z_2 and EH_6/EH_7 centers are dominant in the as-grown samples. Their concentrations increase significantly after electron irradiation at 116 keV, by which only carbon atoms may be displaced. They increase with 0.7 power of the electron fluence of irradiation and their concentrations decrease by

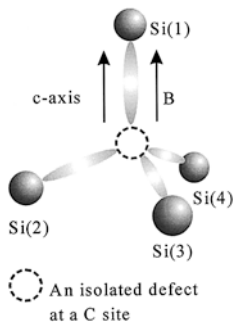


Fig. 2.14 Schematic of an isolated defect (V_C^\bullet) in SiC with the magnetic field parallel to the c -axis. The expected symmetries of the hyperfine tensors representing the interaction with the Si (1) and Si (2, 3, 4) are, respectively, C_{3V} and C_{1h} . Reprinted with permission from [42]. Copyright 2001, American Physical Society

annealing at 1,600–1,700 °C. The concentrations of the Z_1/Z_2 and EH_6/EH_7 centers are very close to each other in all kinds of samples (as-grown, as-irradiated, and annealed ones). It has been proposed that both the Z_1/Z_2 and EH_6/EH_7 centers microscopically contain the same defect, possibly the carbon vacancy. However, first-principle calculation carried out on models for the Z_1/Z_2 defects in 4H-SiC shows that a π -bonded dicarbon interstitial complex next to a nitrogen atom, which is ultra thermally stable and has negative- U character with donor and acceptor levels close to that of the defect, is the most likely candidate of the Z_1/Z_2 defect [44].

Positron lifetime measurement and Doppler broadening spectroscopy have been employed to study the vacancies in 6H-SiC formed by irradiation of 2.2- and 10-MeV electrons [45]. Both neutral carbon and silicon vacancies are observed from n -type SiC, but no vacancies are detected from p -type SiC. The defect energy levels in nitrogen-doped 6H-SiC epitaxial layers prepared by chemical vapor deposition and irradiated with 2-MeV electrons and implanted with 300-keV deuterium or hydrogen are investigated by deep-level transient spectroscopy at room temperature [46]. Five levels within the energy gap are observed, and it is proposed that the $E_C - 0.51$ eV level (E_C referring to the conduction-band minimum energy) originates from a carbon vacancy. The two levels at $E_C - 0.34$ and $E_C - 0.41$ eV originate from the occupation of nonequivalent lattice sites. The results for the $E_C - 0.62$ eV and $E_C - 0.64$ eV levels support a defect model involving a silicon vacancy on the nonequivalent sites in the 6H lattice.

The neutral and charged Si and C vacancies in 3C- and 4H-SiC are theoretically studied by the density functional theory using the local density approximation as well as local spin-density approximation [47]. A plane-wave-supercell approach is combined with the ultrasoft Vanderbilt pseudopotentials to ensure converged calculation. Generation of the C-site vacancy is generally accompanied by a remarkable Jahn-Teller distortion, whereas only an outward-breathing relaxation occurs at the Si-site vacancy due to strong localization of the neighboring C dangling bonds. As a result, Si vacancies show high-spin configurations and C

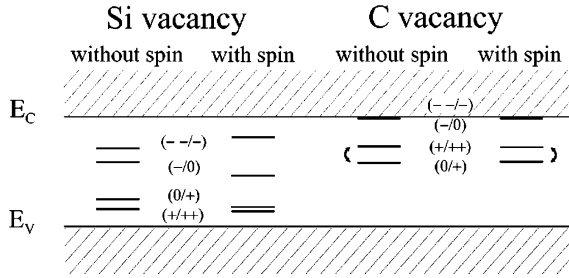


Fig. 2.15 Schematic of the energy levels of the Si and C vacancies at cubic and hexagonal sites in 3C-SiC obtained by local density approximation or local spin-density approximation calculation using the 216-atom supercell. Reprinted with permission from [47]. Copyright 1999, American Physical Society

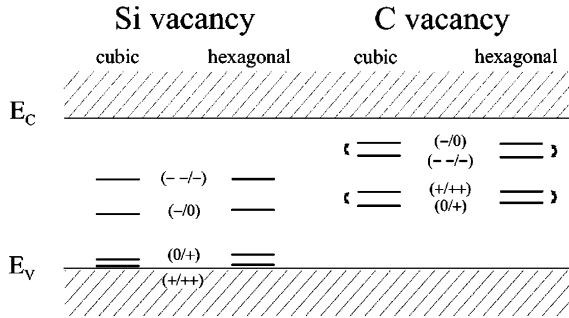
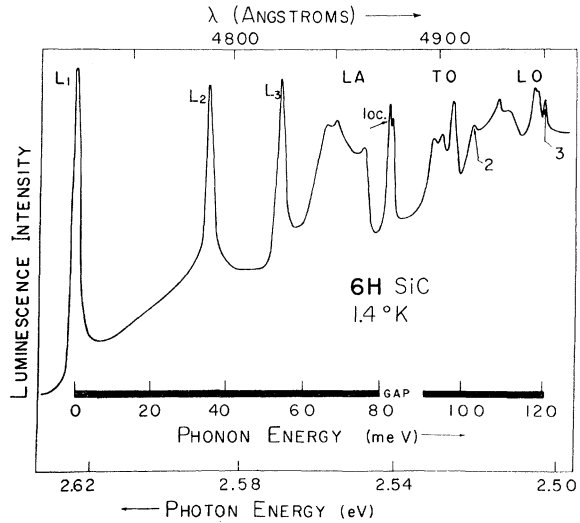


Fig. 2.16 Schematic of the energy levels of the Si and C vacancies in 4H-SiC obtained by local density approximation or local spin-density approximation calculation employing the 128-atom supercell. Reprinted with permission from [47]. Copyright 1999, American Physical Society

vacancies show low-spin configurations with a negative- U behavior. The schematic diagrams of the energy levels of the vacancies are depicted in Figs. 2.15 and 2.16.

Ion implantation of SiC may produce damage in the crystal lattice that is hard to repair. Some of these defects remain even after annealing at a high temperature. One of these persistent defects is observed from 3C-SiC after 120-keV He-ion implantation or 1-MeV electron bombardment. This defect (D_1) exhibits strong low-temperature luminescence, which is independent of the implanted ion, and the luminescence spectrum contains a zero-phonon line (at 6279.8 Å) accompanied by a strong vibronic structure [48]. This luminescence remains after annealing at 1,600 °C. The radiation defects in 6H-SiC produced by ion implantation and electron bombardment have been investigated [49]. The defects also show low-temperature luminescence. This D_1 spectrum persists after annealing at 1,700 °C. Its intensity depends strongly on the defect concentration. The defect is proposed to originate from a divacancy. Unlike the case of 3C-SiC, there are three no-phonon lines in the D_1 band (Fig. 2.17) due to the three nonequivalent sites in

Fig. 2.17 Portion of the 1.4 K D_1 PL spectrum of the 1,300 °C annealed and ion-bombarded 6H-SiC. L_1 , L_2 , and L_3 are no-phonon lines and most of the phonon replicas belong to the L_1 peak. Reprinted with permission from [49]. Copyright 1972, American Physical Society



6H-SiC. The spectrum shows unusual temperature dependence. The low-temperature (1.4 K) spectrum vanishes as the high temperature (77 K) form emerges, and this abrupt spectral change is ascribed to lattice distortion at low temperature. The D_1 centers with similar properties have also been observed from 4H-SiC [50].

Two negative- U centers have been observed from 4H-SiC by capacitance transient techniques [51]. Each negative- U center generates two levels in the bandgap, one shallower donor level, and one acceptor level, and the electron ionization energy of the acceptor level is larger than that of the donor level. The two-electron emissions from the two acceptor levels result in the previously reported deep-level transient spectroscopy peak related to the Z_1 center. The electron paramagnetic resonance measurement combined with ab initio supercell calculation suggests that the $P6/P7$ defect centers in 3-MeV electron-irradiated 4H-SiC originate from the triplet ground states of the neutral divacancy in the axial C_{3v} and monoclinic C_{1h} configurations (Fig. 2.18) [52]. The spin density is located mainly on three nearest C neighbors of the Si vacancy, and it is negligible on the nearest Si neighbors of the C vacancy. The vacancy model for the $P6/P7$ centers points out that the interaction between V_{Si} and V_C to form divacancies is significant and so the divacancy is a common defect in SiC. Annealing indicates that the formation of the divacancy is governed mainly by diffusion of V_{Si} and V_C . First-principle calculation indicates that there is a negative- U behavior at $E_V + 0.7$ eV between the charge states ± 1 only for nearest-neighbor divacancies on different lattice sites in 4H-SiC, but not for all the other cases in 4H-SiC or for the cubic divacancy in 3C-SiC [53].

Similar to the case of Si vacancy, the divacancy in SiC can be used as an individually controllable solid state quantum bit. It has been demonstrated that several defect spin states in high-purity semi-insulating 4H-SiC can be optically addressed

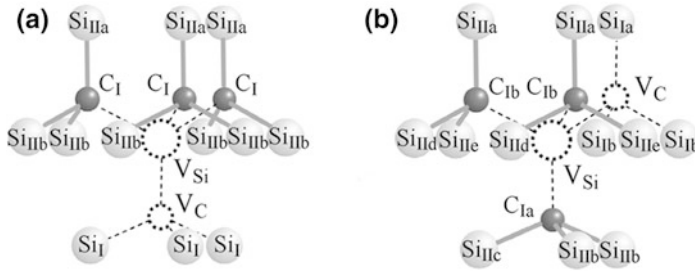


Fig. 2.18 Schematic of the **a** axial (C_{3v}) and **b** monoclinic (C_{1h}) configurations of the divacancy in electron-irradiated 4H-SiC. Reprinted with permission from [52]. Copyright 2006, American Physical Society

and coherently controlled in the time domain at temperature between 20 and 300 K [54]. Using optical and microwave techniques similar to those used in diamond nitrogen-vacancy qubits, researchers have studied the spin-1 ground state of each of the four inequivalent forms of the neutral carbon–silicon divacancy as well as a pair of defect spin states of unidentified origin. These six lines lie in the range of 1.09–1.20 eV at 20 K. These defects are optically active near the telecommunication wavelengths, and they possess desirable spin coherence properties comparable to those of the nitrogen-vacancy center in diamond. These divacancy centers are promising candidates in many photonic, spintronic, and quantum information applications. Further study demonstrates that 4H-, 6H- and 3C-SiC all host coherent and optically addressable defect spin states in the 1.08–1.20-eV range, including states with room-temperature quantum coherence [55]. It suggests that crystal polymorphism in SiC can be a degree of freedom for engineering spin qubits.

It is well known that annealing can change the structure and properties of intrinsic defects especially vacancies. The annealing processes of vacancy-type defects in 3-MeV electron-irradiated and as-grown 6H-SiC are investigated by positron lifetime spectroscopy [56]. A vacancy-type defect giving rise to a positron lifetime of 183 ps is detected from the as-grown *n*-type 6H-SiC. This defect is annihilated after annealing at around 1,400 °C. Electron irradiation produces defects related to carbon vacancies, silicon vacancies, and divacancies. The defects related to carbon vacancies and divacancies are annealed at temperature up to 500 °C, whereas the defects related to silicon vacancies are annealed at around 750 and 1,400 °C. The observed defect is thus suggested to arise from Si vacancies, possibly complexes of silicon vacancies and nitrogen atoms. No vacancy-type defects are detected from *p*-type 6H-SiC even after electron irradiation.

Thermal elimination of the defects in 4H-SiC has been studied [57]. The Z_1/Z_2 and EH_6/EH_7 concentrations are reduced from the initial 10^{12} – 10^{13} cm $^{-3}$ to below the detection limit of 1×10^{11} cm $^{-3}$ after thermal oxidation at 1,150–1,300 °C. However, oxidation produces a high concentration (5 – 8×10^{12} cm $^{-3}$) of another *HK0* center ($E_V + 0.78$ eV). Further annealing in argon at 1,550 °C eliminates this *HK0* center. Therefore, all the major deep defect levels can be eliminated by

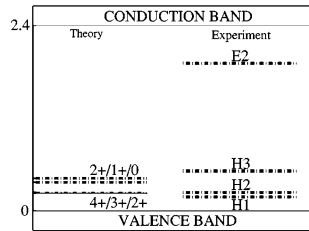


Fig. 2.19 Comparison of the calculated ionization levels of Si antisite in 3C-SiC with the experimental deep-level transient spectroscopy data obtained from Ref. [58]. Reprinted with permission from [59]. Copyright 1998, American Physical Society

this two-step thermal treatment and the carrier lifetime in a 98- μm -thick n -type 4H-SiC epilayers can be improved from 0.64 to 4.52 μs afterward.

2.4.1.2 Antisites

The antisite defect is generated by occupation of a Si (C) position by a C (Si) atom. Deep-level transient spectroscopy performed on neutron-irradiated 3C-SiC reveals point defect-related centers called $H1$, $H2$, $H3$, and $E2$ [58]. The electronic energy levels of H centers are located at 0.18 eV ($H1$), 0.24 eV ($H2$), and 0.514 eV ($H3$) above the valence-band maximum, whereas the level of $E2$ is located at 0.49 eV below the conduction-band minimum. Ninety percent of the produced defects are eliminated by annealing at 350 $^{\circ}\text{C}$, whereas the concentration of the $E2$ centers increases gradually with annealing of the H centers. The theoretical calculation based on the density functional theory with the local density approximation suggests that the H centers are ascribed to silicon antisite (Si_{C}) defects generated by neutron irradiation [59]. In both 3C- and 2H-SiC, the silicon antisite has several ionization levels in the bandgap. These levels in 3C-SiC are calculated by the plane-wave pseudopotential method and the results agree well with the deep-level transient spectroscopy data (Fig. 2.19).

The defect D_1 with characteristic photoluminescence (PL) lines that is produced from irradiated SiC has been proposed to arise from the divacancy [48, 49], but the assignment of this defect is debatable and some researchers have suggested its origin to be antisite. A study of the 2-MeV electron-irradiated 4H-SiC (n^+ - and p^+ -type substrates and epilayers grown by chemical vapor deposition with different levels of n - or p -type residual doping) reveals a series of emission lines, and this spectrum named E_A consists of several sharp no-phonon lines accompanied by a broad phonon-assisted structure (Fig. 2.20) [60]. Annealing at around 750 $^{\circ}\text{C}$ induces an abrupt change in the spectrum and further annealing at over 750 $^{\circ}\text{C}$ results in the dominance of the strong D_1 PL spectrum. Up to 40 no-phonon lines (within 2.8–2.9 eV) are resolved in the E_A spectrum. Photoluminescence excitation spectroscopy shows that the lines come in groups of two to four lines. The characteristics of the line groups suggest that they are attributed to bound-exciton

Fig. 2.20 Effects of annealing on the no-phonon lines in the PL spectrum (at 15 K) of 2-MeV electron-irradiated 4H-SiC. **a** No annealing. **b** Annealing at 750 °C. **c** Annealing at 1500 °C. The D_1 lines L_1 and M_1 that dominate the spectrum after annealing at 1,500 °C (c) are one order of magnitude more intense than the lines of the (a) and (b) spectra. Reprinted with permission from [60]. Copyright 1999, American Physical Society

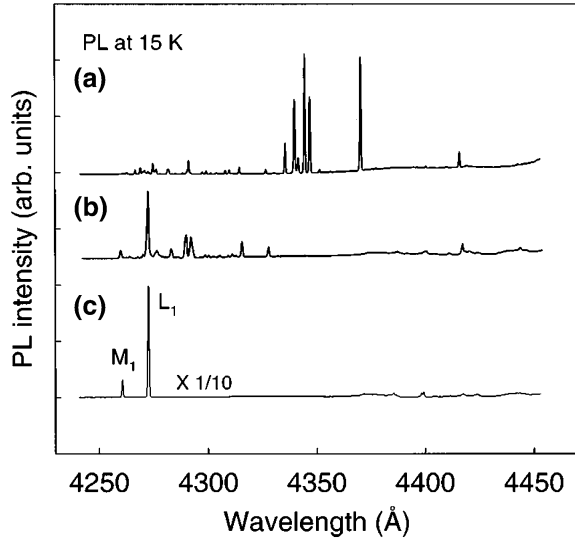
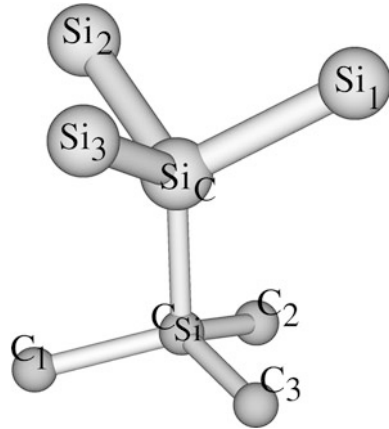
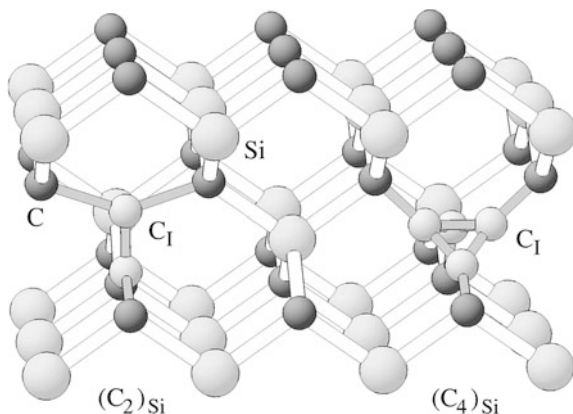


Fig. 2.21 Schematic of the antisite pair at the k site in 4H-SiC. For the C_{1h} symmetry in the single positively charged state, the Si(1) and C(1) atoms lie in the mirror plane making the Si(2), Si(3) and C(2), C(3) atoms equivalent. Reprinted with permission from [62]. Copyright 2003, American Physical Society



recombination at isoelectronic defect centers. By using first-principle density functional calculation, the origin of the lines of the E_A spectrum has been investigated [61]. These lines originate from the recombination of a delocalized electron with a localized hole bound to a Si antisite defect (Si_C), which is in proximity with a C antisite (C_{Si}). The most stable antisite pair may generate the most energetic line in the E_A spectrum or the D_1 band. The study based on the low-temperature PL and ab initio supercell calculation for 3C- and 4H-SiC shows that the neutral antisite pair (Fig. 2.21) is a good candidate for the D_1 defect [62]. The calculated one-electron level of the neutral antisite pair is very close to the measured transition energy of the zero-phonon line, and the calculated local vibration modes can explain the experimental findings. The calculated hyperfine constants of the

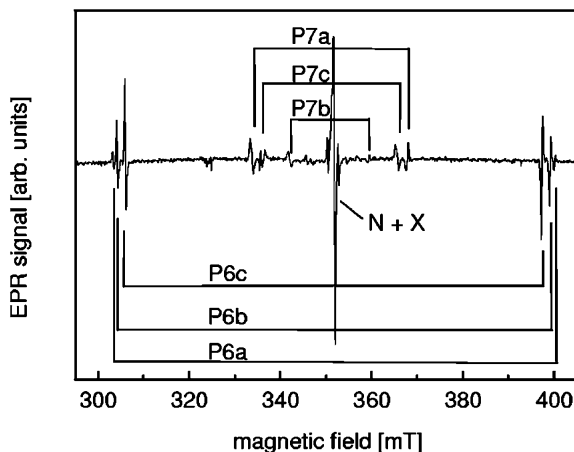
Fig. 2.22 Configuration of the dicarbon antisite $(C_2)_{Si}$ and carbon cluster with four atoms on a silicon site $(C_4)_{Si}$ in 3C-SiC. Reprinted with permission from [66]. Copyright 2004, American Physical Society



antisite pair in its paramagnetic state support this assignment of the D_I center. However, another study based on the local density functional calculation shows that the close-by antisite pair is not stable enough to account for D_I [63]. Instead, D_I is suggested to be related to an isolated Si antisite and the four forms of the close-by antisite pair in 4H-SiC is supposed to give rise to the a , b , c , and d members of the E_A PL spectrum.

Another famous persistent intrinsic defect in SiC is D_{II} . This defect center is detected from ion-implanted and annealed (at 1,300 °C) 3C-SiC by low-temperature luminescence spectroscopy [64]. The PL spectrum reveals a number of high-energy localized modes. One mode has an energy of 164.7 meV, which is equivalent to the highest lattice frequency in diamond and far above the 120.5-meV lattice limit of SiC. A carbon di-interstitial is suggested to account for this defect, which arises after annealing at 1,300 °C and persists after annealing at 1,700 °C. The D_{II} center is also observed from the unannealed ion (B, Al, P) implanted 3C-SiC films [65]. The D_{II} zero-phonon line is located at about 2.3 eV. Its intensity increases with annealing temperature, but drops rapidly for annealing temperature above 1,600 °C. The phonon replicas of the D_{II} zero-phonon line are located in the range of 1.98–2.25 eV. The spectral density of the phonon replicas resembles the phonon density of states in diamond, suggesting that the observed spectrum stems from a carbon-associated defect. The structural, electronic, and vibrational properties of the dicarbon antisite complexes have been investigated by the density functional theory to check whether they can account for the D_{II} center [66]. Figure 2.22 shows the configuration of the dicarbon antisite $(C_2)_{Si}$, where two carbon atoms sharing a silicon site are surrounded by a tetrahedron of four carbon atoms. The dicarbon antisite possesses a characteristic vibrational pattern in the frequency range of the D_{II} spectrum but it cannot explain all the experimentally observed phonon replicas. The D_{II} -type centers may be related to larger carbon clusters built on the basis of the dicarbon antisite.

Fig. 2.23 Electron paramagnetic resonance spectrum of neutron-irradiated and 1,000 °C annealed 6H-SiC acquired with the magnetic field parallel to the c -axis of the crystal. Six spin-triplet spectra labeled $P6a$, b , c , and $P7a$, b , c are observed. Reprinted with permission from [67]. Copyright 2001, American Physical Society



2.4.1.3 Carbon Vacancy–Carbon Antisite Pair

The carbon vacancy–carbon antisite ($C_{Si}-V_C$) pair is another important point defect in silicon carbide. The $P6/P7$ spectrum observed from neutron-irradiated and annealed nitrogen-doped 6H-SiC prepared by sublimation is suggested to arise from a photoexcited spin-triplet state of the carbon vacancy–carbon antisite ($C_{Si}-V_C$) pair [67]. The photoexcited paramagnetic triplet state of this defect in 6H-SiC is observed from all the inequivalent lattice sites and all orientations by electron paramagnetic resonance and magnetic circular dichroism of the absorption. The electron paramagnetic resonance signal comprises six spin-triplet lines (Fig. 2.23). First-principle calculation shows that among several pair defect models, $C_{Si}-V_C$ in the charge state +2 (Fig. 2.24) is the only intrinsic nearest-neighbor pair defect that is diamagnetic in its ground state and has a photoexcited spin-triplet state that can result in the observed electron paramagnetic resonance hyperfine structure and optical transitions. The $C_{Si}-V_C$ pair is observed after irradiation and subsequent annealing above the annealing temperature of the silicon vacancy. Therefore, movement of the carbon atom into the neighboring Si vacancy during annealing may result in the formation of the $C_{Si}-V_C$ defect.

However, the same spectrum generated from electron-irradiated 4H-SiC has been proposed to arise from the triplet ground states of the neutral divacancy [52]. Instead, another experimentally observed defect ($SI5$ center) in 4H-SiC is assigned to the negatively charged carbon vacancy–carbon antisite pair $(C_{Si}V_C)^-$ based on electron paramagnetic resonance and first-principle calculation [68]. The vacancy defects and $SI5$ center are found to play an important role in the semi-insulating property of SiC. Two sets of photoluminescence lines (called A and B) are detected from electron-irradiated and ion-implanted 4H-SiC at 7 K (Fig. 2.25) [69]. The spectral details, temperature dependence, and annealing characteristics suggest that the A and B spectra stem from the neutral on-axis and off-axis carbon antisite–vacancy pairs $(V_C C_{Si})^0$. The relatively impure and highly compensated-doped

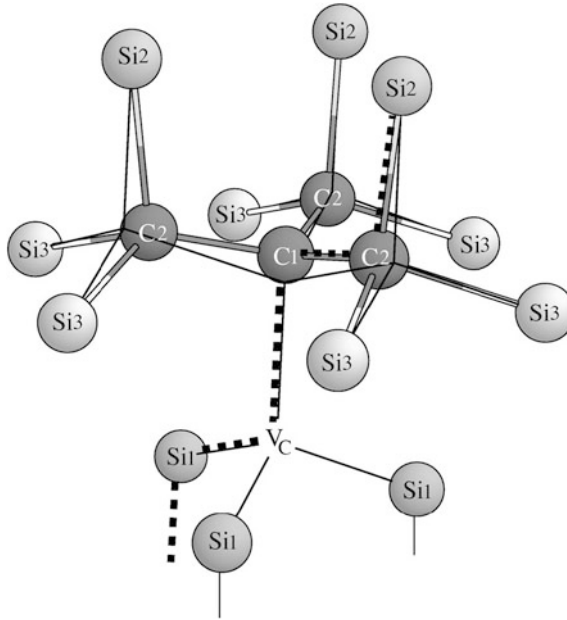


Fig. 2.24 Calculated relaxed structure of $(C_{Si}-V_C)^{2+}$ in 6H-SiC. The thin lines mark the position of the bonds in the ideal lattice. The carbon antisite C1 relaxes by 16 % of the bond length in the ideal crystal away from the vacancy. Reprinted with permission from [67]. Copyright 2001, American Physical Society

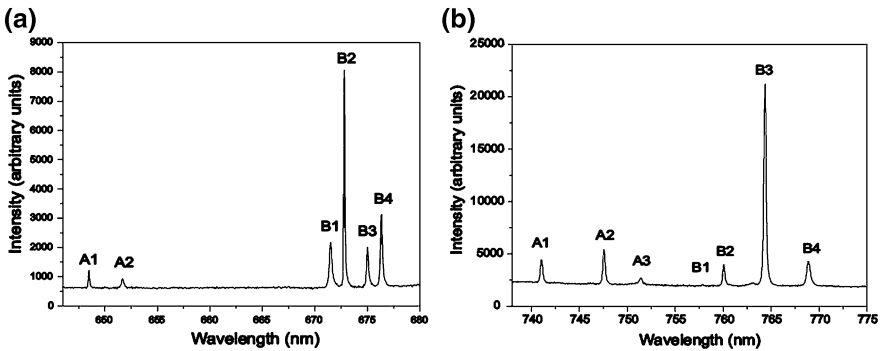


Fig. 2.25 A and B spectra of **a** 4H-SiC and **b** 6H-SiC excited by 488-nm light at 7 K. Reprinted with permission from [69]. Copyright 2009, American Physical Society

samples exhibit very strong A and B PL, whereas the purer largely uncompensated *n* (N)- or *p* (Al)-doped samples exhibit mainly PL of the Si vacancy-related defects and weakly PL of A and B even after annealing at 900 °C.

The carbon antisite–vacancy defect showing A/B PL can serve as a single-photon source [70]. These defects are produced in high-purity, semi-insulating 4H-SiC

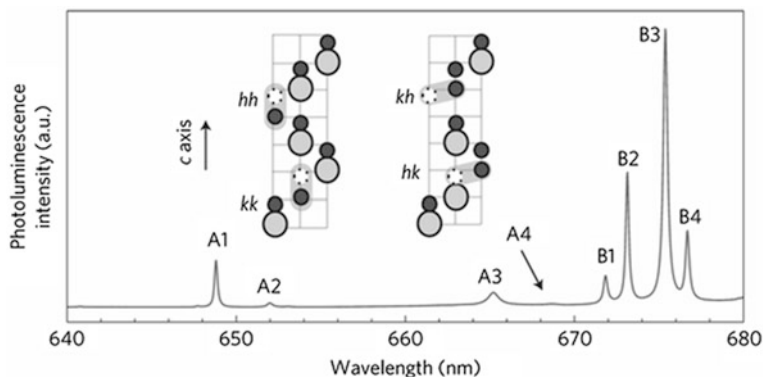


Fig. 2.26 A and B PL lines observed from electron-irradiated 4H-SiC acquired at 80 K. The proposed atomic structure of the defects $C_{Si}-V_C$ yielding the PL is shown in the (1120) plane (small/large circle representing C/Si atom and small open circles denoting vacancies). The carbon antisite-vacancy pair has four possible configurations: hh/kk axial configurations with C_{3v} symmetry, and hk/kh basal plane configurations with C_{1h} symmetry. h/k denotes the hexagonal/cubic site in the SiC lattice. Reprinted with permission from [70]. Copyright 2014, Macmillan Publishers Ltd

wafers by irradiation with 2-MeV electrons followed by annealing. Low electron fluences are adopted to give rise to isolated single defects, and the annealing temperature is tuned to increase/decrease the number of defects. The sample shows obvious A/B PL lines (Fig. 2.26). The lines are at 648.7 nm (A1), 651.8 nm (A2), 665.1 nm (A3), 668.5 nm (A4), 671.7 nm (B1), 673.0 nm (B2), 675.2 nm (B3), and 676.5 nm (B4). These lines arise from the $C_{Si}V_C$ defect. In contrast to the previous assignment [69], the ab initio supercell calculation in combination with group theory indicates that the neutral $C_{Si}-V_C$ pair does not have visible PL and so the positively charged $C_{Si}-V_C$ pair (spin = 1/2) with predicted visible PL is proposed as the origin of the A/B PL. PL from single-defect centers is observed by room-temperature confocal microscopy, as shown in Fig. 2.27a. These spectra are in accordance with the A/B lines. Single-photon emission is confirmed using a Hanbury Brown-Twiss interferometer based on the observation that the second-order photon correlation function at zero delay is $g^{(2)}(0) < 0$ (Fig. 2.27b). The typical acquired excited state lifetime is 1.2 ns. Forty-five percent of the defect emitters measured in a sample irradiated and annealed at 300 °C are stable over a long period of time, whereas the other emitters show PL blinking and some eventually photobleach. The samples annealed at higher temperature (500 °C) contain nearly no blinking centers.

2.4.1.4 Studies on Multiple Point Defects

The effects of deviations from stoichiometry on the relative abundances of native defects and electronic properties of 3C-SiC have been investigated by ab initio calculation [71]. The result shows that the dominant defect in a perfectly

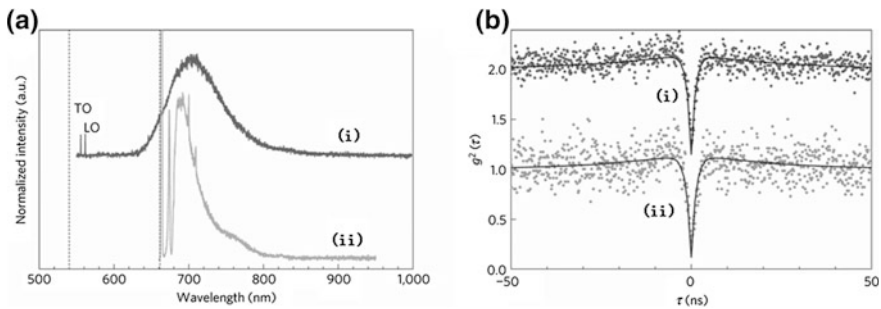


Fig. 2.27 **a** Room-temperature PL spectra of a single-photon source in the irradiated 4H-SiC excited by the 532 nm (i) and 660 nm (ii) lines. The dashed lines denote excitation wavelengths. **b** Corresponding antibunching curves. Reprinted with permission from [70]. Copyright 2014, Macmillan Publishers Ltd

stoichiometric SiC is the electrically inactive $\text{Si}_\text{C}-\text{C}_{\text{Si}}$ pair. In Si-rich SiC, the concentrations of the stoichiometry compensating defects depend strongly on the Fermi-level position, and the Si_C antisite and carbon vacancy are separately the dominant defects in *n*- and *p*-type SiC. As a double donor, the carbon vacancy acts as a charge-compensating defect when the Fermi level is lowered and reduces the doping efficiency of acceptors. The electrically inactive C_{Si} antisite dominates in the C-rich SiC regardless of the position of the Fermi level. The slightly C-rich SiC is thus more suitable for *p*-type doping in electronic applications. The electronic and atomic structures of the monovacancies and antisite defects in 4H-SiC in all possible charge states have been investigated using a plane-wave pseudopotential method based on the density functional theory and local spin-density approximation [72]. The calculation indicates no negative-*U* behavior for the carbon vacancies. Hence, the single positive charge state of the carbon vacancy V_C^+ is stable, in agreement with previous experimental result. The silicon antisite Si_C^+ is found to be stable at small values of electron chemical potential. These results agree with previous experiments.

Electrically active defects in 4H-SiC are produced by irradiation of low-energy electrons below the threshold of Si atom displacement [73]. The majority and minority carrier traps induced by radiation are analyzed by capacitance transient techniques. Four electron traps (EH1, Z_1/Z_2 , EH3, and EH7) and one hole trap (HS2) are detected (Fig. 2.28) and suggested to be related to the initial displacement of carbon atoms. Their properties are summarized in Table 2.2. The concentrations of these defects increase linearly with irradiation dose, suggesting that no divacancies or di-interstitials are generated. None of the observed defects is found to be an intrinsic defect-impurity complex. The probable candidates for these defects are limited to carbon vacancies, split interstitials, and antisites. No additional defects are detected from samples irradiated by electrons with energies higher than the threshold of Si atom displacement.

The irradiation and annealing effects on defects as well as the defect migration processes in SiC have been extensively studied by theoretical calculation and simulation. Molecular dynamics simulation using a modified Tersoff potential is

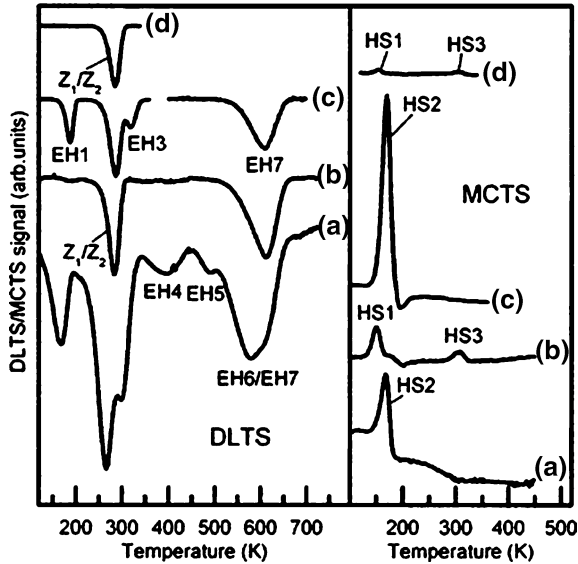


Fig. 2.28 Deep-level transient spectroscopy and minority carrier transient spectroscopy spectra of electron-irradiated 4H-SiC. **a** Irradiation with 9-MeV electrons. **b** Irradiation with 9-MeV electrons and annealing at 950 °C for 1 h. **c** Irradiation with 210-keV electrons. **d** Irradiation with 210-keV electrons and annealing at 950 °C for 1 h. Reprinted with permission from [73]. Copyright 2004, AIP Publishing LLC

Table 2.2 Electrical properties of the defects observed in 4H-SiC irradiated by low-energy electrons. The capture cross section is estimated from the intercept of the Arrhenius plot. Reprinted with permission from [73]. Copyright 2004, AIP Publishing LLC

Position in the bandgap (eV)	Label	Peak temperature, K (for 230-ms rate window)	Capture cross section, cm ²
$E_c - 0.41$	EH1 (SS ₁)	188	4×10^{-15}
$E_c - 0.68$	(Z _{1/2})	287	2×10^{-14}
$E_c - 0.71$	EH3 (S ₂)	320	4×10^{-15}
$E_c - 1.54$	EH7	607	3×10^{-14}
$E_v - 0.39$	HS2	170	2×10^{-14}

used to study the primary damage state and defect production in the displacement cascades in 3C-SiC [74]. Recoils with energies of 0.25–50 keV are simulated at 300 K. It is found that the displacement threshold energy surface is highly anisotropic. The dominant surviving defects are C interstitials and vacancies, whereas only a small fraction of the surviving defects is antisites. The defect clusters are much smaller and rarer compared to those in metals. The simulation also shows that the defect production efficiency decreases with increasing recoil

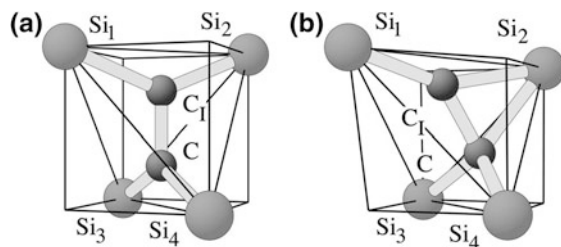


Fig. 2.29 Configuration of the carbon split interstitial $C_{sp(100)}$: **a** $\langle 100 \rangle$ orientation with D_{2d}/D_2 symmetry and **(b)** tilted $C_{sp(100)}$. The $C_{spSi(100)}$ configuration corresponds to the untilted $C_{sp(100)}$ with the $C-C_1$ pair replaced by a $Si-C_1$ pair and C neighbors instead of Si neighbors. Reprinted with permission from [77]. Copyright 2003, American Physical Society

energy. The formation energies and properties of the native defects in 3C-SiC are studied by density functional calculation based on the pseudopotential plan-wave method within local density approximation combined with the molecular dynamics simulation using Tersoff potentials [75]. It is found that the most favorable configurations for the C interstitials are $\langle 100 \rangle$ and $\langle 110 \rangle$ dumbbells with formation energies of 3.16–3.59 eV, and the most favorable Si interstitial is Si tetrahedral surrounded by four C atoms with a formation energy of 6.17 eV. The formation energies of the vacancies and antisite defects obtained by molecular dynamics simulation agree with those obtained by density functional calculation. The long-range migration of point defects in 3C-SiC is subsequently investigated by both molecular dynamics simulation and the nudged elastic band method [76]. The results show that stable C split interstitials can migrate via the first or second nearest-neighbor sites, whereas Si interstitials migrate directly from one tetrahedral position to another neighboring equivalent position by a kick-in/kick-out process. C and Si vacancies jump to one of their equivalent sites through a direct migration mechanism. The calculated migration barriers for C and Si interstitials agree with experiments.

Diffusion of intrinsic defects in 3C-SiC is studied by density functional calculation using the local density approximation or local spin-density approximation [77]. The results show that the vacancies migrate to their own sublattice. The carbon split interstitials (Fig. 2.29) and two silicon interstitials (tetrahedrally carbon-coordinated interstitial in the p -type materials and the split interstitial in the compensated and n -type materials) are found to be more mobile than the vacancies, thereby playing a prominent role in diffusion. The metastable Si vacancy in p -type and compensated SiC is transformed into the more stable vacancy–antisite complex, suppressing its contribution to diffusion processes. The most important migration channels for vacancies and interstitials in 3C-SiC are depicted in Fig. 2.30. The annealing kinetics of mobile intrinsic defects in 3C-SiC is investigated by the same method [78]. The calculated migration and reaction barriers help to determine the annealing mechanisms. The carbon and silicon interstitials have higher mobility than the vacancies, thus driving the annealing mechanisms at lower temperature including vacancy–interstitial recombination and formation of

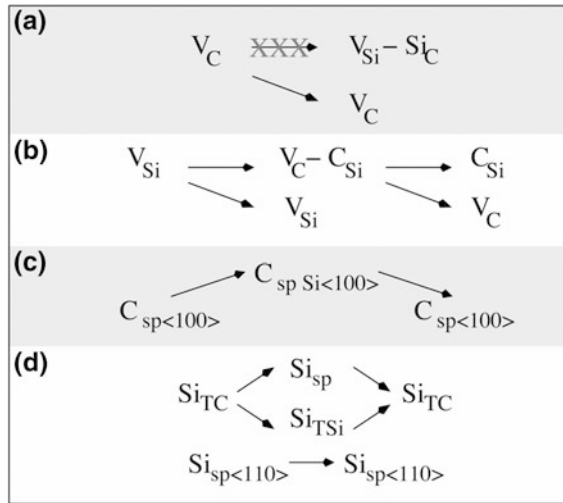


Fig. 2.30 Dominant migration mechanisms of interstitials and vacancies in 3C-SiC: **a** C vacancies (V_C) migrate on the C sublattice only, **b** transformation of the Si vacancy (V_{Si}) into a C vacancy-antisite complex V_C-C_{Si} (p -type and compensated) and vacancy migration on the Si sublattice (n -type), **c** C-interstitial migration via split-interstitial configurations $C_{sp Si<100>}$ and $C_{sp<100>}$, and **d** kick-out mechanism for the C-coordinated Si interstitial (Si_{TC}) via split interstitials ($Si_{sp<100>}$ and $Si_{sp<110>}$) (p -type) and direct migration of the Si split-interstitial $Si_{sp<110>}$ (compensated and n -type). Reprinted with permission from [77]. Copyright 2003, American Physical Society

interstitial carbon clusters. These clusters emit carbon interstitials at higher temperature. In p -type SiC, transformation of the silicon vacancy into the more stable vacancy-antisite complex serves as an annealing mechanism before vacancy migration.

The aggregates of carbon interstitials in 3C- and 4H-SiC have been studied theoretically [79]. Formation of carbon aggregates is found to be energetically favored, and all the carbon clusters are electrically active. The electronic and vibronic properties depend strongly on the polytype of SiC. Additionally, comparison of the calculated local vibration modes of all the defect aggregates to those observed from the P and D_{II} PL centers suggests that these centers are related to the $(C_2)_{Si}$ and $[(C_2)_{Si}]_2$ defects, respectively. Migration of vacancies at high temperature is studied by the self-consistent charge density functional-based tight-binding method [80]. The energy barrier for sublattice migration of V_{Si} is shown to be lower than that for V_C , and hence, V_{Si} should anneal out at lower temperature as supported by experiments. The calculation shows that the motion of vacancies can mediate the migration of antisites. Vacancy-assisted diffusion of carbon antisites is much faster than that of silicon antisites, thereby creating carbon antisite clusters. The result shows that the mobility of carbon antisites can trigger the formation of larger antisite complexes.

Fig. 2.31 Interaction between dislocations in parallel glide planes ($180\times$). Reprinted with permission from [81]. Copyright 1960, AIP Publishing LLC

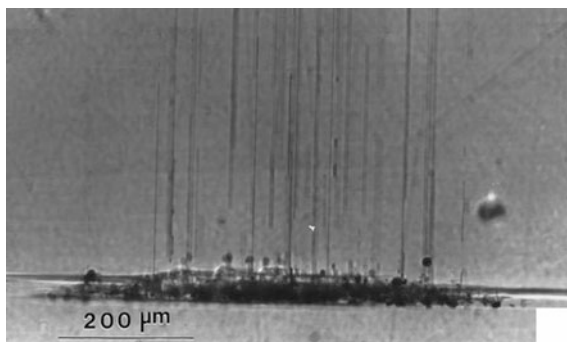


2.4.2 Dislocations and Micropipes

Dislocations and micropipes have long been observed from silicon carbide. The various dislocations and glide elements in 6H-SiC have been investigated by etching in conjunction with optical microscopy and X-ray diffraction microscopy [81]. The conventional etching technique is demonstrated to be suitable for the identification of the intersection of dislocations on the (0001) surfaces. High-density dislocations in the (0001) planes are observed by diffraction microscopy, and dislocations with $[11\bar{2}0]$ vectors are observed in addition to evidence of slip on both the basal planes and “puckered” pyramidal plane. Pileups formed by slip and dislocation walls formed by climb are identified. The dislocations in the parallel glide planes interact with each other (Fig. 2.31), and they line up in a direction perpendicular to the glide planes. Propagation of basal plane dislocations from the off-axis 4H-SiC substrate into the homoepitaxial layer has been investigated by chemical etching, optical microscopy, and transmission electron microscopy [82]. The basal plane dislocations in the substrates are converted into threading edge dislocations in the epilayer at the epilayers/substrate interface. TEM reveals that the converted dislocations are inclined from the c -axis toward the down-step direction by about 15° . The in-plane orientation of the inclination is toward the step flow direction within $\pm 10^\circ$. The conversion can be interpreted as a result of the image force in the epilayers between flowing growth steps and basal plane dislocations. A theoretical study has been conducted on the 30° and 90° Shockley partial dislocations lying in the $\{111\}$ and basal planes of cubic and hexagonal silicon carbide [83]. The core structure, energetics, and electronic structure of the dislocations are determined. The thermal activation barriers to glide motion of 30° and 90° Shockley partials are calculated in terms of a process involving the formation and migration of kinks along the dislocation line.

Micropipes that constitute a major defect in mass-produced SiC wafers are hollow tubular defects penetrating the SiC single crystals. Their radius ranges from

Fig. 2.32 Optical micrograph showing nucleation of micropipes at a group of inclusions during growth in a 4H-SiC wafer. Reprinted with permission from [88]. Copyright 1999, AIP Publishing LLC



a few tens of nanometers to several tens of micrometers and the density at the growth surface ranges from several hundred to less than one micropipe per cm^2 [84]. These micropipe defects can severely hamper the performance of SiC power devices [85]. Micropipe defects in 4H- and 6H-SiC substrates have been found to lead to preavalanche reverse-bias point failure in many epitaxially grown p - n junction devices with an area of 1 mm^2 or larger. The SiC power device ratings will be restricted to several amps or less if the defect density is on the order of 100s of micropipes/ cm^2 .

Many studies indicate that the micropipes in SiC are hollow core dislocations [83]. The dependence of the micropipe radius on the Burgers vector content of the micropipes in different SiC has been analyzed, and the relationship can be explained by Frank's model of a hollow core dislocation when a mixed dislocation is assumed [86]. The origin of micropipes and nanopipes in SiC are hollow superscrew dislocations formed by the attraction of unit screw dislocations to a nanopipe formed at the axis of some triple junctions [87].

A model has been proposed to explain the formation of screw dislocations (including micropipe nucleation) in SiC [88]. Micropipes have been demonstrated to nucleate at the sites of foreign materials inclusions by synchrotron white beam X-ray topography and transmission optical microscopy (Fig. 2.32). Incorporation of the inclusions into the growing crystal can lead to deformation of the protruding ledge that constitutes the overgrowing layer. Deformation is accommodated by the crystal lattice creating pairs of opposite-sign screw dislocations (Fig. 2.33), which then propagate with the growing crystal. Using a series of synchrotron imaging techniques in the reflection geometries, micropipes in 6H-SiC crystals have been mapped [89]. The combined synchrotron white beam X-ray topography techniques and corresponding simulation (Fig. 2.34) demonstrate explicitly that the micropipes are pure superscrew dislocations. The details of the superscrew dislocations, including the spatial distribution of the strain fields, magnitude of the Burgers vectors, dislocation senses, and surface relaxation effects, can also be accurately determined and described by these techniques.

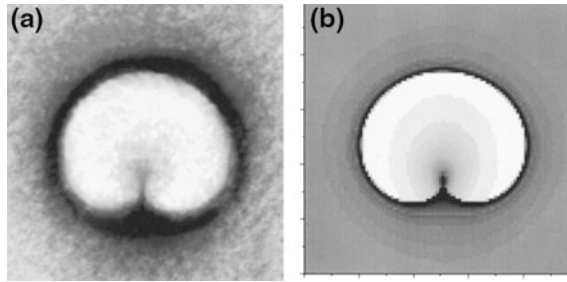


Fig. 2.33 **a** Synchrotron white beam X-ray topography image recorded in the back-reflection geometry from a (0001) Lely platelet showing a pair of opposite-sign screw dislocations. **b** Simulated image of two opposite-sign screw dislocations with 30- μm spacing. The image dimensions are $200 \times 200 \mu\text{m}^2$. Reprinted with permission from [88]. Copyright 1999, AIP Publishing LLC

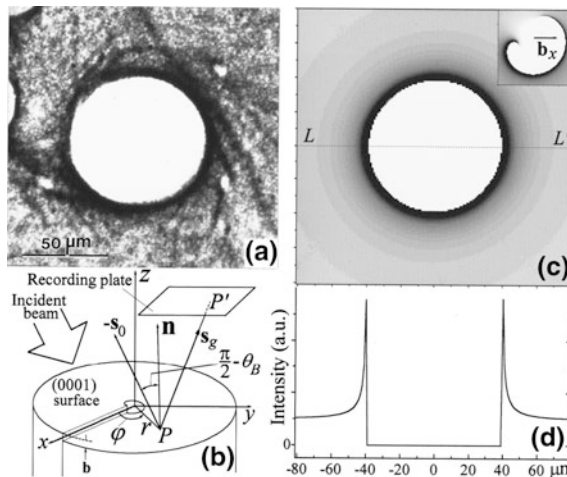


Fig. 2.34 **a** Synchrotron back-reflection topographic image of an 8c micropipe under diffraction conditions $g = 00024$ (and its harmonics), $\theta_B = 81.4^\circ$, and sample-to-film distance equal to 20 cm. **b** Diffraction geometry. **c** Simulation of an 8c superscrew dislocation. The inset corresponds to the simulation of a mixed dislocation. **d** Radial diffraction intensity profile of (c). Reprinted with permission from [89]. Copyright 1999, AIP Publishing LLC

2.4.3 Stacking Faults

Stacking faults are segments in the SiC crystal where rows of Si–C bilayers deviate from the perfect stacking sequence (along c -axis) of the crystal. The defects in single crystalline and polycrystalline SiC are examined by transmission electron microscopy, and the result shows that dislocations are not as common as stacking faults [90]. Dislocations have been observed from nearly all the materials examined (Fig. 2.35). The observed stacking faults are either “stress-induced” extrinsic

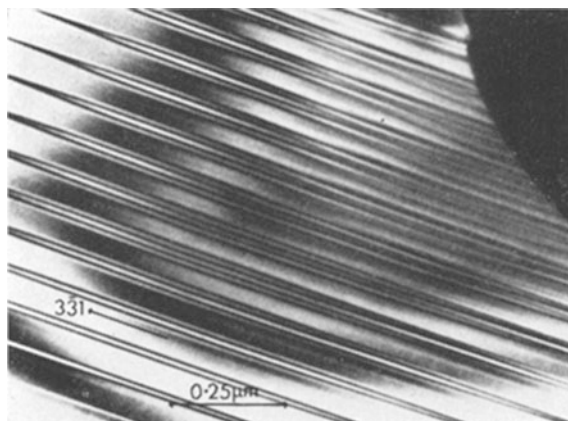


Fig. 2.35 TEM image of the regularly spaced stacking faults in hot-pressed SiC. Reprinted with permission from [90]. Copyright 1972, Springer Science and Business Media

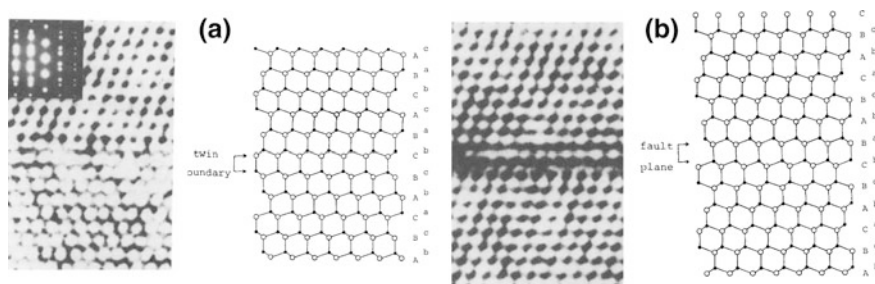
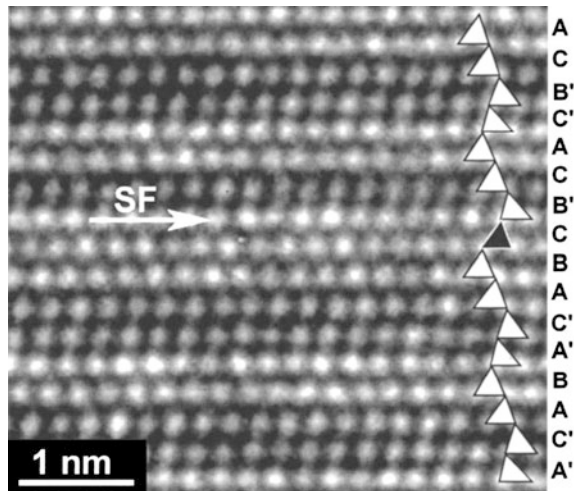


Fig. 2.36 High-resolution TEM images of **a** twin stacking fault and **b** deformation stacking fault found in β -SiC ceramics sintered at 2,000 °C. The right panel shows the structural models based on the stacking sequence. Reprinted with permission from [91]. Copyright 1989, Wiley-VCH Verlag GmbH & Co. KGaA

or “grown-in” intrinsic ones. The stacking fault energy is measured to be 1.9 ergs/cm² by the extended node method. The structure of the stacking faults in β -SiC has been investigated by high-resolution transmission electron microscopy (HRTEM) [91]. The HRTEM images of the stacking faults in a specimen sintered at 2,000 °C along with their structure models are shown in Fig. 2.36. There are many twin boundaries with nearly perfect atomic arrangement in each twinned domain. The result shows that the stacking faults initially present in the β -SiC powders are eliminated as grain growth proceeds at elevated temperature.

The effects of stacking faults on the X-ray diffraction profiles of β -SiC powders have been studied by simulation with supercells of up to 100 times the volume of a conventional unit cell [92]. Stacking faults in β -SiC powders give rise to all the features observed from the diffraction pattern, that is, an additional peak at $d = 0.266$ nm, a high background intensity around the peak at $d = 0.252$ nm, and broadening of the β -SiC peaks. The simulation also indicates that the distribution

Fig. 2.37 High-resolution TEM image of a stacking fault (marked by *arrow*) in a 4H-SiC diode. Reprinted with permission from [94]. Copyright 2002, AIP Publishing LLC



of the faults is not uniform, although a unique description of the fault population is not available. The deformed 4H- and 6H-SiC single crystals by compression at 1,300 °C have been investigated [93]. All the deformation-induced dislocations are dissociated into two partials bounding a ribbon of intrinsic stacking fault. Using transmission electron microscopy, the stacking fault energy is determined from the separation width of the two partials of dissociated dislocations. It is $14.7 \pm 2.5 \text{ mJ m}^{-2}$ for 4H-SiC, and $2.9 \pm 0.6 \text{ mJ m}^{-2}$ for 6H-SiC. The calculated stacking fault energies based on the axial next-nearest-neighbor Ising spin model are within 5 and 40 % of the experimental values for 6H- and 4H-SiC, respectively.

The structure of the stacking faults formed in forward-biased 4H- and 6H-SiC $p\text{-}n^-$ diodes is investigated by transmission electron microscopy [94]. The typical fault densities are between 10^3 and 10^4 cm^{-1} , and analysis of the stacking sequences (Fig. 2.37) and partial dislocations bounding the faults indicates that the faults are isolated single-layer Shockley ones bounded by partial dislocations. The stacking faults formed during forward biasing of 4H-SiC $p\text{-}i\text{-}n$ diodes are identified using light emission imaging and transmission electron microscopy [95]. These faults may have either faulted dislocations or faulted dislocation loops, and the leading partial dislocations of the faulted loops may have either carbon cores or silicon cores, whereas the partials of faulted dislocations are silicon cores. These stacking faults seem to relieve both tension and compression during $p\text{-}i\text{-}n$ diode operation, indicating the presence of a complex inhomogeneous strain field within the diode. The formation and growth of the stacking faults causing degradation in bipolar $p\text{-}i\text{-}n$ diodes are studied by electrical, optical, and structural techniques [96], and there are at least three origins for the stacking fault formation, giving rise to faults with different characteristics.

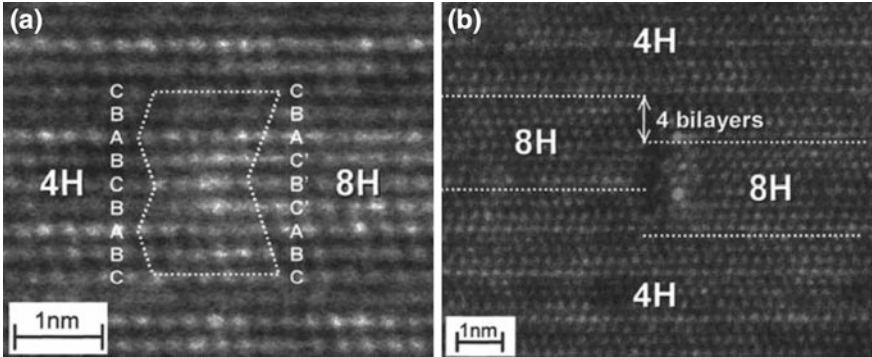


Fig. 2.38 High-resolution TEM images of the stacking faults in the 4H-SiC epilayer. Reprinted with permission from [97]. Copyright 2005, AIP Publishing LLC

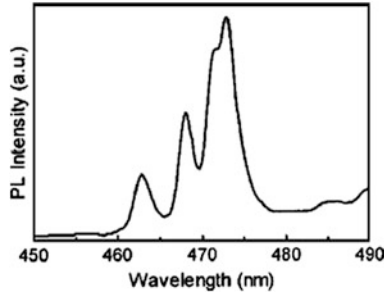


Fig. 2.39 PL spectrum of an in-grown stacking fault in the 4H-SiC epilayer acquired at 9 K excited by the 325-nm line. The four peaks are at 463.1, 468.3, 471.8, and 473.1 nm. Reprinted with permission from [97]. Copyright 2005, AIP Publishing LLC

The structure of in-grown stacking faults in 4H-SiC (0001) epilayers prepared by chemical vapor deposition has been investigated [97]. The in-grown stacking faults nucleate near the substrate/epilayer interface and expand with increasing epilayer thickness in a triangular shape. Transmission electron microscopy confirms that the in-grown stacking fault is the 1c of 8H polytype (Fig. 2.38). The low-temperature PL spectrum obtained from the same area (absent in other areas) exhibits four peaks at 463.1, 468.3, 471.8, and 473.1 nm (Fig. 2.39) corresponding to phonon replicas with a bandgap of 2.710 eV, and this confirms the 8H polytype. The epilayers prepared under the conditions of slow growth rate, high temperature, and improved substrate surface have reduced densities of in-grown stacking faults. The density, shape, and structure of the in-grown stacking faults in 4H-SiC (0001) epitaxial layers are investigated by cathodoluminescence, photoluminescence, and transmission electron microscopy [98]. The in-grown stacking faults have the 8H structure (Fig. 2.40) and exhibit a photoluminescence peak at 2.56–2.70 eV. The stacking faults in the Schottky barrier diode lower the barrier height and decrease the breakdown voltage. The stacking faults in 4H-SiC epilayers are studied by

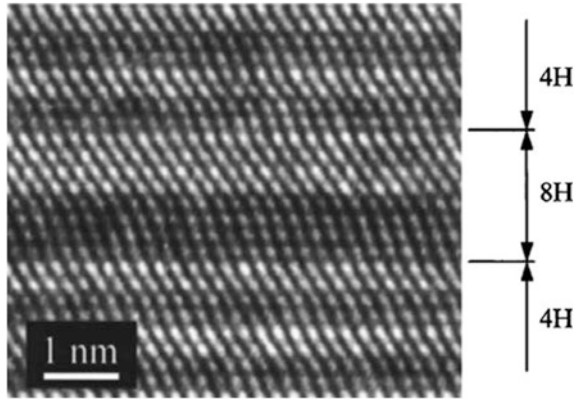


Fig. 2.40 Cross-sectional HRTEM image of an in-grown stacking fault in the 4H-SiC epilayer prepared by chemical vapor deposition. Reprinted with permission from [98]. Copyright 2005, AIP Publishing LLC

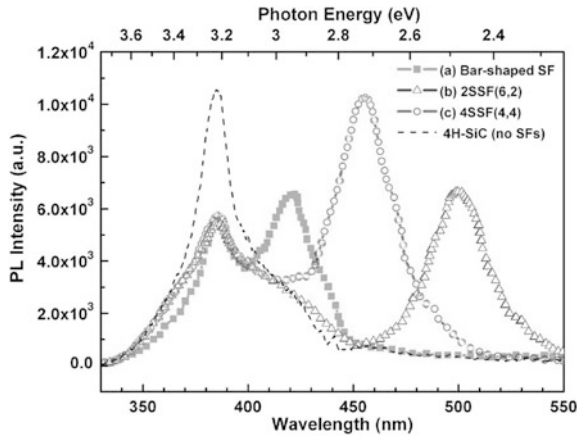


Fig. 2.41 PL spectra obtained from the 4H-SiC epilayer in the areas of: **a** bar-shaped (intrinsic Frank) stacking fault, **b** double Shockley stacking fault (2SSF), and **c** in-grown stacking fault (4SSF). The spectrum acquired from the area without stacking faults (SFs) is shown by the *dashed line*. Reprinted with permission from [99]. Copyright 2008, AIP Publishing LLC

microphotoluminescence spectroscopy and photoluminescence intensity mapping [99]. Three types of stacking faults, namely intrinsic Frank, double Shockley, and in-grown stacking faults, are identified. Each kind of stacking fault shows distinct PL located at 420 nm (intrinsic Frank), 500 nm (double Shockley), and 455 nm (in-grown), respectively (Fig. 2.41). The area without stacking faults shows PL with a peak at 386 nm (close to 4H-SiC bandgap) accompanied by a tail on the low-energy side. The shape and distribution of the stacking faults can be profiled by micro-PL intensity mapping (Fig. 2.42).

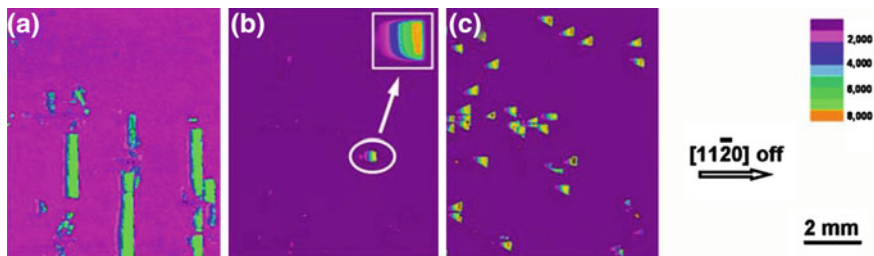
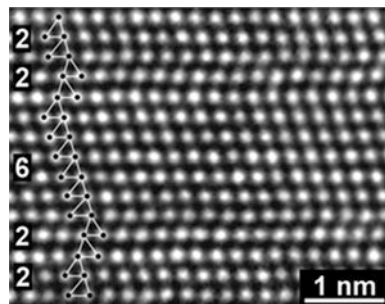


Fig. 2.42 PL intensity mapping of the 4H-SiC epilayer at **a** 420 nm, **b** 500 nm, and **c** 455 nm. Reprinted with permission from [99]. Copyright 2008, AIP Publishing LLC

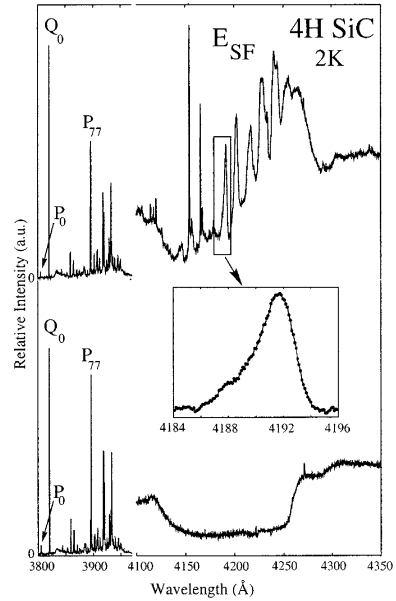
Fig. 2.43 HRTEM image of a stacking fault in the heavily doped *n*-type 4H-SiC crystal. Reprinted with permission from [100]. Copyright 2002, AIP Publishing LLC



The formation and expansion mechanism of stacking faults have been explored. Spontaneous formation of stacking faults is observed from heavily nitrogen-doped ($n > 1 \times 10^{19} \text{ cm}^{-3}$) 4H-polytype SiC crystals by transmission electron microscopy [100]. Faults are present in the as-grown boules and additional faults are generated by annealing in argon at 1,150 °C. All the faults have an identical structure consisting of six layers stacked in a cubic sequence embedded in the 4H-SiC crystal (Fig. 2.43). The stacking faults result from two Shockley partial dislocations gliding on two neighboring basal planes of SiC. The energy of the 4H-SiC with faults may be lower than that of the perfect heavily doped crystal at typical processing temperatures, and this explains the structural transformation. Detailed study shows that the structural transformation is caused by the quantum-well action [101], the electrons in highly *n*-type 4H-SiC enter stacking fault-induced quantum-well states to lower the system energy. The net energy gain derived from the charge neutrality equation shows a dependence on the temperature and nitrogen doping concentration. Doping concentrations in excess of $3 \times 10^{19} \text{ cm}^{-3}$ should result in spontaneous formation of double-layer stacking faults at the device-processing temperatures, in agreement with observations. Charge buildup in the stacking faults can produce an electrostatic potential that increases the forward voltage drop in SiC *p-i-n* diodes.

The driving force of stacking fault expansion in 4H-SiC *p-i-n* diodes is investigated by optical emission microscopy and transmission electron microscopy

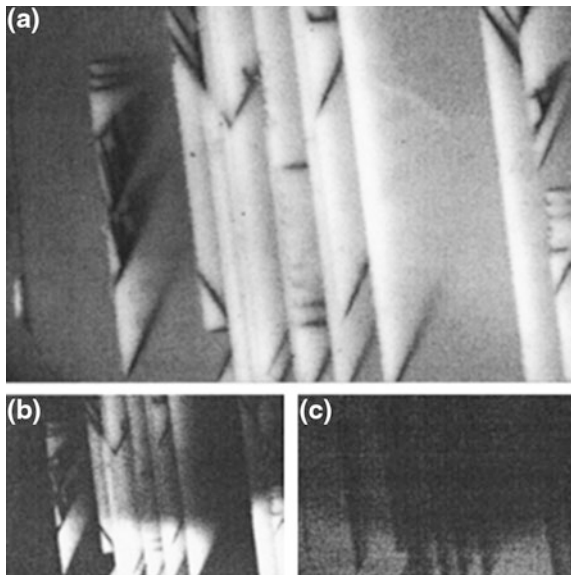
Fig. 2.44 PL spectra of a stressed (*top*) and nonstressed (*bottom*) 4H-SiC diode acquired at 2 K. P_0 , Q_0 , and P_{77} are the nitrogen-bound exciton lines. A new set of lines labeled E_{SF} appear in the PL spectrum of the stressed diode between 410 and 435 nm. Reprinted with permission from [104]. Copyright 2001, AIP Publishing LLC



[102]. The stacking fault expansion and properties of partial dislocations are inconsistent with stress as the driving force. Instead, the thermodynamic free-energy difference between the perfect and fault structure is suggested as the driving force for stacking fault formation in the diodes. This implies that the hexagonal polytypes of SiC may be metastable at room temperature and may transform to a fault structure if the activation energy of the partial dislocation glide is available. This activation energy can be provided by the electron-hole recombination during operation of the diodes. The nucleation and expansion of stacking faults induced by recombination in 4H- and 6H-SiC epitaxial films have been studied in detail [103]. The activation energy for partial dislocation glide under optical excitation decreases to about 0.25 eV, about 2 eV lower than that for pure thermal activation. The low activation threshold is in good agreement with the observation in forward-operating p - n -junction devices, implying that radiation enhanced dislocation glide is a general phenomenon in hexagonal SiC. The elementary process controlling expansion of stacking faults is supposed to be kink pair nucleation aided by the phonon-kick mechanism, based on thermal activation and below-gap excitation spectroscopy of dislocation glide.

Stacking faults can be regarded as a quantum well sandwiched between the normal silicon carbide crystals and the quantum states and energy levels of the stacking faults can be evaluated. The calculated and experimental data provide the basis to understand the formation and properties of stacking faults. A unique luminescence band belonging to the stacking fault is observed from the 4H-SiC bipolar diode after extended forward voltage operation [104]. As shown in Fig. 2.44, a series of lines located between 410 and 435 nm (E_{SF}) is present in the

Fig. 2.45 **a** Panchromatic cathodoluminescence image of the stressed 4H-SiC diode showing stacking faults. Cathodoluminescence image of the same diode at **b** 425 nm and **c** 390 nm. Reprinted with permission from [104]. Copyright 2001, AIP Publishing LLC



PL spectrum of the stressed diode but absent in the nonstressed one. The panchromatic cathodoluminescence image (Fig. 2.45a) of the stressed diode contains triangular features that are assigned to the stacking faults. The triangular regions are brighter in the image acquired with a monochromator at 425 nm (Fig. 2.45b), indicating that the E_{SF} emission stems from the entire stacking faults. The band-edge luminescence at 390 nm within the stacking faults is suppressed (Fig. 2.45c), implying competition between two recombination processes. The measured E_{SF} decay time is between 7 and 470 ns and has the same order as that of the intrinsic exciton in 4H-SiC. The E_{SF} emission is attributed to the exciton recombination at the quantum well created by the stacking fault.

The stacking fault-like quantum wells in SiC crystals can be created intentionally. Multiple quantum well structures with 3C-SiC wells between 4H-SiC barriers (consisting of more than 20 heterojunctions) are fabricated by a two-step procedure using solid source molecular beam epitaxy [105]. The structures are produced by selective nucleation of wire-like 3C-SiC nuclei on the terraces of well-prepared hexagonal SiC (0001) substrates followed by a step flow of both the 3C wires and surrounding hexagonal SiC materials (Fig. 2.46). The thickness of the 3C-SiC quantum well is about 2.3 nm (corresponding to three unit cells in $\langle 111 \rangle$ direction), thus giving rise to spatial quantization of electrons. The PL spectrum obtained at 6 K shows dominant L_1 emission line related to the D_1 center (attributed to 4H-SiC) as well as an additional band at around 2.26 eV (Fig. 2.47). These new lines can be explained by a model of a triangular electron quantum well in 3C-SiC.

Low-temperature photoluminescence in 4H/3C/4H-SiC single quantum wells in the 20–50- μm -thick 4H-SiC epitaxial film has been investigated [106]. The

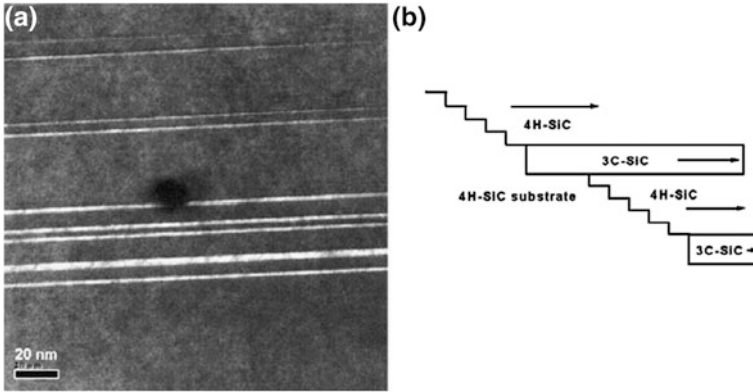
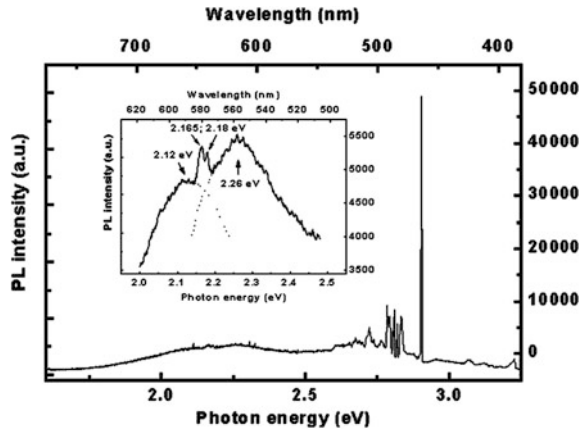


Fig. 2.46 **a** TEM image of the 3C/4H-SiC multiple quantum well structure fabricated on 4H-SiC(0001) by step-controlled epitaxy. **b** Schematic illustration of the formation process of the structure on a tilted substrate. Reprinted with permission from [105]. Copyright 2001, Elsevier

Fig. 2.47 PL spectrum of the 3C/4H-SiC multiple quantum well structure. The *inset* shows the magnified region between 2 and 2.5 eV. Reprinted with permission from [105]. Copyright 2001, Elsevier



quantum well is 3.25 nm thick consisting of thirteen 3C-SiC bilayers as revealed by high-resolution transmission electron microscopy (Fig. 2.48). Figure 2.49 shows a portion of the PL spectrum taken from the same area where the TEM image is taken. In this region, four well resolved peaks between 580 and 600 nm are observed but they are absent in a normal 4H-SiC film. The energy separation between these peaks is approximately equal the energy difference between the four major phonons in 3C-SiC and thus is phonon replicas. An effective exciton energy gap of about 2.177 eV (for the 3C quantum well) is derived, and it is more than 200 meV below the usual exciton bandgap of bulk 3C-SiC as a result of Stark effect due to the built-in electric field in the quantum well in conjunction with the quantum confinement effect. Calculation shows a strong internal electric field on the order of 1 MV/cm to satisfy the observed large red shift of PL, and this field is

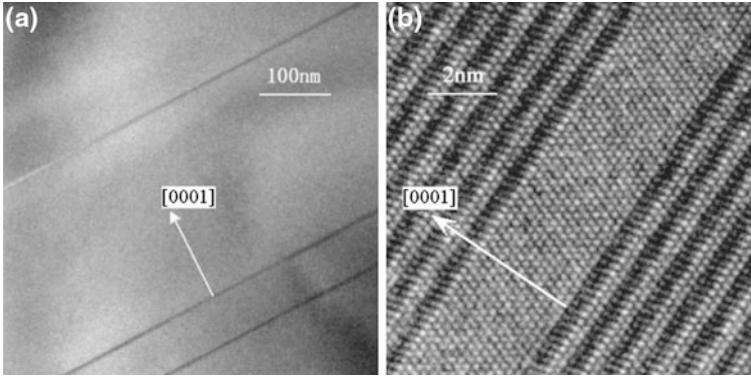
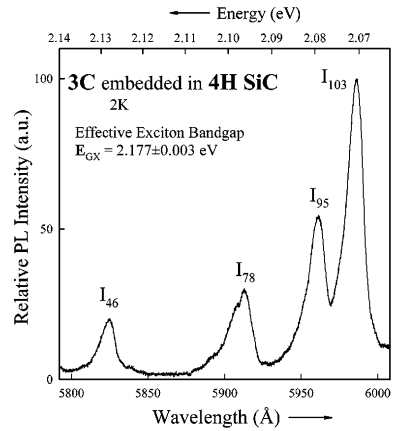


Fig. 2.48 **a** TEM image and **b** high-resolution TEM image of the cross section of an undoped 4H-SiC epitaxial film with 3C inclusions. Reprinted with permission from [106]. Copyright 2003, AIP Publishing LLC

Fig. 2.49 PL spectrum of the 4H-SiC epitaxial film with 3C-SiC inclusions acquired at 2 K. The subscript of the marked lines denotes the momentum-conserving phonon energy in meV. Reprinted with permission from [106]. Copyright 2003, AIP Publishing LLC



proposed to arise from the difference in spontaneous polarization between 3C- and 4H-SiC.

The study using ballistic electron emission microscopy in ultrahigh vacuum indicates that annealing of 4H-SiC wafer in dry oxygen at 1,150 °C for 90 min can produce double stacking faults 3C-SiC inclusions [107]. Distinctive quantum-well structures corresponding to individual inclusions are observed. The two-dimensional quantum-well conduction-band minimum is determined to be approximately 0.53 eV below the conduction-band minimum of bulk 4H-SiC. Macroscopic diode I - V and microscopic ballistic electron emission microscopy measurements indicate that there is little variation in the interface state density or fixed charge across the inclusions. The study of the electronic properties of single- and double-layer stacking faults in 4H-SiC clarifies the apparent distinctions of recombination-enhanced defect reactions at these faults [108]. Photoluminescence imaging

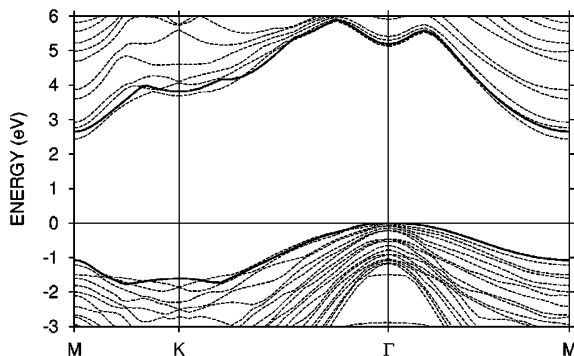


Fig. 2.50 Band edges of 4H-SiC near the fundamental gap projected on the Γ -M-K basal plane calculated by the first-principle method (*solid lines*). The dashed lines show the band-structure results of the model containing the stacking faults. Reprinted with permission from [109]. Copyright 2001, AIP Publishing LLC

spectroscopy and deep-level transient spectroscopy reveal the key constituents of radiative recombination and provide evidence of the nonradiative centers at $E_V + 0.38$ eV responsible for the recombination-enhanced mobility of Si-core partial dislocations. This energy-level model allows the qualitative description of the recombination activity at different types of stacking faults and bounding partial dislocations.

Several groups have theoretically studied stacking faults by first-principle calculation. The first-principle calculation is performed on the stacking faults in 4H-SiC [109]. An interface band in the gap with a maximum depth of 0.2–0.3 eV below the conduction-band minimum at the \bar{M} point is obtained (Fig. 2.50) because the local environment resembles that of the lower gap 6H polytype. The formation energies of the stacking faults in 3C-, 4H-, and 6H-SiC are on the order of a few meV/pair. Hence, the thermodynamic driving force results in growth of the stacking faults in an n -type sample. Nonradiative recombination of electrons trapped at the stacking fault with holes provides the necessary energy to overcome the partial dislocation motion barriers required to increase the stacking fault area in a device under forward bias. This explains the observed increase in stacking faults in SiC devices under long-time forward bias operation as well as degradation of the devices by the negative effects of trapping electrons on transport. Trapping of electrons in the stacking fault interface states in 4H-SiC serves as a driving force for growth of stacking faults, because the energy to create the additional stacking fault area is offset by energy gained by capturing electrons in an interface localized state below the conduction band [110]. Screening significantly reduces the potential barrier (for electrons) adjacent to the quantum well.

The structurally different stacking faults that can be introduced by glide along the (0001) basal plane in 3C-, 4H-, and 6H-SiC have been studied based on local density approximation using the density functional theory [111–113]. The band-structure calculation reveals that both types of stacking faults in 4H-SiC and two of

the three different types of stacking faults in 6H-SiC induce quasi-two-dimensional energy states in the bandgap at about 0.2 eV below the conduction-band minimum, thus being electrically active in *n*-type SiC [111]. The third type of stacking faults in 6H-SiC and the only stacking fault in 3C-SiC do not give rise to states clearly separated from the band edges, but instead produce rather strongly localized states with energies very close to the band edges [112]. Figure 2.51 displays the calculated band structure of the perfect 6H-SiC and the 6H-SiC containing stacking faults. There are three types of stacking faults in 6H-SiC that can be introduced by dislocation glide: stacking fault (42), defined as (A|CABAC) inside the faulted cell, stacking fault (3111), defined as (AB|ABAC), and stacking fault (24), defined as (ABC|BAC). Herein, “|” denotes the slip plane. Strong localization of the stacking fault gap state wave function is within roughly 10–15 Å perpendicular to the stacking fault plane. This quantum-well-like feature of certain stacking faults in SiC can be understood in terms of the remarkable conduction-band offsets between cubic and hexagonal polytypes. The stacking fault energies are also calculated using the supercell method and axial next-nearest-neighbor Ising model method. Both calculated results agree well with the measured low stacking fault energies determined experimentally. The 4H-SiC that contains two, three, and four stacking faults in neighboring glide planes has also been investigated [113]. The structural defects can be viewed as thin 3C-like inclusions in the 4H-SiC matrix. The stacking fault energy of two stacking faults in adjacent basal planes is reduced by approximately a factor of 4 relative to that of one isolated stacking fault. This implies that double stacking faults (3C-like inclusions 1.25 nm in thickness) may be quite common in 4H-SiC.

2.4.4 Impurities

Nitrogen donor is an important impurity in silicon carbide, and it has been intensively studied. Boron and nitrogen impurities in 6H-SiC single crystals have been studied by electron spin resonance spectroscopy [114] and both impurities substitute for carbon and occupy the three nonequivalent carbon sites with equal probability. The hyperfine structure is well resolved for both species. The nitrogen hyperfine structure is interpretable in terms of some *s* character for the unpaired electron, whereas the boron hyperfine structure indicates predominantly *p* character. Infrared absorption and Hall effect measurements are utilized to study nitrogen-doped 6H-SiC single crystals [115]. Three sets of infrared absorption lines are observed and attributed to transitions from the $1s(A_1)$ and $1s(E)$ ground states to $2p_0$, $2p_{\pm}$, $3p_0$, and $3p_{\pm}$, excited states of the nitrogen donors on the *h* lattice site of 6H-SiC and from $1s(A_1)$ to $2p_{\pm}$ and $3p_{\pm}$ states of the nitrogen donors on k_1 and k_2 lattice sites. The ground-state binding energies of these donor species are 81.0, 137.6, and 142.4 meV, respectively. The *h* donor center exhibits valley-orbit splitting of 12.6 meV. Figure 2.52 shows the schematic of the energy levels of the nitrogen donors residing at *h*, k_1 , and k_2 lattice sites as determined from infrared

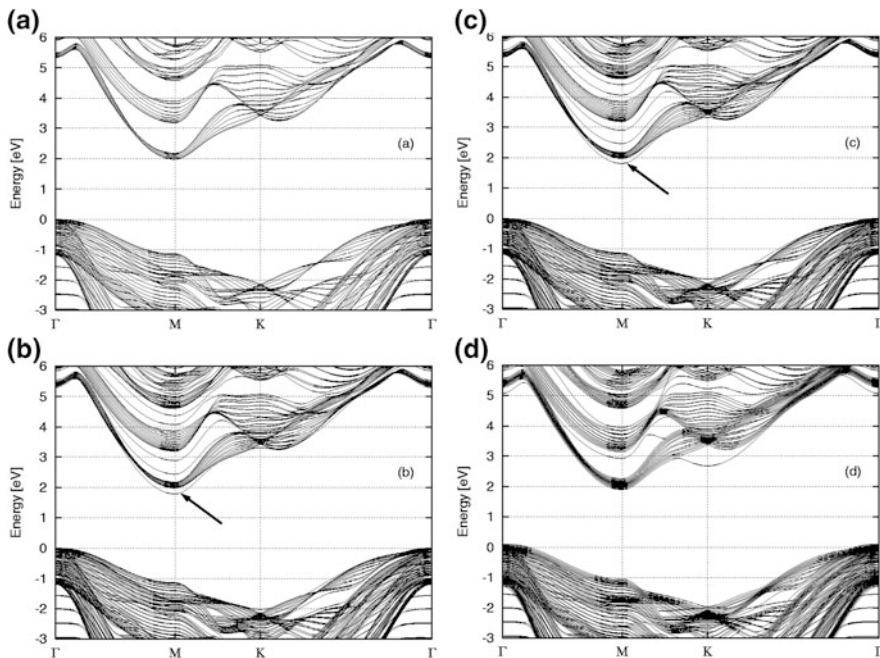


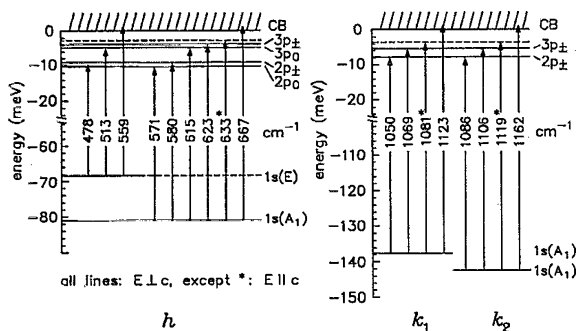
Fig. 2.51 Kohn-Sham band structure of the 96 atom supercells for **a** perfect 6H-SiC, **b** with stacking fault (42), **c** with stacking fault (24), and **d** with stacking fault (3111). The arrows point to the split-off bands below the conduction band caused by the stacking fault. Reprinted with permission from [112]. Copyright 2003, American Physical Society

spectra. The transverse and longitudinal effective electron masses are 0.24 ± 0.01 and $0.34 \pm 0.02 m_0$, respectively, as obtained by fitting the effective-mass formalism to the observed transition energies. The energy positions of the ground and excited states of the nitrogen donor in the nitrogen-doped 4H-SiC are also investigated [116]. The two electrically active levels (Hall effect) and three series of absorption lines (infrared spectra) are assigned to two nitrogen donor species that substitute on the two inequivalent lattice sites (h , k) in 4H-SiC. The nitrogen donors on hexagonal sites (h) exhibit a valley-orbit splitting of the ground-state level of 7.6 meV. The energies of the excited states of both nitrogen donors are identified by effective-mass approximation assuming the transverse effective mass of $0.18 m_0$ and longitudinal effective mass of $0.22 m_0$.

Several other types of impurities have also been investigated. Trace impurities of vanadium (V) in the SiC crystals prepared by a modified Lely process are detected based on the strong and polytype-dependent photoluminescence in the 1.3–1.5- μm near-infrared region as well as by infrared absorption [117]. The spectra originate from the intra-3d-shell transitions ${}^2E(3d^1) \rightarrow {}^2T_2(3d^1)$ of $V_{Si}^{4+}(3d^1)$. Electron spin resonance spectroscopy reveals that V_{Si} in SiC serves as a deep acceptor and possibly also as a deep donor. The vanadium impurity is suggested to be able to reduce the minority carrier lifetime in SiC-based

Fig. 2.52 Energy levels of nitrogen donors residing at the h , k_1 , and k_2 lattice sites of nitrogen-doped 6H-SiC.

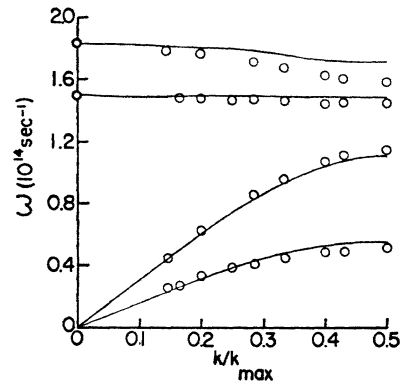
Reprinted with permission from [115]. Copyright 1992, AIP Publishing LLC



optoelectronic devices. Intense erbium luminescence around $1.54\ \mu\text{m}$ at 2–300 K is observed from Er^{3+} -implanted 4H-, 6H-, 15R-, and 3C-SiC samples [118]. The ion implant fluence is about 10^{13} erbium ions/ cm^2 , and the implanted samples are annealed at $1,700\ ^\circ\text{C}$. The most striking feature about the spectra is that the relative integrated intensity of the erbium luminescence is nearly constant from 2 to 400 K. This is different from the narrower gap semiconductors in which the $1.54\text{-}\mu\text{m}$ luminescence is observed to drop significantly. No major difference exists in the spectra of the hexagonal and rhombohedral polytypes, but there is a difference for cubic SiC. Hydrogen impurities in 3C-SiC have been studied theoretically based on ab initio density functional supercell calculation, employing the local density approximation [119]. The stable configurations and formation energies of various hydrogen and dihydrogen defects are calculated. The interstitial H is readily incorporated into the p -type 3C-SiC during growth and acts as a shallow donor compensating the acceptors. In n -type 3C-SiC, interstitial H_2 is more stable, but its formation energy is too high to allow for significant incorporation. $(V_C + \text{H})$ behaves as a hole trap and $(V_{\text{Si}} + \text{H})$ as an electron trap. The implanted hydrogen is favorably trapped by V_{Si} . The electron trap V_{Si} can be passivated by four hydrogen atoms but V_C remains a hole trap. Low-temperature hydrogen annealing of SiC introduces a sufficient amount of interstitial hydrogen for complete passivation of the p -type materials. In the n -type materials, the dominant defects are $(V_{\text{Si}} + n\text{H})$ electron traps that can reduce the free-carrier concentration. High-temperature annealing in hydrogen is effective in introducing hydrogen even to the n -type materials. It is suggested that some of the paramagnetic signals that have been assigned to pure vacancies may arise from $(V + n\text{H})$ complexes.

The microscopic and electronic structures of several important shallow donors and acceptors in 6H-, 4H- and 3C-SiC determined by electron paramagnetic resonance, electron nuclear double resonance, and optical absorption and emission spectroscopy have been well reviewed [120]. The electrical data obtained by deep-level transient spectroscopy on deep defect centers in the 3C-, 4H-, and 6H-SiC are summarized [31]. Emphasis is placed on intrinsic defect centers in the as-grown, ion-implanted, and electron-irradiated materials as well as on defect centers caused by doping of transition metals (vanadium, titanium, chromium, and scandium).

Fig. 2.53 Calculated phonon dispersion curves (*solid lines*) of cubic SiC in the $\langle 111 \rangle$ direction. The circles denote measured values obtained from Ref. [122] ($k_{\max} = 2\pi/a$). Reprinted with permission from [121]. Copyright 1969, American Physical Society



2.5 Lattice Vibration and Infrared/Raman Spectra

The lattice dynamical vibration properties of silicon carbide and associated infrared and Raman scattering characteristics have been extensively studied. The phonon dispersion curves in the various symmetry directions in cubic SiC are derived using a rigid ion model consisting of short-range central and noncentral interactions and long-range Coulombic interactions among ions with the appropriate effective ionic charges [121]. The calculated dispersion curve in the $\langle 111 \rangle$ direction (Fig. 2.53) is compared to Raman data acquired from various polytypes of SiC [122, 123], and the agreement between calculation and experiments is very good. The phonon density of states and Debye characteristic temperature of SiC are also derived. The adiabatic bond-charge model is applied to the 3C, 6H, 4H, and 2H polytypes of SiC [124]. The short-range elastic forces are described by two-body and three-body interactions among silicon ions, carbon ions, and bond charges, whereas the long-range Coulomb forces are taken into account by the Ewald technique. The model parameters are fitted to the frequencies obtained from Raman and luminescence measurements. The resulting phonon dispersion curves along the high symmetry lines in the fcc and hexagonal Brillouin zone agree with experimental results. In the 3C case, the calculation yields the same eigenvectors as *ab initio* calculation. The independent elastic constants of the different polytypes are derived using the resulting sound velocities, and they agree reasonably well with experimental ones. The plane-wave pseudopotential approach of the density functional theory employing the local density approximation is used to study the ground-state properties of the 3C, 2H, and 4H polytypes of SiC [125]. The linear response theory within the density functional theory is employed to determine the dynamic lattice properties of 3C-SiC. The phonon dispersion curves of cubic SiC are intermediate between those of Si and diamond but not average and consistent with measured values (Fig. 2.54). The phonon dispersion curves of 2H- and 4H-SiC are also derived. The calculated ground-state properties of the cubic 3C and hexagonal 2H and 4H

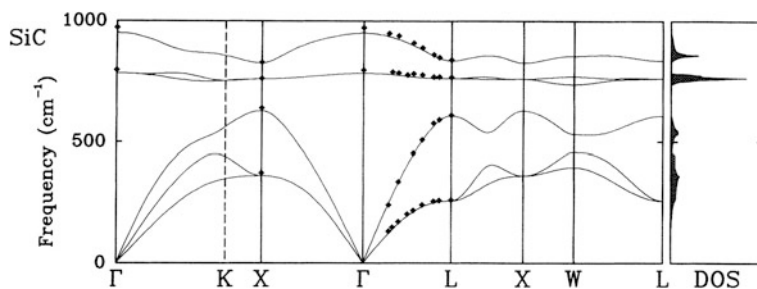
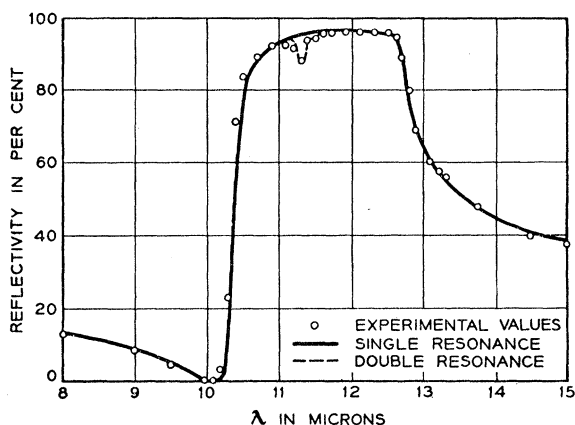


Fig. 2.54 Calculated phonon dispersion curves and density of states (DOS) of 3C-SiC. The diamond signs denote the experimental first-order Raman scattering data obtained from Ref. [123]. Reprinted with permission from [125]. Copyright 1994, American Physical Society

Fig. 2.55 Reflectivity versus wavelength of the extraordinary ray in α -II SiC. The circles denote measured values and the solid line is the calculated curve. Reprinted with permission from [126]. Copyright 1959, American Physical Society



polytypes of SiC are quite similar, especially concerning ground-state energies and volumes as well as the valence charge densities along the bonding and stacking directions. In contrast to elemental crystals like Si and diamond, SiC has noticeable ionicity, that is, charge asymmetry. The employed calculation procedure has limitations in that it neglects the effects of the vibrational energy and crystal entropy.

Infrared spectroscopy imparts information about the lattice vibration properties of various polytypes of silicon carbide. The infrared transmission and reflectivity of several hexagonal SiC crystals in the 1–25- μm spectral region have been measured [126], and the reflectance spectra of both ordinary and extraordinary rays have been obtained (Figs. 2.55 and 2.56). Resonance occurs at 12.60 and 12.73 μm , respectively, and based on the reflectivity data, the high-frequency dielectric constant is calculated to be 6.7. The reflectance spectra can be fitted within experimental errors by the classical dispersion theory using the properly selected dispersion parameters, and the low frequency dielectric constant is derived to be 10.0 accordingly. The study of the surface effect suggests that

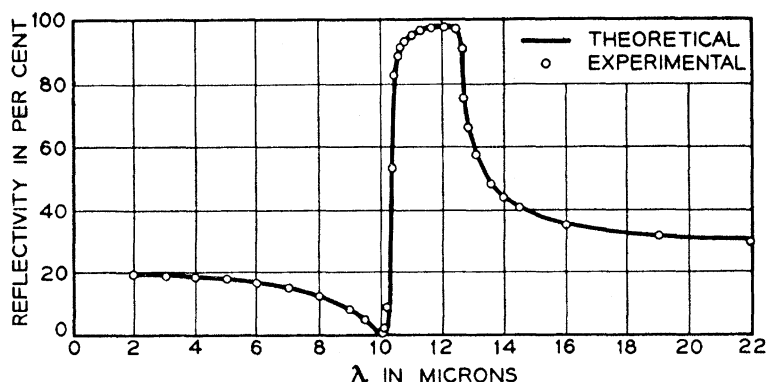


Fig. 2.56 Reflectivity versus wavelength of the ordinary ray in α -II SiC. The circles denote measured values and the solid line shows the calculated curve. Reprinted with permission from [126]. Copyright 1959, American Physical Society

reflectivity is an intrinsic property of the crystal. The absorption coefficient is derived as a function of wavelength in the range 1–10 μm based on the transmission measurement data. The transmission and reflection of 3C-SiC films are investigated in the 1–15- μm range [127], and the results are analyzed by the classical dispersion theory. The dispersion parameters for the fundamental resonance at 12.60 μm are essentially the same as those of the ordinary ray in the hexagonal α -II SiC. The measured and calculated transmission and reflection spectra are displayed in Fig. 2.57. In the immediate region of resonance, the agreement between theory and experiments is very good for both transmission and reflection. However, at the shorter wavelengths, the theory predicts higher transmission values and smaller reflection values because other absorption mechanisms such as free-carrier absorption are neglected in the theoretical treatment.

Multiple phonon absorption processes also occur in silicon carbide. The featured infrared absorption bands obtained from SiC have been interpreted as arising from multiple phonon absorption [128]. The phonon energies obtained by measuring the indirect interband absorption in SiC are 0.045 eV (TA), 0.067 eV (LA), 0.0955 eV (TO), and 0.1055 eV (LO). The ten infrared absorption peaks in the energy range of 0.130–0.300-eV stem from multiple phonon absorption, and Fig. 2.58 depicts a part of the infrared absorption spectrum. The four predicted summation bands show good agreement with the corresponding peaks of the measured spectrum.

Since the infrared reflection spectrum depends on many sample parameters, the infrared spectra of SiC films can provide useful information about the status of the films. Several unusual features are present in the infrared reflection spectra of CVD SiC films concerning the surface roughness and possible conducting layers at the film–substrate interface [129]. The free-carrier concentration and thickness of the film can be determined from the reflectance extrema. These values show good agreement with the values obtained by other methods, and hence, infrared reflectance measurement can nondestructively assess the fabricated films. Spectral

Fig. 2.57 Transmission and reflection of a 0.06- μm -thick β -SiC film. Reprinted with permission from [127]. Copyright 1959, American Physical Society

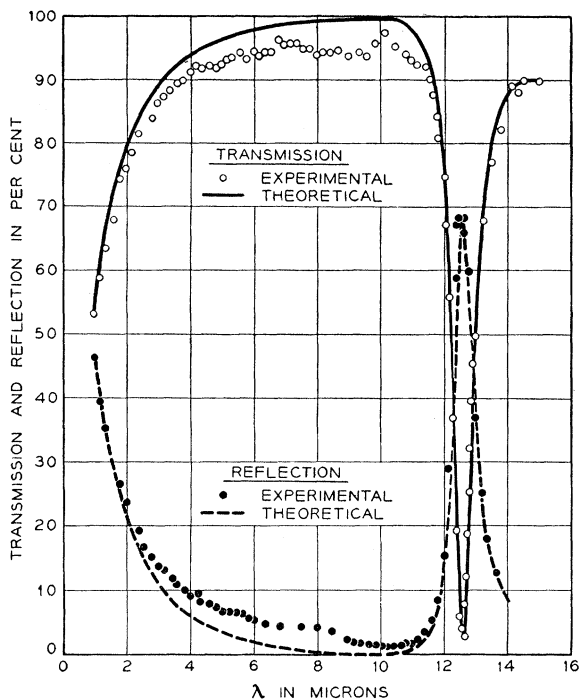
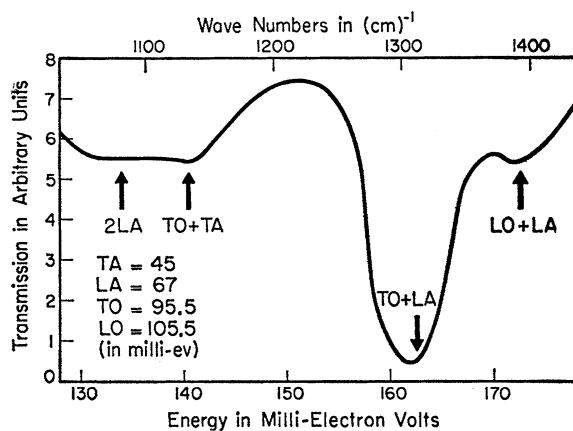
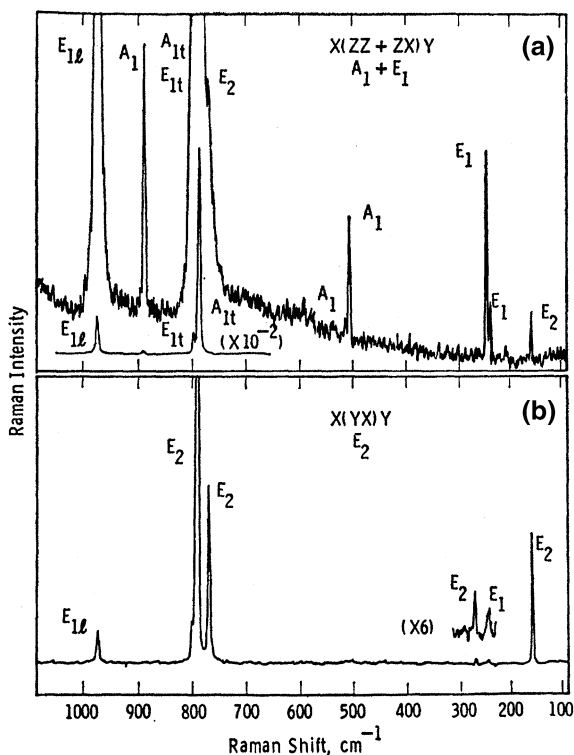


Fig. 2.58 Two-phonon optical acoustical summation bands in the infrared spectrum of SiC. The arrows point to the energy values calculated using the four assigned phonon energies. Reprinted with permission from [128]. Copyright 1961, American Physical Society



analysis may also reveal the crystal anisotropy, as demonstrated by the polarized infrared reflectivity spectra of 6H-SiC single crystals at different incident angles [130]. A sharp line in the reststrahl band is observed from the extraordinary ray, and its line shape depends on the incident angle. Numerical calculation based on a Lorentz oscillator model demonstrates that this sharp line arises from the crystal anisotropy of 6H-SiC suggesting that the infrared reflectivity of many anisotropic

Fig. 2.59 Full one-phonon emission Raman spectrum of 6H-SiC crystal with arrangements permitting **a** A_1 and E_1 modes, and **b** E_2 modes. Reprinted with permission from [122]. Copyright 1968, American Physical Society



solids may depend on the incident angle. Infrared ellipsometry is used to determine the free-electron concentrations in bulk and epitaxial nitrogen-doped 4H- and 6H-SiC [131] as well as epitaxial layer thickness. Data obtained from 6H-SiC can be modeled well if the large effective-mass anisotropy is taken into account, whereas effective-mass anisotropy has no noticeable effects on the 4H-SiC spectra. The two-phonon interaction influences the line shape in the region between 1,300 and 1,700 cm^{-1} and should be considered in calculating the free-carrier concentration.

Raman scattering conveys structural information about the lattice dynamical vibration properties of solids. Examination of Raman scattering in 6H-SiC crystals [122] revealed fifteen phonon-lines (Fig. 2.59). Polarized light is used to identify the mode symmetry, and the modes are classified by large zone analysis yielding dispersion like curves (Fig. 2.60). All observed narrow lines can be explained, and only two of the expected lines are not observed. Analysis of the dependence of phonon energy on propagation direction indicates that certain infrared and Raman active modes have extremely small infrared strength due to the specific polytype structure of 6H-SiC.

The first-order Raman spectra of more polytypes of SiC crystals, including 3C, 4H, 6H, 15R, and 21 R, have been acquired [123], and the phonon dispersion curves are established based on the Raman measurements. Overall, 9 lines are

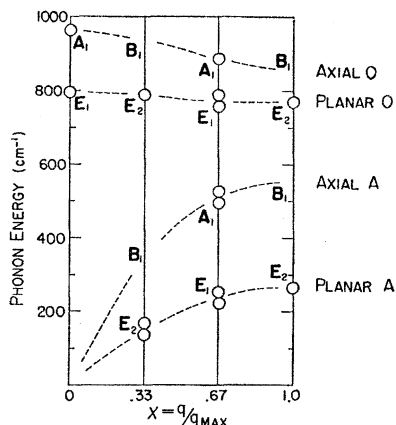
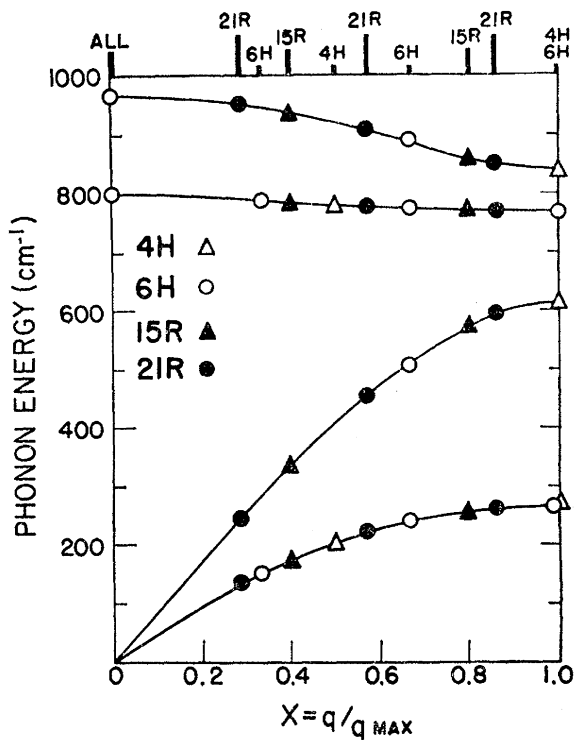


Fig. 2.60 Plot of experimental data of 6H-SiC in the form of dispersion curves in the large zone. The doublet separation is exaggerated. This figure is valid for weak modes for any phonon propagation direction and appropriate for strong modes only when the phonon propagation direction is along the c -axis. Reprinted with permission from [122]. Copyright 1968, American Physical Society

observed from 4H-SiC, 16 lines from 15R-SiC, and 14 lines from 21R-SiC. The symmetry of each phonon mode is determined by analyzing the polarization. The modes are classified using a standard large zone and then the positions of the three groups of one-phonon lines and 15 previously observed lines in 6H-SiC are assembled in a single large zone (Fig. 2.61). This assignment results in a set of SiC phonon dispersion curves confirming the existence of a common phonon spectrum for all SiC polytypes in the axial direction. The velocities of the longitudinal and transverse acoustic phonon waves derived from the dispersion curves are in good agreement with experimental results.

A theoretical method based on bond polarizability is adopted to calculate the Raman intensity profiles of the folded modes of silicon carbide [132]. The relative Raman intensity of the folded modes is calculated using bond Raman polarizability together with the eigenvectors of the linear-chain model. In this method, the bonds in a unit cell are classified into groups in which the individual Raman polarizability is equivalent. The Raman polarizability is expressed as the sum of the product of the bond Raman polarizability and relative displacement of the end atoms linked by the bond. The calculated Raman intensity profiles are in qualitative agreement with the experimental Raman spectra of the folded modes arising from TA and TO phonon branches along the c direction (Fig. 2.62). The calculated dispersion curves are compared to the measured ones in Fig. 2.63. The calculated frequencies of the TA branch are slightly smaller than the measured values, whereas there are slightly larger deviations from the measured values (as much as 20 cm^{-1}) for the TO branch at around the zone edge. The calculation may fit the experimental data better if the force constants between the second-neighbor planes are taken into account. The results indicate that measurement of the Raman frequencies and intensities is a useful technique for identifying the polytype structure of SiC.

Fig. 2.61 Combined dispersion curves based on measured Raman data obtained from four polytypes of SiC. The Raman accessible values of $x = q/q_{\max}$ are marked at the top of the figure. Reprinted with permission from [123]. Copyright 1968, American Physical Society



Raman scattering is utilized to evaluate SiC heteroepitaxial thin layers [133]. The heteroepitaxial layer of 3C-SiC can be grown on the (0001) surface of 6H-SiC platelets using conditions similar to those used to fabricate 3C-SiC on Si. The Raman spectra are acquired in the backscattering geometry using the 514.5-nm laser line at room temperature. The incident light is normal to the 3C (111) and 6H (0001) surfaces and polarized in a vertical plane. Figure 2.64 shows the TO and LO regions of the Raman spectra of the 6H-SiC sample before and after growth of the epitaxial layers. The intensity is normalized to the 6H-SiC main peaks at 789 cm^{-1} in the TO region and 967 cm^{-1} in the LO region. In the TO region, the intensity of the peak corresponding to the 3C-SiC TO phonon mode (796 cm^{-1}) increases after epitaxy, whereas in the LO region, the peak corresponding to 3C-SiC LO phonon mode (972 cm^{-1}) and the diminished peak of 6H LO phonon are observed. The layer thickness is about 10–15 μm , and the surface exhibits a single-crystal reflection high-energy electron diffraction pattern. The results indicate that the 3C-SiC (111) layer is heteroepitaxially grown on the 6H-SiC (0001) surface. This is understandable because that the atomic arrangements on the (111) plane of 3C-SiC and the (0001) plane of 6H-SiC are identical and the only structural difference between 3C in the [111] direction and 6H in the [0001] direction is the stacking order. Using a revised lattice dynamics model and the bond polarizability concept, the Raman intensity profiles in SiC polytypes are examined [134]. The

Fig. 2.62 Comparison between the measured and calculated Raman spectra of the folded TO modes of the four polytypes of SiC: **a** 15R, **b** 6H, **c** 21R, and **d** 8H. Reprinted with permission from [132]. Copyright 1986, American Physical Society

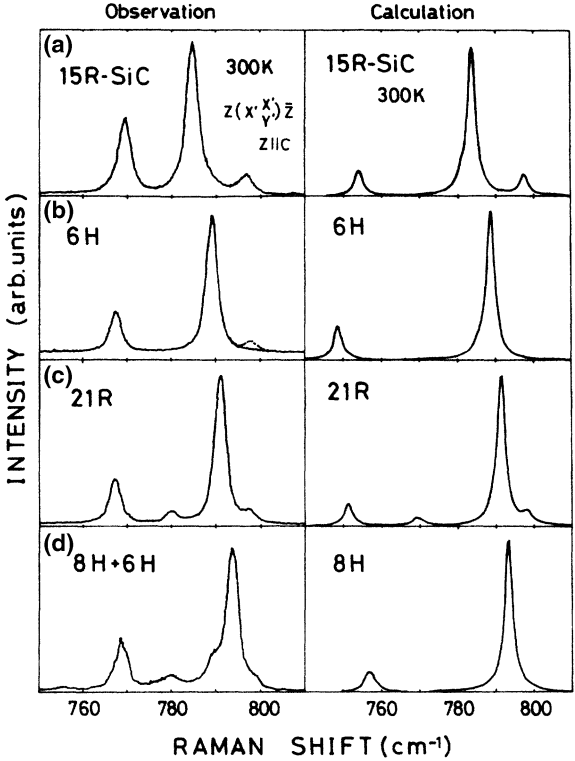


Fig. 2.63 Assembled phonon dispersion curves in the basic zone based on the data acquired from five polytypes of SiC. The *solid lines* are the calculated curves by the linear-chain model. Reprinted with permission from [132]. Copyright 1986, American Physical Society

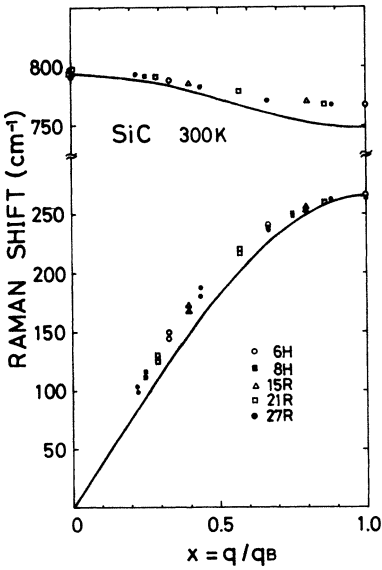
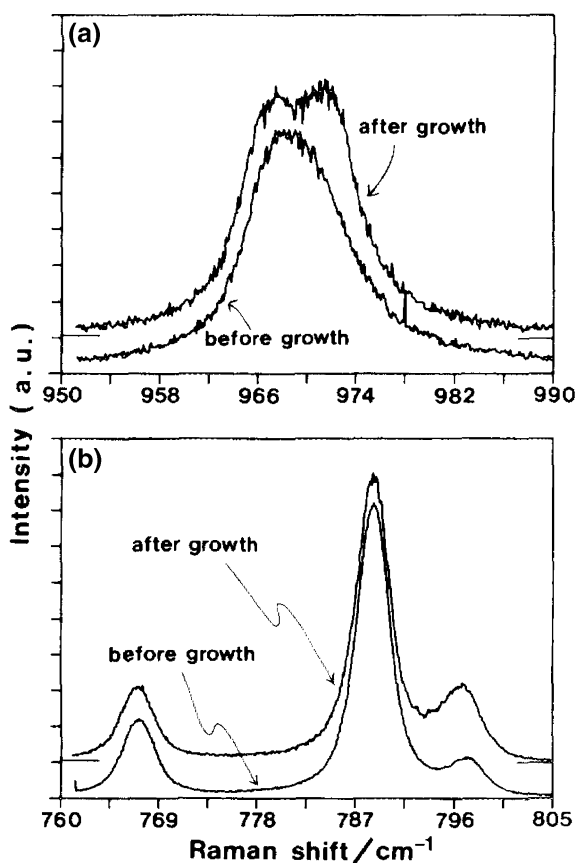


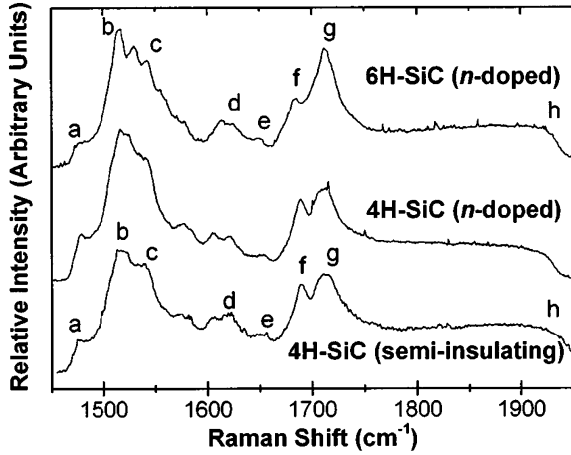
Fig. 2.64 **a** LO and **b** TO regions of the Raman spectra of 6H-SiC before and after growth of the epitaxial layer of cubic SiC on the (0001) surface. The intensities are normalized using the 6H-SiC main peaks at 789 cm^{-1} in the TO region and 967 cm^{-1} in the LO region. Reprinted with permission from [133]. Copyright 1987, AIP Publishing LLC



force constant parameters of a linear-chain model are such determined that the calculated phonon dispersion and Raman intensity profiles fit the experimental results. The employed lattice dynamics model takes into account the third-neighbor plane forces and the differences between the force in the hexagonal and cubic configurations. Quantitative agreement between the calculated and observed Raman profiles is obtained for the folded modes of the TO and TA branches for a number of polytypes. This agreement indicates that the set of force constants can be commonly used for any polytype of SiC and the bond polarizability concept is applicable to folded modes of both acoustic and optical branches.

The first- and second-order Raman spectra of semi-insulating 4H-SiC have been investigated at room temperature by nonresonant excitation [135]. The results are compared to Raman spectra obtained from *n*-type-doped 4H- and 6H-SiC. The second-order Raman spectra (Fig. 2.65) of *n*-type-doped and semi-insulating 4H-SiC are quite similar. The optical branches of the second-order Raman spectra are different between 4H- and 6H-SiC and more complicated than the two-phonon Raman spectra of 3C-SiC. The two-phonon spectra are assigned by comparison

Fig. 2.65 Second-order Raman spectra acquired from semi-insulating 4H-SiC and *n*-type (nitrogen concentration: $2.1 \times 10^{18} \text{ cm}^{-3}$) 4H- and 6H-SiC. Reprinted with permission from [135]. Copyright 1999, American Physical Society



with calculation, and both overtones and combination bands are present in the second-order Raman spectra of 4H- and 6H-SiC.

The lattice compression and pressure can affect the lattice dynamical properties of silicon carbide and also the Raman spectra. The pressure dependences of the optical phonons and transverse effective charge in 3C-SiC have been experimentally investigated [136]. The first-order Raman spectra of 3C-SiC are acquired at different hydrostatic pressure up to 22.5 GPa (Fig. 2.66). The measured LO(Γ , at the Brillouin-zone center) and TO(Γ) phonon energies can be described within experimental errors by the following least-square fits:

$$\begin{aligned}\omega_{\text{TO}} &= (796.5 \pm 0.3) + (3734 \pm 30) \left[-\frac{\Delta a}{a_0} \right], \\ \omega_{\text{LO}} &= (973 \pm 0.3) + (4532 \pm 30) \left[-\frac{\Delta a}{a_0} \right],\end{aligned}\quad (2.1)$$

where ω_{TO} and ω_{LO} are in cm^{-1} and a_0 is the lattice constant at room temperature. The fitted curve is shown in Fig. 2.66. The quadratic fit to the measured phonon energies versus pressure (Fig. 2.66) gives rise a sublinear relationship:

$$\begin{aligned}\omega_{\text{TO}} &= (796.2 \pm 0.3) + (3.88 \pm 0.08)p - (2.2 \pm 0.4) \times 10^{-2}p^2, \\ \omega_{\text{LO}} &= (972.7 \pm 0.3) + (4.75 \pm 0.09)p - (2.5 \pm 0.4) \times 10^{-2}p^2,\end{aligned}\quad (2.2)$$

with ω_{TO} and ω_{LO} given in cm^{-1} and p in GPa. The mode-Grüneisen parameters $\gamma_i = -\partial \ln \omega_i / \partial \ln V$ for the TO(Γ) and LO(Γ) phonons are evaluated from the coefficient of the linear term in $\Delta a/a_0$ of Eq. (2.1). They are $\gamma_{\text{LO}} = 1.55 \pm 0.01$ and $\gamma_{\text{TO}} = 1.56 \pm 0.01$. The LO(Γ)–TO(Γ) splitting increases linearly with lattice compression (Fig. 2.67) and also shows a sublinear dependence on pressure. The corresponding mode-Grüneisen parameter is $\gamma_{\text{LO-TO}} = 1.52 \pm 0.05$. This

Fig. 2.66 Plot of the measured LO(Γ) and TO(Γ) phonon energies versus relative lattice compression (linear lower scale) and pressure (upper scale) in 3C-SiC crystals. The *solid lines* are least-square fits of the experimental points. Reprinted with permission from [136]. Copyright 1982, American Physical Society

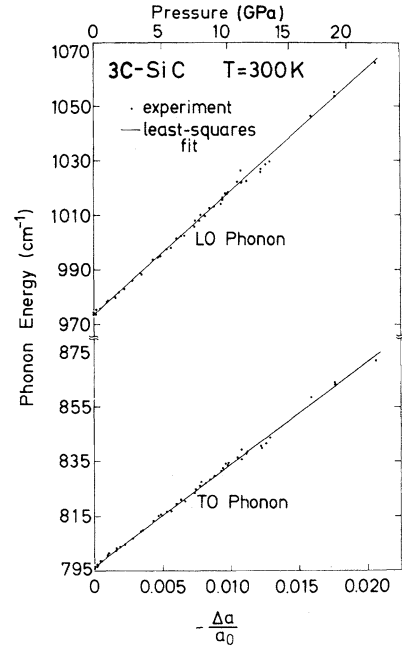
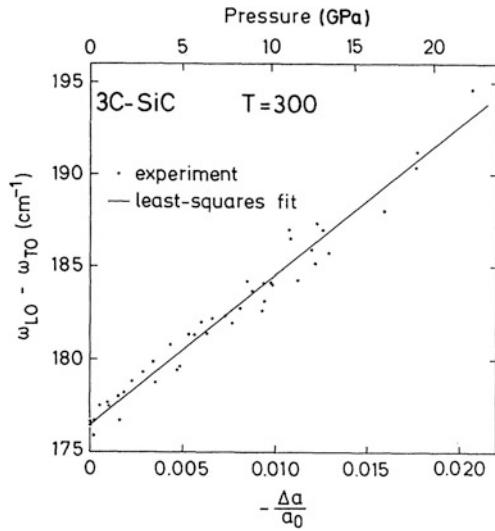


Fig. 2.67 Plot of the LO(Γ)–TO(Γ) splitting versus lattice compression and pressure in 3C-SiC crystals. The *solid lines* through the experimental points is the least-square fit. Reprinted with permission from [136]. Copyright 1982, American Physical Society



increasing splitting implies an increase in the transverse effective charge under pressure. The transverse effective charge is defined as the macroscopic dipole moment per unit displacement of the sublattice (Si or C) when the macroscopic electric field in the crystal is kept zero. The relationship between the transverse effective charge and lattice compression is explained by the microscopic

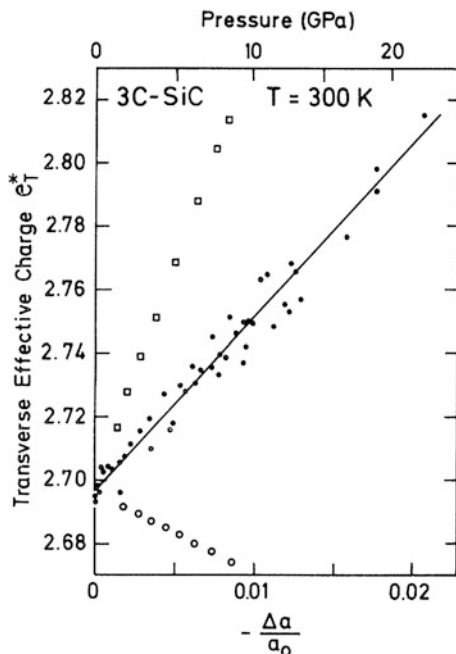
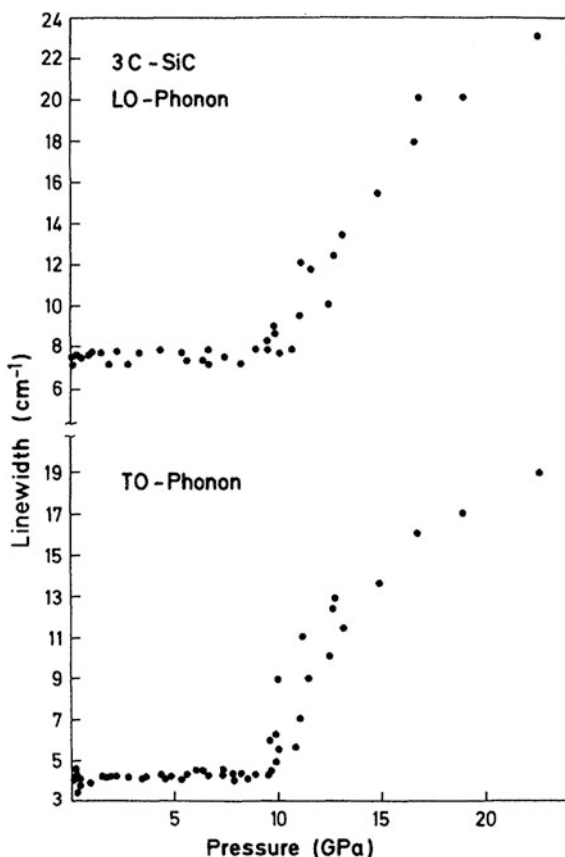


Fig. 2.68 Plot of transverse effective charge versus lattice compression and pressure in 3C-SiC crystals. The data are acquired from the measured pressure dependence of the LO and TO phonons in Figs. 2.66 and 2.67. The solid line is the least-square fit. The squares represent the full pseudopotential calculation result and the open circles are the calculated results based on the bond-orbital model. The calculated transverse effective charges for $\Delta a = 0$ are renormalized to the experimental values in both cases. Reprinted with permission from [136]. Copyright 1982, American Physical Society

pseudopotential calculation but cannot be explained by the semi-empirical models such as the bond orbital model (Fig. 2.68). The line width of the long-wavelength optical phonons of 3C-SiC increases with pressure at above 10 GPa (Fig. 2.69) [137]. This is supposed to arise from the increase in the decay rate as Γ optical phonons decay into two acoustical phonons. Different results are obtained from the low-temperature (6 K) experimental and theoretical study of the pressure dependence of the line widths of the TO and LO phonons in 3C-SiC [138]. While the line width of the TO mode remains unchanged at pressure up to 35 GPa, that of the LO mode exhibits a monotonic increase up to 26 GPa, followed by an abrupt decrease above this pressure. The experimental results agree well with first-principle calculation, and this anomalous behavior is proposed to originate from the anharmonic effect.

The pressure effect in the Raman spectra of 6H-SiC shows features different from 3C-SiC. The TO and LO modes of 6H-SiC are observed at pressure of up to 95 GPa, indicating the structural stability of the 6H polytype [139]. The sample remains optically transparent at 95 GPa, and there is no sign of the expected metallic phase. The LO(Γ) and TO(Γ) Raman frequencies increase with pressure.

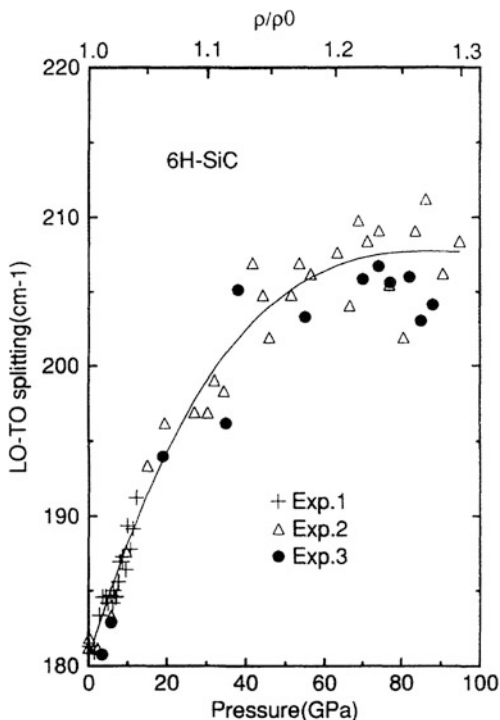
Fig. 2.69 Plot of LO(Γ) and TO(Γ) Raman line widths versus pressure in 3C-SiC crystals. Reprinted with permission from [137]. Copyright 1982, American Physical Society



The LO–TO splitting is 181 cm^{-1} at ambient pressure and increases rapidly below 60 GPa, whereas it tends to saturate at 205 cm^{-1} over 60 GPa (Fig. 2.70). The transverse effective charge increases with pressure at low pressure until reaching a maximum at about 40 GPa and then decreases (Fig. 2.71). This suggests increased covalent binding at high pressure, and this variation agrees with the proposed theory. The mode-Grüneisen parameters γ of the SiC LO and TO modes are derived from experimental data. Comparison of the density variation of γ with diamond and Si leads to the conclusion that γ of the LO mode in 6H-SiC is softer than that of the TO mode, and they both exhibit anomalous decrease.

The temperature effect on the lattice dynamical properties has been investigated. The temperature dependence of the long-wavelength optical phonons of 3C-SiC up to 750 K shows that the TO and LO phonon Raman lines shift to lower frequencies and broaden with temperature (Fig. 2.72) [140]. The shift in the LO line is stronger than that of the TO line, while the LO–TO splitting decreases with temperature. The line width also increases with temperature, and this is explained by assuming that the lifetime of the optical phonon is determined by its decay into

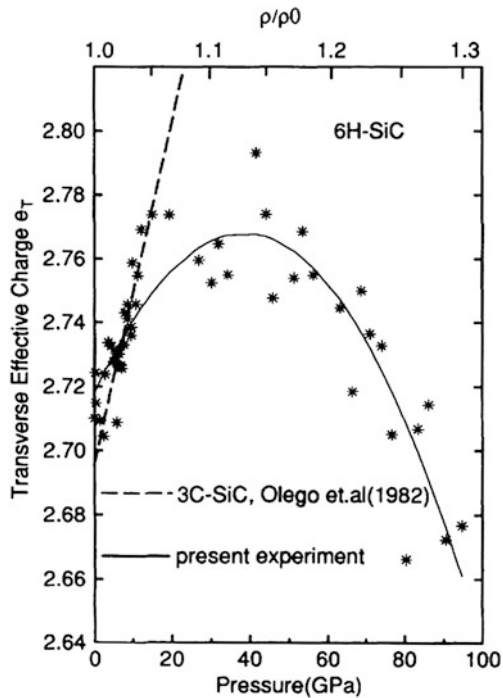
Fig. 2.70 LO–TO splitting in 6H-SiC as a function of pressure obtained by three different experiments. The upper scale is the density variation from the equation of state of 6H-SiC and the *solid curve* represents the quadratic fit of the data. Reprinted with permission from [139]. Copyright 1994, American Physical Society



two LA phonons, similar to the cases of Si and Ge. The transverse effective charge decreases slightly with temperature. The temperature and pressure data elucidate the explicit temperature contribution to the temperature dependence of the transverse effective charge. The results also agree with calculation based on the pseudopotential expression for charges. The temperature dependence of the Raman spectra of 3C-SiC microcrystalline films consisting of randomly oriented crystallites of about 100 nm is quite different from that of 3C-SiC single crystals [141]. The Raman spectra are acquired at elevated temperature up to 1,700 K, and the temperature dependence of the TO and LO phonon frequencies is consistent with that of 3C-SiC single crystals, but the Raman lines are much broader. This can be attributed to the effects of stacking faults by comparing the experimental results with simulated Raman intensity profiles of 3C-SiC comprising randomly distributed stacking faults. The simulated line width and disorder-induced peak shift show good agreement with experiments provided that the average stacking fault distance is assumed to be 6 Å. The Raman lines show irreversible narrowing at temperature above 1,900 K possibly arising from annealing of the stacking faults in 3C-SiC.

The phonon–plasmon coupled mode in SiC and Raman scattering from these coupled modes have been investigated. The plasmon arises when a polar semiconductor is highly doped and plasmon oscillation refers to long-wavelength

Fig. 2.71 Transverse effective charge as a function of pressure. Reprinted with permission from [139]. Copyright 1994, American Physical Society



electron density oscillation. It is a longitudinal vibrational mode of the electron gas, and the energy quantum is called plasmon. The plasmon oscillation can couple to the electric field of the long-wavelength LO phonon to give rise to the phonon–plasmon coupled mode. The Raman data acquired from nitrogen-doped 6H- and 15R-SiC reveal the valley–orbit transitions for donors on nonequivalent sites in the two types of SiC [142]. The transitions can be grouped into two widely separated energy regions, suggesting that the donor wave functions are sensitive to the impurity potential beyond the central cell. The Raman symmetry of the valley–orbit transitions is found to be E_2 that provides some understanding of the position of the conduction-band minima in the Brillouin zone. The Raman spectrum shows a shifted asymmetric LO phonon line (Fig. 2.73) interpreted as the LO phonon–plasmon coupled mode (L^+). This suggests a metallic system, and the calculated mobility is in agreement with measured values in heavily doped samples. The asymmetry of the mode and absence of the L^- LO phonon–plasmon coupled mode may be caused by the short electron collision lifetime. The efficiency of light scattering from an LO phonon coupled to a single component plasmon in a semiconductor is derived by the semi-classical theory [143]. Two terms contribute to the efficiency. The first one arises from the modulation of polarizability by atomic displacements and the macroscopic longitudinal field obeying the ordinary Raman polarization selection rules. The second term comes from free-electron charge density fluctuation that obeys different selection rules and is proportional to

Fig. 2.72 First-order Raman lines of 3C-SiC recorded at two temperatures. Reprinted with permission from [140]. Copyright 1982, American Physical Society

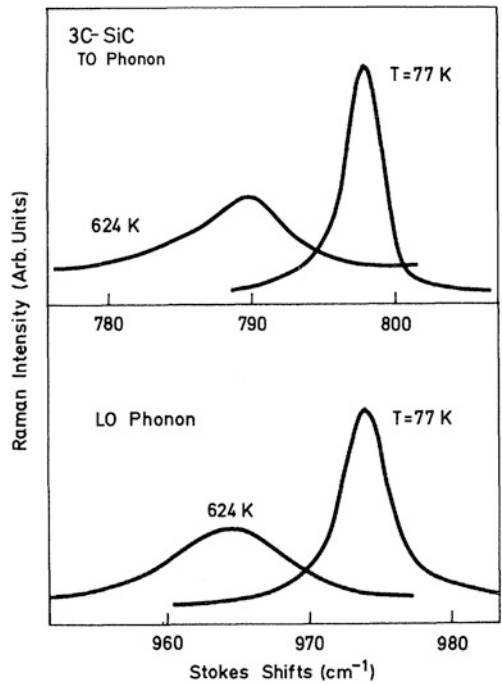


Fig. 2.73 **a** Photon-counting spectrum of the shifted A₁(LO) phonon of nitrogen-doped 6H-SiC measured at 8.8 K. **b** Shifted A₁(LO) phonon with the baseline of part (a) (dashed line) subtracted and theoretical fit (solid line). Reprinted with permission from [142]. Copyright 1972, American Physical Society

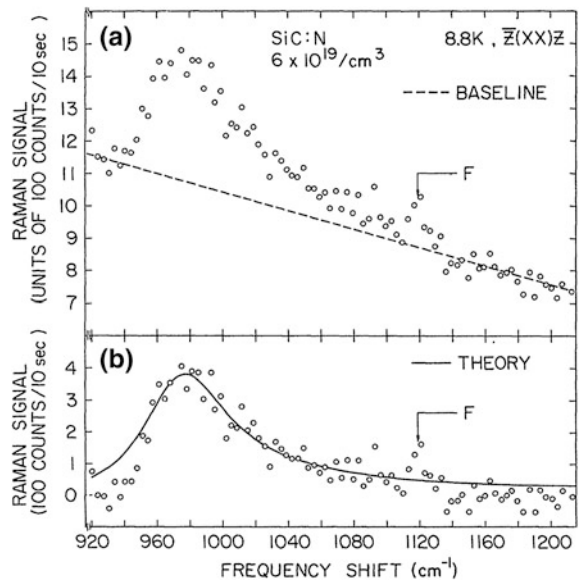
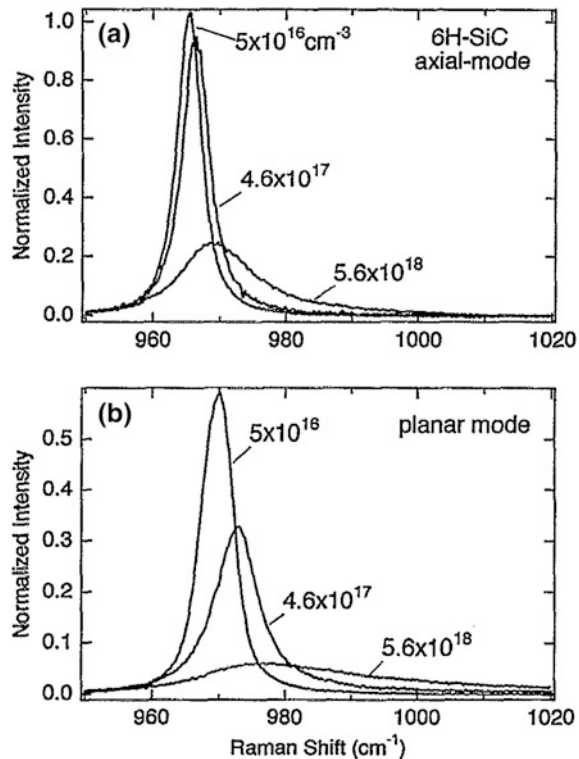


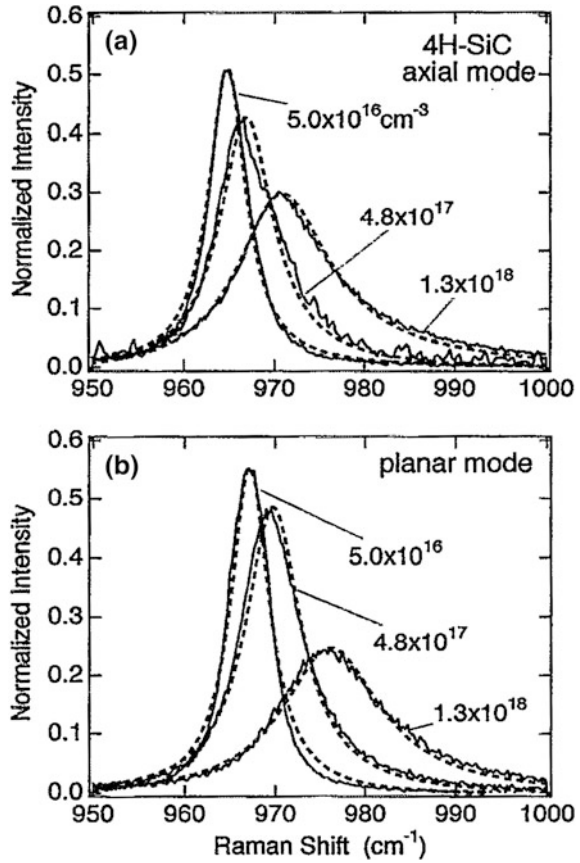
Fig. 2.74 Raman profiles of **a** axial and **b** planar LO phonon–plasmon coupled modes of *n*-type 6H-SiC with different carrier concentrations. Reprinted with permission from [144]. Copyright 1995, AIP Publishing LLC



the square of the wave vector transferred. This theory combined with experimental data provides insight to coupled plasmon–phonon scattering in heavily nitrogen-doped 6H-SiC. The dominant light scattering mechanism is polarizability modulation, whereas the density mechanism is predicted to be 3,500 times weaker. The absolute efficiency of the coupled mode spectrum in doped materials and $A_1(\text{LO})$ phonon in lightly doped crystals has also been derived.

The Raman profiles of the axial and planar LO phonon–plasmon coupled modes in *n*-type 6H- and 4H-SiC bulk crystals with free-carrier concentrations of 10^{16} – 10^{18} cm^{-3} have been studied [144]. In the axial mode, the direction of plasmon oscillation and atomic displacement are parallel to the *c*-axis, whereas in the planar mode, they are perpendicular to the *c*-axis. In 6H-SiC, the planar mode exhibits more dramatic variations in the peak intensity, width, as well as shift with carrier concentrations than the axial mode (Fig. 2.74). In contrast, the spectra of 4H-SiC show no noticeable difference in the peak intensity and width between the axial and planar modes, but the planar mode shows a slightly bigger peak shift than the axial mode (Fig. 2.75). The anisotropic plasmon frequencies and carrier damping constants are derived using a fit of the calculated band shape with the experimental Raman band profiles, and the agreement between the experimental and calculated

Fig. 2.75 Comparison between measured (solid line) and calculated (dotted line) Raman spectra of **a** axial and **b** planar LO phonon–plasmon coupled modes in *n*-type 4H-SiC with different concentrations. Reprinted with permission from [144]. Copyright 1995, AIP Publishing LLC



profiles is rather good. Using the plasmon frequencies in combination with the carrier concentrations obtained from Hall measurements, the longitudinal (m_{\parallel}) and transverse (m_{\perp}) effective masses of electrons can be derived, namely $m_{\parallel} = 1.4m_0$ and $m_{\perp} = 0.35m_0$ for 6H-SiC and $m_{\parallel} = 0.48m_0$ and $m_{\perp} = 0.30m_0$ for 4H-SiC. The carrier mobility obtained from the Raman analysis is also anisotropic.

The relationship between the LO phonon–plasmon coupled mode position and carrier concentration can be used to map the carrier concentration spatially. This is demonstrated by the semi-insulating and *n*-type-nitrogen-doped (concentration between 2.1×10^{18} and $1.2 \times 10^{19} \text{ cm}^{-3}$) 4H-SiC and 6H-SiC [145]. Significant coupling between the A_1 longitudinal optical (LO) phonon and plasmon mode is observed, and there is direct correlation between the position of the coupled mode peak and carrier concentration. Figure 2.76a shows the nitrogen concentration estimated from the coupled LO phonon frequency across the wafer. The spatial dependence is not the same in different SiC wafers, and the concentration profile is generally not symmetrical with respect to wafer rotation. The wafer center has a large carrier concentration, and the far edges have doping levels much smaller than

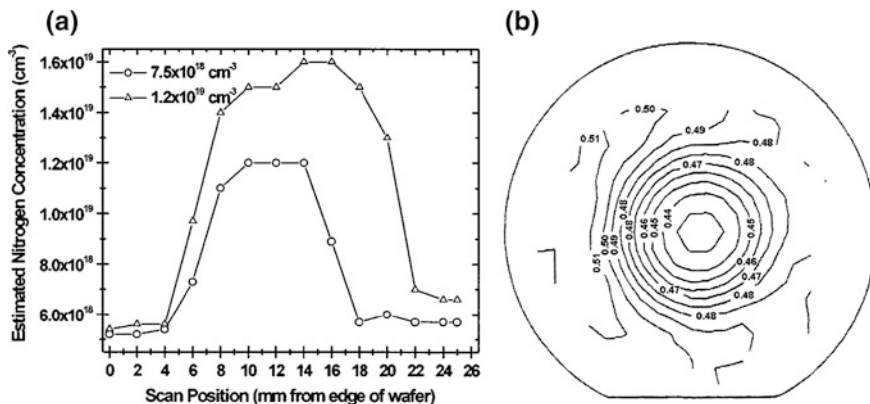


Fig. 2.76 **a** Estimated carrier concentration profile across two heavily doped 4H-SiC wafers determined by Raman spectroscopy with nominal nitrogen concentrations denoted in the legend. **b** Resistivity map for the 4H-SiC wafer nominally doped with $1.2 \times 10^{19} \text{ cm}^{-3}$. Reprinted with permission from [145]. Copyright 1998, AIP Publishing LLC

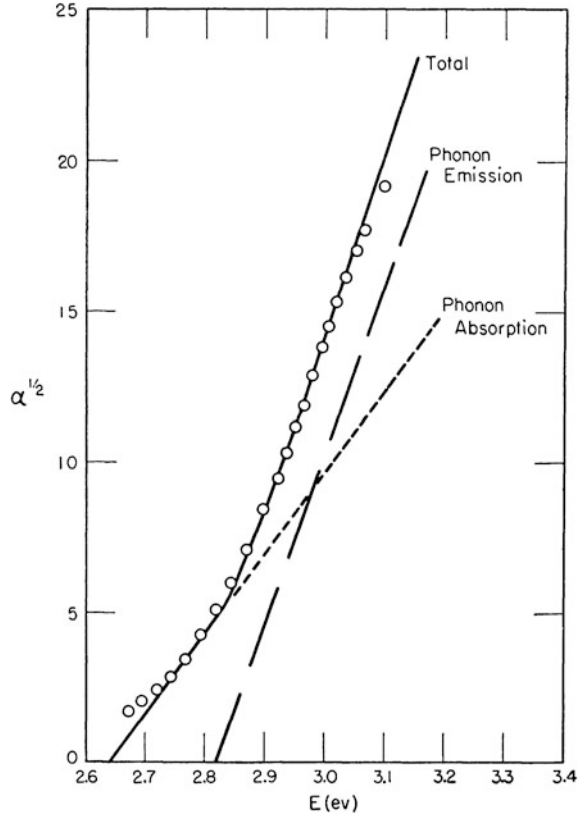
the nominal value specified for the wafer. Figure 2.76b shows the resistivity map of a doped SiC wafer confirming the spatially nonuniform dopant concentration. The resistivity variation in the most heavily doped wafer is consistent with the observed carrier concentration variation obtained by Raman measurement of the same wafer. The results indicate that Raman scattering can be employed as a noncontact, nondestructive, and in situ probe for the spatial distribution of carriers in SiC wafers.

2.6 Absorption and Luminescence Properties

Light absorption and emission are very important optical processes in solids. On the one hand, they can serve as probes of the electronic structures and defect characteristics of solids. On the other hand, luminescence from solids has applications in many areas including displays, lighting, information communication, etc. As a wide bandgap semiconductor, the luminescence properties of silicon carbide have technological and commercial interests.

As a direct probe method for energy band structures, light absorption by some common polytypes of silicon carbide has been extensively investigated. Choyke and Patrick have acquired UV-Vis absorption spectra from hexagonal SiC at temperature from 77 to 717 K [146]. Figure 2.77 shows the absorption spectrum [$\alpha^{1/2}$ versus E (photon energy)] at 700 K along with the fit. The fit is the sum of the following two terms representing phonon absorption and phonon emission, respectively:

Fig. 2.77 Comparison between observed and calculated absorption by hexagonal silicon carbide at 700 K. Reprinted with permission from [146]. Copyright 1957, American Physical Society

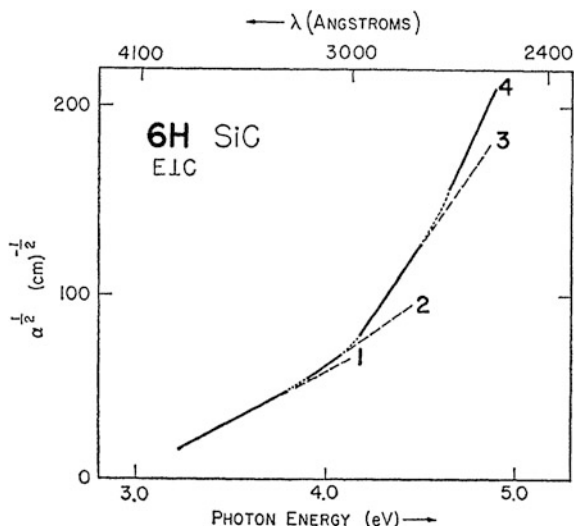


$$\alpha^{\frac{1}{2}}(\text{abs.}) = \left[\frac{A}{e^{\theta/T} - 1} \right]^{\frac{1}{2}} [h\nu - (E_g - k\theta)], \quad (2.3)$$

$$\alpha^{\frac{1}{2}}(\text{emiss.}) = \left[\frac{A}{1 - e^{-\theta/T}} \right]^{\frac{1}{2}} [h\nu - (E_g + k\theta)], \quad (2.4)$$

where α is the absorption constant corresponding to absorption or emission of a phonon, h is Planck's constant, ν is the photon frequency, E_g is the energy gap of silicon carbide, k is Boltzmann's constant, and A is a constant depending on the properties of the materials and electron-phonon interaction. To obtain the best fit based on Eqs. (2.3) and (2.4), $k\theta$ (phonon energy) = 0.09 eV and $A = 2,500$. The good fit indicates that the interband transitions in SiC are indirect. The minimum energy gap at 300 K is 2.86 eV and above this temperature, $dE_g/dT = -3.3 \times 10^{-4}$ eV/degree. Four higher-energy absorption edges are observed by studying absorption of 1.8- μm -thick 6H-SiC prepared by grinding and polishing [147]. Three indirect absorption edges (Fig. 2.78) are observed at 3.0, 3.7, and

Fig. 2.78 Plot of $\alpha^{1/2}$ versus $h\nu$ for the UV-Vis absorption spectrum of 6H-SiC with data obtained from many samples. The measured values are on the straight-line segments (*solid*) or in the transitional regions (*dotted*). The four straight-line segments are extrapolations (*dashed*). Reprinted with permission from [147]. Copyright 1968, American Physical Society



4.1 eV (from fitted lines 1, 2, and 3), whereas the fourth absorption edge is at 4.6 eV (from line 4) but cannot be definitively identified as direct or indirect. The following simplified equation is used to fit the experimental data:

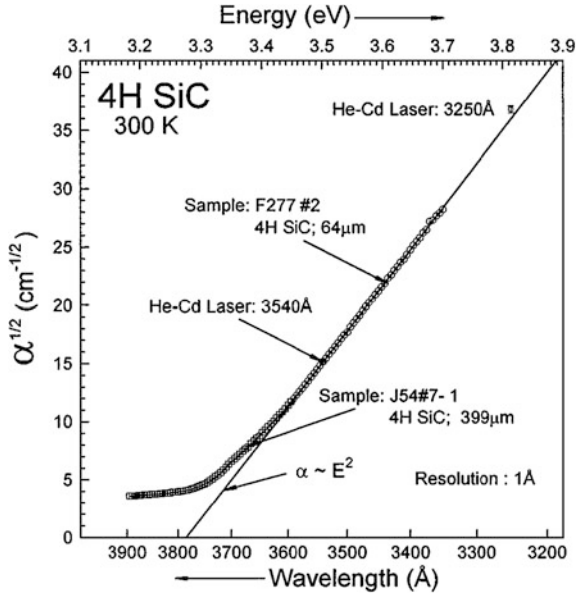
$$\alpha = \sum_i \alpha_i = \sum_i A_i (h\nu - E_{gi})^2, \quad (2.5)$$

where α is the absorption constant in cm^{-1} , A_i is a constant, and E_{gi} is the energy threshold. A_i and E_{gi} are chosen to yield the best fit, and in this equation, the effects of excitons and phonons are neglected since they are not observed experimentally.

The absorption coefficients of 4H-SiC in the wavelength range between 325 and 390 nm have been determined at room temperature [148]. The absorption coefficient from 335 to 390 nm is measured using a Xe arc lamp as the light source and the light propagates along the c -axis, whereas the 325-nm absorption coefficient is determined using a He-Cd laser source. The results are displayed in Fig. 2.79. At high energy, the square root of the absorption coefficient is proportional to the wavelength, as required by the indirect bandgap nature. By using the known relationship between the bandgap and temperature, the absorption coefficients of 4H-SiC at 2 K can be derived. The absorption coefficients of 4H-, 6H- and 3C-SiC between 297 and 390 nm are measured at room temperature using xenon and tungsten lamps together with lasers of several wavelengths [149]. On the basis of the temperature dependence of the bandgaps, the absorption coefficients at 2 K are estimated.

Donor-acceptor pair luminescence plays an important role in silicon carbide. Photoluminescence from the donor-acceptor pairs in cubic SiC excited by a laser at 1.8 K has been studied in detail [150]. The spectrum consists of a series of lines, and some of them are displayed in Fig. 2.80. The lines arise from the nitrogen

Fig. 2.79 Square root of the absorption coefficient versus wavelength of 4H-SiC. Reprinted with permission from [148]. Copyright 1998, AIP Publishing LLC



(N)-aluminum (Al) pairs (donor N in C sites and acceptor Al in Si sites) based on the crystal growth and freedom from extraneous lines. The following relationship is employed to analyze the origin of the observed luminescence lines [151]:

$$h\nu = E_g - (E_D + E_A) - E_C + E_{vdW}, \quad (2.6)$$

where E_g is the bandgap, E_D and E_A are the donor and acceptor ionization energies, E_C is the Coulombic interaction energy between the donor and acceptor ions after electron-hole recombination, and E_{vdW} is the interaction energy between the neutral donor and acceptor atoms before recombination. E_C has discrete values allowed by the lattice structure and so for a given donor, E_g is evaluated for each shell (denoted by an integer m) of equidistant acceptors. The same table of donor-acceptor shell substructure components of GaP is used to determine the shell numbers in cubic SiC, considering the identical (zinc-blende) crystal structures. In the N-Al spectrum of cubic SiC, the lines are well resolved up to the 80th shell and extrapolation yields the photon energy for distant donor-acceptor pairs, $h\nu_\infty$, of 2.0934 eV. With the aid of the bandgap of the cubic SiC (2.39 eV), the donor and acceptor ionization energies can be derived, $E_D = 118$ meV for N, and $E_A = (179 \text{ meV}) + E_x$, for Al. Here, E_x represents the exciton binding energy. The donor-acceptor spectrum exhibits as an envelope at low resolution (Fig. 2.81), and the low-resolution spectrum shows several phonon replicas from which the phonon energies are derived to be 69, 94, and 118 meV.

Donor- and acceptor-related luminescence from 4H-, 6H-, and 3C-SiC single crystals has been investigated in the temperature range between 2 and 450 K [152].

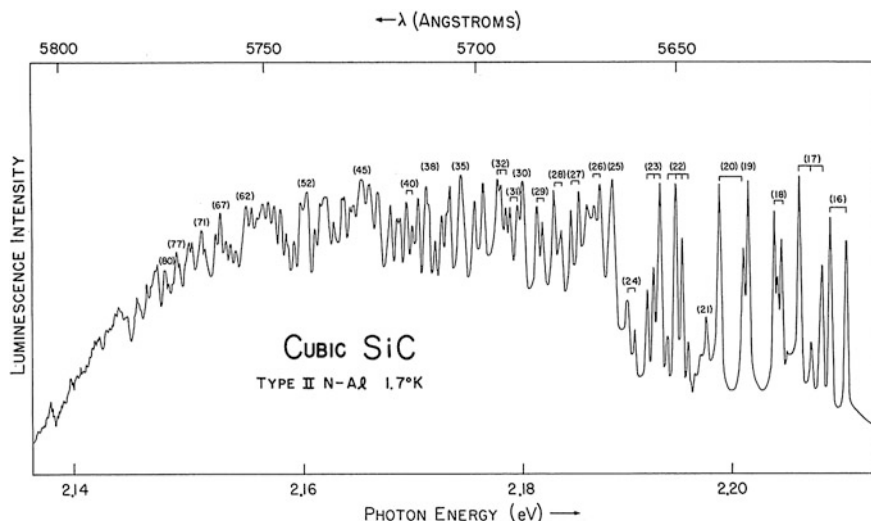


Fig. 2.80 Photoluminescence lines for shell numbers bigger than 15. The shell numbers (m) are displayed in brackets and shell substructure components are identified for small m . Reprinted with permission from [150]. Copyright 1970, American Physical Society

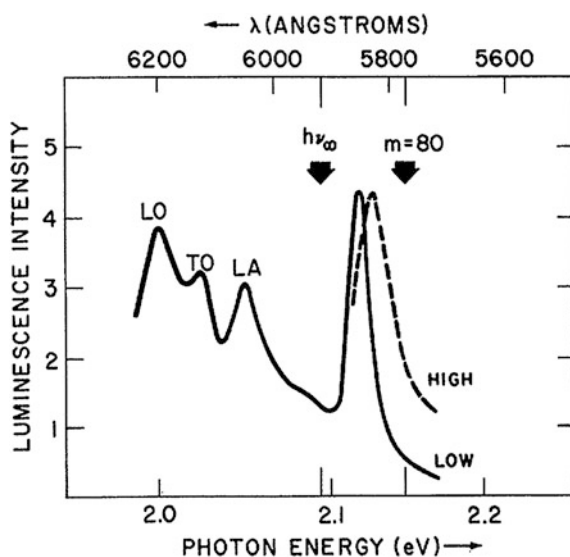


Fig. 2.81 Low-resolution envelope of the donor-acceptor PL spectrum (*strongest peak*) and phonon replicas (LA, TO, and LO). The solid and dashed lines are obtained at small and large excitation intensities, respectively. The position of the $m = 80$ line shown in Fig. 2.80 is marked and the photon energy of the distant pair, $h\nu_\infty = 2.0934$ eV, is also marked. Reprinted with permission from [150]. Copyright 1970, American Physical Society

Table 2.3 Ionization energies of donors and acceptors in cubic-like sites (E^C) and hexagonal-like sites (E^H), their average ratios, and free-exciton binding energies (E_x) in 3C, 4H, 6H, and 15R SiC. Reprinted with permission from [153]. Copyright 1980, American Physical Society

Ionization energy (meV)						
	Site	N	Al	Ga	B	E_x
3C	C	56.5	254	343	735	13.5
6H	C	155	249	333	723	78
	H	100	239	317	698	
	E^C/E^H	1.55	1.040	1.050	1.036	
15R	C	112	236	320	700	40
			230	311		
			223	305		
	H	64	221	300	666	
			206	282		
	E^C/E^H	1.75	1.076	1.072		
4H	C	124				20
			191	267	647	
	H	66				
	E^C/E^H	1.88	1.0	1.0	1.0	

acceptor pair transitions, and A is attributed to free-to-acceptor transition. The peak intensity ratios of C_0 to B_0 under high-intensity excitation, where both the B and C series appearing with full intensity are, respectively, 0.96 for 4H, 1.9 for 6H, and 1.4 for 15 R SiC. These values agree well with the ratios of the number of cubic-to-hexagonal-like sites (1 for 4H, 2 for 6H, and 1.5 for 15R). Hence, the B and C series of emission lines arise from donor–acceptor pair transitions between acceptors and donors in hexagonal-like and cubic-like sites, respectively, as suggested previously [154]. This implies that every impurity atom enters each type of site with the same equal probability. Further analysis based on the configuration coordinate phonon spectra supports the notion that all the impurities in cubic sites occupy deeper levels than those in hexagonal sites (Table 2.3). The ratios of the ionization energies between the cubic and hexagonal sites, which are roughly constant and independent of the polytypes and impurity types, are 1.0–1.08 for acceptors and 1.55–1.88 for donors. The origin of the site effect on the impurity level is explained by assuming a local dielectric constant and local effective mass based on the quantum defect model. The exciton binding energy depends almost linearly on the ionization energy of nitrogen donors in 3C, 4H, 6H, and 15R SiC.

The donor–acceptor pair light emission from silicon carbide can persist at elevated temperature. The highly efficient visible luminescence from N- and B-doped 6H-SiC epilayers is observed at room temperature [155]. Figure 2.83 displays the PL spectra of two samples with B concentrations of $2 \times 10^{17} \text{ cm}^{-3}$

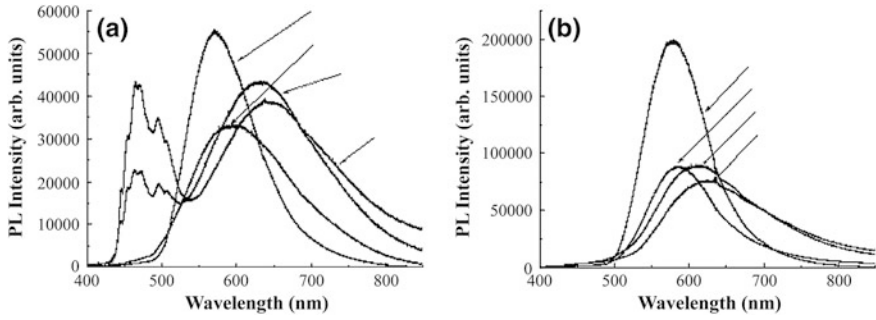
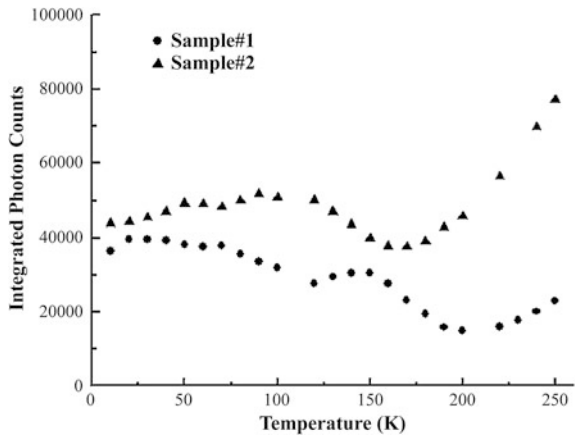


Fig. 2.83 Photoluminescence spectra of N- and B-doped 6H-SiC epilayers excited by 351 nm at different temperatures. The B concentrations are **a** $2 \times 10^{17} \text{ cm}^{-3}$ (sample 1) and **b** $2 \times 10^{18} \text{ cm}^{-3}$ (sample 2), respectively. Reprinted with permission from [155]. Copyright 2006, AIP Publishing LLC

Fig. 2.84 Integrated photon count in the PL spectrum as a function of temperature for low and highly doped 6H-SiC. Reprinted with permission from [155]. Copyright 2006, AIP Publishing LLC



(sample 1) and (b) $2 \times 10^{18} \text{ cm}^{-3}$ (sample 2). The N concentration is approximately $4 \times 10^{18} \text{ cm}^{-3}$ in both samples. The temperature varies from 10 to 250 K in the PL measurements. The sample with a small B concentration shows both N–B donor–acceptor emission at approximately 630 nm and N–Al (unintentionally introduced) donor–acceptor emission at 460 nm at temperature below 100 K. However, the N–Al emission is quenched above 100 K. The peak wavelength of the N–B emission gradually shifts to 576 nm with increasing temperature. The N–B emission band is broad with a full width at half maximum (FWHM) of 110 nm at 250 K. The sample with a large B concentration shows only the N–B emission even at low temperature. The PL intensity from the highly doped sample at high temperature is significantly larger (Fig. 2.84). A high internal quantum efficiency of 95 % is estimated for the highly B-doped sample at 250 K. The donor–acceptor recombination lifetimes are 2.5 and 5.0 ms for samples 1 and 2, respectively, as determined from the time-resolved photoluminescence measurement, and in good

agreement with the calculated value based on the rate equation. It has also been demonstrated that when the N and B concentrations are in a range of 10^{18} cm^{-3} , 6H-SiC shows the most intense luminescence when the concentration difference between the donors and acceptors is about $4.6 \times 10^{18} \text{ cm}^{-3}$ [156]. The PL spectrum has a maximum at about 587 nm with an FWHM of 120 nm. However, the obtained lifetimes are 0.5, 30 ns, 0.5, 1.2, and 1.1 μs for different samples and much smaller than those reported in Ref. [155].

Some specific luminescence lines observed from bulk silicon carbide are ascribed to recombination of excitons bound to impurities or free-to-bound recombination. The exciton–impurity complex is discussed in Ref. [157], and various donors and acceptors in Si have been investigated leading to the observation of luminescence arising from the decay of the exciton bound to impurities [158]. The phonon-assisted indirect transitions involving the exciton–impurity complexes in SiC generally give rise to a series of emission lines, from which the energies of the phonons involved can be derived. Choyke and Patrick have reported photoluminescence from 6H-SiC, showing 50 lines at low temperature [159]. Figure 2.85 depicts the PL spectrum collected at 6 K. It shows three no-phonon lines, P_0 , R_0 , and S_0 caused by exciton recombination at the three non-equivalent unionized nitrogen donors along with the phonon replicas. For example, P_0 is related to a series of lines. The P series are due to recombination at the P nitrogen center with emission of one of 17 phonons. The displacement of a P line from P_0 corresponds to the energy of a phonon. The 17 measured phonon

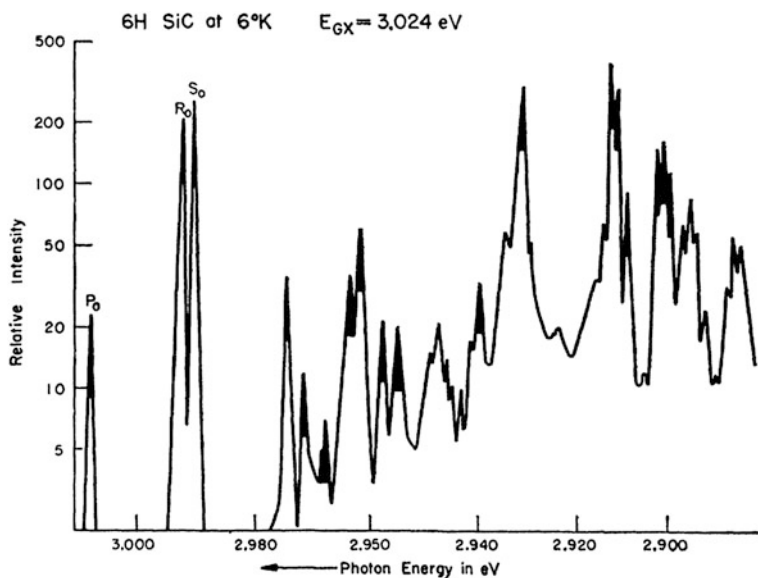


Fig. 2.85 Photoluminescence spectrum obtained from 6H-SiC at 6 K. The black peaks belong to the P series. Reprinted with permission from [159]. Copyright 1962, American Physical Society

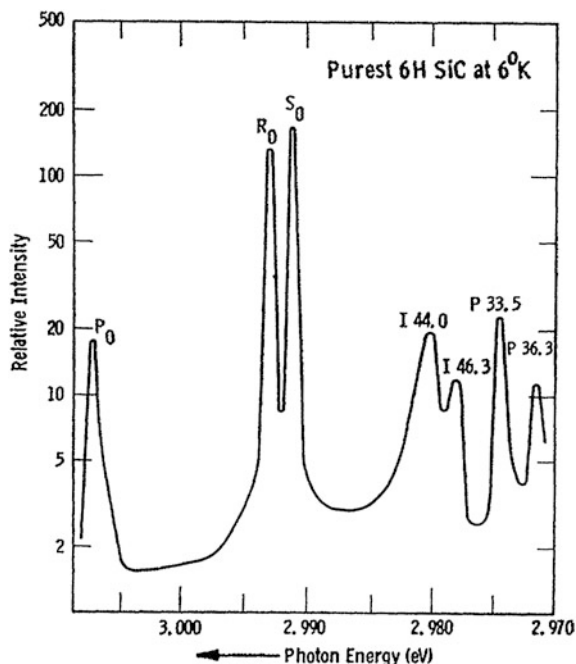


Fig. 2.86 Photoluminescence spectrum of the purest 6H-SiC sample at 6 K. Two additional intrinsic lines (*I* 44.0 and *I* 46.3) due to recombination of free excitons are shown and the numbers are the phonon energies in meV. Reprinted with permission from [159]. Copyright 1962, American Physical Society

energies can be assembled into an appropriate extended Brillouin zone. The spin-orbit splitting of the valence bands is found to be only 4.8 meV, suggesting that the hole is confined to the carbon sublattice. Luminescence due to recombination of free excitons involving phonons has also been observed (Fig. 2.86).

Besides the excitons bound to neutral nitrogen impurity atoms, the exciton bound to the singly ionized nitrogen impurity can yield luminescence in 6H-SiC [160]. Photoluminescence from the ionized nitrogen-exciton complexes in N-doped 6H-SiC is observed at 6 K, and the PL spectrum is shown in Fig. 2.87. The ionization energies of the three nonequivalent nitrogen donors are 0.17, 0.20, and 0.23 eV, respectively. The observed quenching of edge emission in the impure samples is ascribed to exciton hopping. Figure 2.88 displays the energy ranges of the two distinct luminescence spectra arising separately from the exciton-neutral nitrogen complex (four-particle complex) or exciton-ionized nitrogen complex (three-particle complex). The three-particle spectrum extends into the lower-energy region with multi-phonon emission and becomes gradually a continuum. Four-particle emissions have higher photon energies than three-particle emissions because the exciton is more tightly bound to ionized nitrogen atoms than neutral ones. In 15R-SiC, the photoluminescence spectra due to the two kinds of nitrogen-

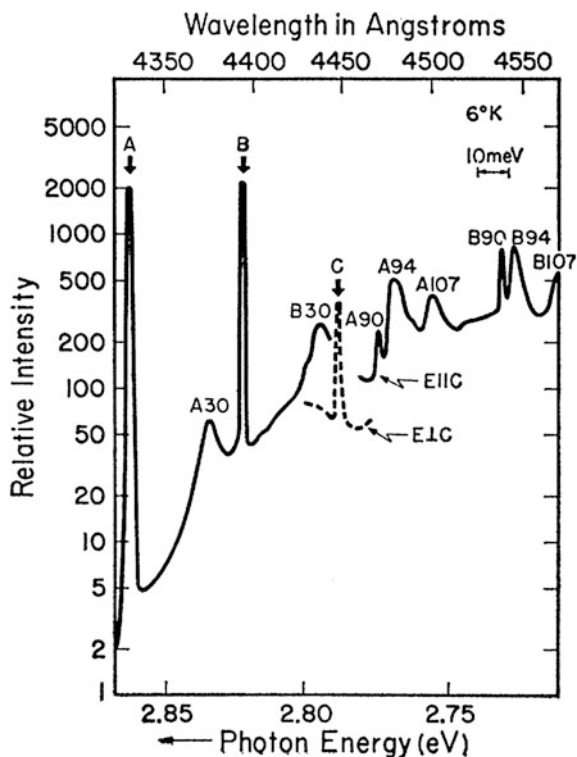


Fig. 2.87 Photoluminescence spectrum of 6H-SiC showing the portion of the ionized nitrogen-exciton complex band, including the no-phonon lines of A, B, and C along with some peaks arising from phonon emission. The peaks are labeled with their series letter and the number indicates the phonon energy in meV. Reprinted with permission from [160]. Copyright 1963, American Physical Society

exciton complexes are very similar to those of 6H-SiC and similar phonon spectra are obtained [161]. The four nitrogen ionization energies are approximately 0.14, 0.16, 0.16, and 0.20 eV, which are smaller than those in 6H-SiC. Only four of the five nonequivalent nitrogen atoms in 15R-SiC are detected from the PL spectra. 15R-SiC also exhibits indirect absorption at the absorption edges. The edges have a similar shape as 6H-SiC due to the similarity in the phonon spectrum. 15R-SiC has an exciton energy gap of 2.986 eV at 6 K, which is smaller than that of 6H-SiC. According to the luminescence from thermally excited states of the exciton-neutral nitrogen complexes, it is proposed that 15R-SiC has a second valence band that splits from the first one by 4.8 meV due to the spin-orbit interaction; the holes are supposed to be largely confined to the carbon sublattice. The result shows evidence of the presence of six conduction-band minima.

Luminescence from the exciton-nitrogen complex and interband absorption in cubic SiC has been investigated [21]. Absorption measurements at 4.2 K demonstrate that 3C-SiC has an indirect absorption edge associated with exciton

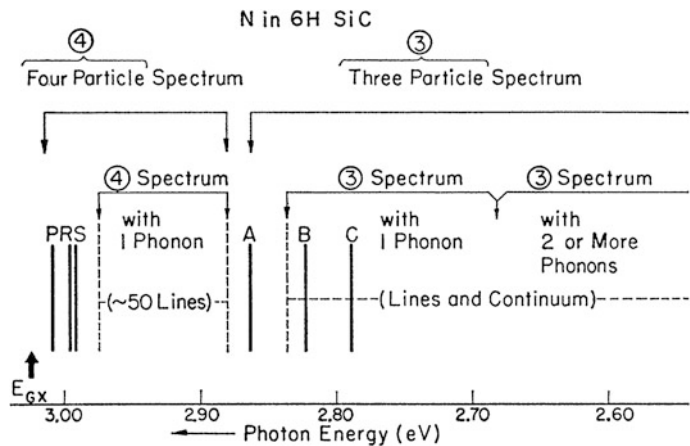


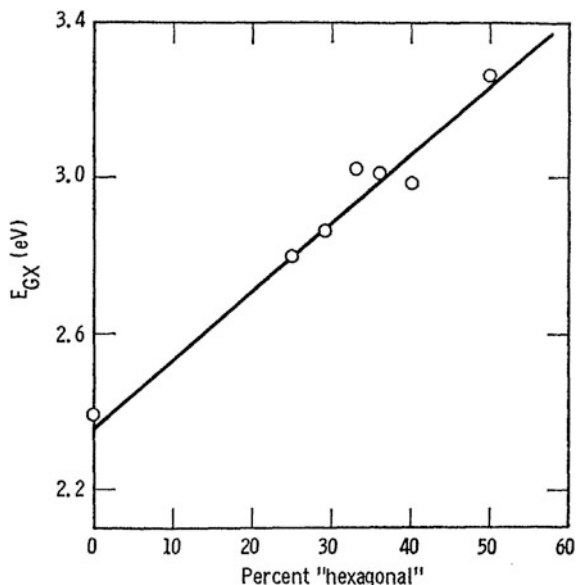
Fig. 2.88 Energies of no-phonon lines *P*, *R*, and *S* of the exciton–neutral nitrogen complex photoluminescence spectrum and *A*, *B*, and *C* of the exciton–ionized nitrogen complex photoluminescence spectrum as well as energy ranges of photons emitted with simultaneous phonon emission. E_{Gx} is the exciton energy gap. Reprinted with permission from [160]. Copyright 1963, American Physical Society

transitions and the exciton energy gap is 2.390 eV. The phonon energies determined from the absorption spectrum are 46, 79, 94, and 103 meV. The exciton–neutral nitrogen complex luminescence spectrum at 6 K provides the accurate phonon energies. The thermally excited states of the complex give rise to additional lines in the luminescence spectrum at higher temperature. Comparison shows that 3C-, 6H-, and 15R-SiC have very close phonon energies, and the values are 46.3 (TA), 79.4 (LA), 94.4 (TO), and 102.8 (LO) meV for 3C-SiC. Choyke and colleagues have found an important empirical correlation between the energy gap and hexagonality (Table 2.4) for seven polytypes of SiC (Fig. 2.89). It is a nearly linear relationship. They have also investigated low-temperature luminescence from the

Table 2.4 E_{Gx} (exciton bandgap) of seven SiC polytypes and corresponding “hexagonal” percentage. Reprinted with permission from [21]. Copyright 1964, American Physical Society

Polytype (Ramsdell notation)	Exciton bandgap E_{Gx}	Jagodzinski notation	Hexagonality <i>h</i> (percent)
3C	2.390	k	0
8H	2.80	hkkk	25
21R	2.86	hkkhkkk	29
15R	2.986	hkhkk	40
33R	3.01	hkkhkkhkkhk	36
6H	3.023	hkk	33
4H	3.263	hk	50

Fig. 2.89 Exciton bandgap E_{GX} versus hexagonal percentage (hexagonality) of seven SiC polytypes. The values of E_{GX} are obtained from absorption measurements at 4.2 K or luminescence measurements at 6 K. These values and the hexagonality values are summarized in Table 2.4. Reprinted with permission from [21]. Copyright 1964, American Physical Society



exciton–nitrogen complexes in 4H-SiC [162]. Eighteen phonon energies are derived from the PL spectra. The interpretation of the phonon spectrum suggests positions of low symmetry for the conduction-band minima, requiring a 12-valley model for electrons. It is argued that such a method can be generalized to other SiC polytypes to locate the conduction-band minima. It explains the observed similarity in the phonon spectra of seven SiC polytypes. The relatively large and pure 2H-SiC crystals are fabricated, and their absorption and luminescence properties at 2–8 K are investigated [163]. 2H-SiC shows an indirect energy gap of 3.330 eV that is the largest among all the observed SiC polytypes. The group theory selection rules are utilized to analyze the polarized luminescence in order to determine the active phonons. The spectrum is consistent with the selection rules by assuming that there are conduction-band minima at the K -points of the Brillouin zone. SiC resembles diamond more than Si concerning the “trace variable” forces.

Nitrogen-bound exciton luminescence can be used to determine the nitrogen-dopant concentration in silicon carbide, as demonstrated by low-temperature photoluminescence spectroscopy conducted on uncompensated 4H- and 6H-SiC [164]. This is realized by comparing the intensity of the nitrogen-bound exciton lines to that of the free exciton (as an internal reference). A line-fitting method with the proper line shape is employed to separate the contribution of the bound exciton and free-exciton lines in the PL spectrum. The ratio of the bound exciton zero-phonon lines to the free-exciton most intensive phonon replica (around 77 meV) shows good linear dependence on the dopant concentration as determined by capacitance-voltage measurements on both polytypes. When the real line shape, influence of the spectrometer transfer function, and structure of the PL

spectrum in the vicinity of the free-exciton replica are taken into account, the fit allows for the determination of the N-dopant concentration in the ranges between 1×10^{14} and $3 \times 10^{16} \text{ cm}^{-3}$ in 4H-SiC and 1×10^{14} and 10^{17} cm^{-3} in 6H-SiC. The free-exciton emission is not observed above these concentrations.

Besides donor–acceptor pair, exciton bound to donor complex, there are other models proposed to explain the low-temperature luminescence lines in silicon carbide. A series of bound exciton lines just below the luminescence of single excitons bound to the shallow nitrogen donors [165] can be attributed to recombination in the multiple bound exciton complexes. This model is supported by the spectral positions, Zeeman effect, and behavior under optical pumping. Two series of near-infrared emission bands are observed from boron-doped 3C-SiC crystals [166]. The dominant series of luminescence bands (at about 1.6 eV) at low temperature is assigned to nitrogen donor–boron acceptor pair recombination. The other series of bands is explained by the free-to-bound transition model concerning the spectral shape of the zero-phonon line and temperature dependence. In this scenario, the electrons in the conduction band recombine with the holes trapped at the boron acceptors to produce luminescence. The ionization energies of the nitrogen donor and boron acceptor are estimated to be 0.05 and 0.73 eV, respectively. The exciton can also be bound to the neutral aluminum acceptor complex in 3C-, 6H-, and 4H-SiC, as confirmed by low-temperature photoluminescence and cathodoluminescence experiments [167]. The correlated lines are observed only from lightly doped *p*-type SiC films, and the intensity increases with aluminum concentration. The multiplicity of the observed lines agrees with the prediction from the symmetry-based models. In another study on low-temperature photoluminescence from the 6H, 4H, and 15R polytypes of SiC [50], a couple of new features different from the well-known emission lines close to the bandgap are observed from the three polytypes and attributed to recombination of the bound excitons at aluminum acceptors. There are two distinct boron-related centers in silicon carbide polytypes, one shallow with ionization energy of 300 meV and the other deep with ionization energy of 650 meV. 4H-SiC homoepitaxial films can be intentionally doped with the shallow boron center by controlling the silicon to carbon source gas ratio during chemical vapor deposition [168]. For samples produced using a small Si/C ratio, the shallow boron centers tend to be incorporated into the silicon sublattice as confirmed by the temperature-dependent Hall effect, admittance spectroscopy, and deep-level transient spectroscopy. A luminescence peak around 383.8 nm is observed from the samples at low temperature, and this peak stems from recombination of an exciton–neutral shallow boron acceptor complex. The first evidence for assignment of this luminescence peak is that its intensity increases with boron concentration, and secondly, the observed momentum-conserving phonon replicas have energies consistent with other previously observed exciton–neutral acceptor complexes in SiC. Lastly, the excited states are observed at elevated temperature and this is similar to the cases of excitons bound to neutral aluminum and gallium acceptors.

Some luminescence lines with previously unknown origins in silicon carbide are ascribed to bound excitons. The D_1 photoluminescence observed from

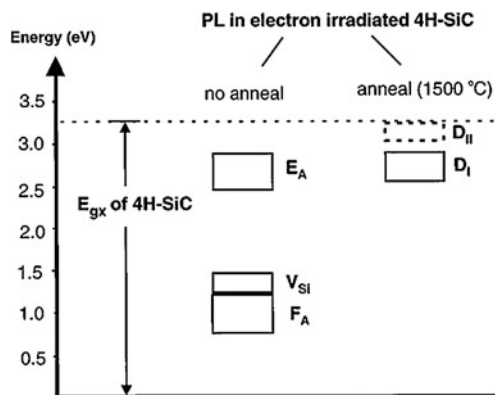


Fig. 2.90 Energy ranges of the main PL spectra of room-temperature electron-irradiated 4H-SiC. The excitonic bandgap energy of 4H-SiC is shown on the left, the case right after electron irradiation in the *middle*, and that after high temperature (about 1,500 °C) annealing on the *right*. Reprinted with permission from [60]. Copyright 1999, American Physical Society

electron-irradiated 4H-SiC has been investigated [169]. At temperature lower than 5 K, the D_1 PL spectrum shows a no-phonon line (L_1 , 427.3 nm) and the phonon replicas. The L_1 line decreases rapidly with increasing temperature and meanwhile, two higher-energy no-phonon lines (M_1 , 426.1 nm; H_1 , 425.7 nm) emerge. At temperature higher than 100 K, the D_1 PL is quenched. The lifetime of the D_1 PL is 450 μ s at 1.3 K and 2 μ s at 70 K. It is suggested that the D_1 luminescence arises from exciton recombination at an isoelectronic center, with one of the particles of the exciton weakly bound and the other more tightly bound. Another luminescence center has been observed from room-temperature electron-irradiated 4H-SiC, called E_A [60]. The spectrum shows a couple of sharp no-phonon lines together with a broad phonon-assisted structure. Annealing at around 750 °C causes an abrupt change in the PL spectrum, whereas further annealing at temperature above 750 °C results in the dominance of the strong D_1 spectrum (Fig. 2.90). Forty no-phonon lines are observed from the E_A spectrum in the range of 2.8–2.9 eV. Based on photoluminescence excitation spectroscopy, the E_A spectrum is proposed to originate from recombination of the excitons bound to isoelectronic defect centers.

2.7 Surface Structures

Silicon carbide has many polytypes, and each polytype has its own crystal structure and specific surface structure. The surface atoms in silicon carbide alter the bonding structures to terminate partial dangling bonds by forming Si–Si bonds, C–C bonds, double or triple bonds, or bonding with foreign atoms. On the other hand, silicon carbide is a compound semiconductor that is composed of two

elements and both silicon and carbon atoms on the surface can react with various elements such as hydrogen and oxygen to produce different surface chemical structures. Therefore, silicon carbide has rather complex surface structures, which affect its electrical and optical properties. Some surface defects can significantly alter the normal performance of SiC-based electronic devices, and so there has been extensive investigation on the surface structures of silicon carbide. Here, the major phenomena involving the surface of silicon carbide are reviewed briefly.

2.7.1 Surface Reconstruction

In general, on the semiconductor surface, owing to the absence of atoms on the air side of the semiconductor/air interface, the surface atoms experience different forces compared to the interior ones. As a result, the surface structure relaxes and reconstructs to attain the minimum surface energy. Assume that the reconstructed surface has a two-dimensional lattice with unit vectors of \mathbf{b}_1 and \mathbf{b}_2 , the substrate surface has two-dimensional lattice with unit vectors of \mathbf{a}_1 and \mathbf{a}_2 , and on a certain substrate crystal surface $X\{hkl\}$, reconstruction is given by $(\mathbf{b}_1 \parallel \mathbf{a}_1, \mathbf{b}_2 \parallel \mathbf{a}_2)$, and then we have:

$$\mathbf{b}_1 = p\mathbf{a}_1, \mathbf{b}_2 = q\mathbf{a}_2, \quad (2.7)$$

where p and q are two proportionality factors. In general, the reconstructed surfaces are denoted by the following notations [170]:

$$X\{hkl\}(p \times q), X\{hkl\}c(p \times q), \text{ or } X\{hkl\}(p \times q) - R^\circ, \quad (2.8)$$

where c represents a possible center, and R° denotes the angles by which the reconstructed surface rotates relative to the substrate surface.

It is very difficult to determine the atomic positions of the reconstructed surface experimentally. Investigators generally utilize scanning tunneling microscopy (STM) and low-energy electron diffraction (LEED) to experimentally study SiC surfaces. First-principle calculation and ab initio molecular dynamics simulation have also been adopted to theoretically study SiC. Based on the experimental and theoretical results, various structural models have been proposed. The (100) surface on cubic SiC is one of the most widely studied surfaces of SiC. This surface has several types of surface reconstruction such as the C-terminated $c(2 \times 2)$ surface, Si-terminated 2×1 surface, and Si-rich 3×2 surface.

The atomic-resolution images obtained by STM reveal that the 3C-SiC(001) surfaces have Si adlayers on the Si-terminated surface [171]. An additional dimer-row model for the surface with extra Si atoms shows structural features consistent with STM and LEED. The unit cell of the Si-saturated (3×2) surface observed by LEED comprises a pair of additional Si dimers on the Si-terminated surface forming a straight line along the direction through the centers of two constituent

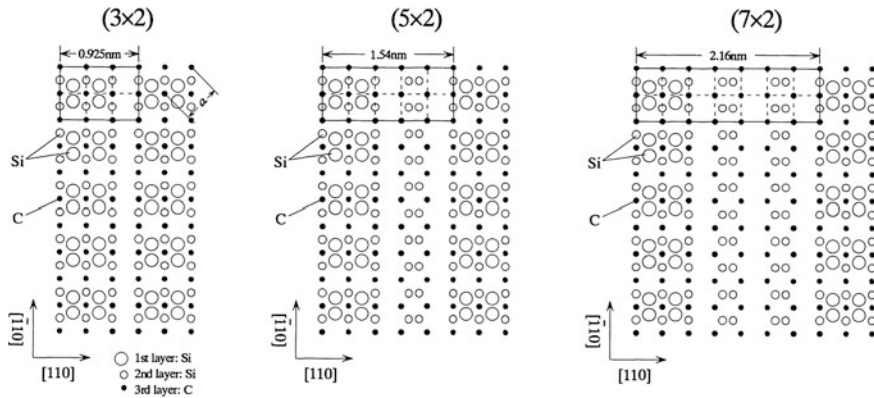


Fig. 2.91 3C-SiC(001)-(3×2), (5×2), and (7×2) structural models. Reprinted with permission from [171]. Copyright 1994, American Physical Society

atoms of a dimer (Fig. 2.91). There are also reconstruction models for the (5×2) and (7×2) surfaces in which the unit cell of the uppermost atomic layer also consists of a pair of additional Si dimmers.

Clear atom images of individual Si dimers are observed from the Si-rich 3C-SiC(100)-(3×2) surfaces by STM [172]. The samples have a high-quality surface with a low defect density (Fig. 2.92). The STM image shows that the Si-Si dimmers form rows perpendicular to the dimer direction in a (3×2) atomic arrangement with clear evidence of asymmetric dimers tilted in the same direction (not alternate tilting). This is a very open atomic surface arrangement. On the top atomic layers, three types of defects are identified, namely missing dimmers (type A), dimer pairs (type B), and dimers having different tilt angles (type C). The proposed structure model is illustrated in Fig. 2.93. This model is based on the clear identification of individual Si atoms from the STM topography (filled and empty electronic states). This model gives a Si-coverage of $1/3$, different from conclusions drawn in the aforementioned STM study [171] where there is a coverage of $2/3$ with pairs of Si dimers oriented parallel to the rows (Fig. 2.91).

The structural and electronic properties of five different configurations of polar 3C-SiC (001) surfaces are studied by self-consistent ab initio calculation [173]. No dramatic Si dimmers on the Si-terminated (2×1) surfaces are found, whereas strong carbon dimmers are found from various C-terminated surfaces serving as the reconstruction building blocks. The 3C-SiC(100)- $c(4 \times 2)$ surface reconstruction is studied by atomic-resolution STM [174]. The STM images agree well with the corresponding STM image calculation (Fig. 2.94). A model of dimer rows is proposed. In this picture, the dimer row consists of alternatively up and down dimers within the row in an “undulating” type of arrangement so as to reduce the surface stress. The 3C-SiC(100) and Si(100) have different $c(4 \times 2)$ surface reconstruction. The straight, long, and highly stable Si atomic lines self-organized on the 3C-SiC(100) surfaces are observed by STM [175]. The Si atomic lines are composed of

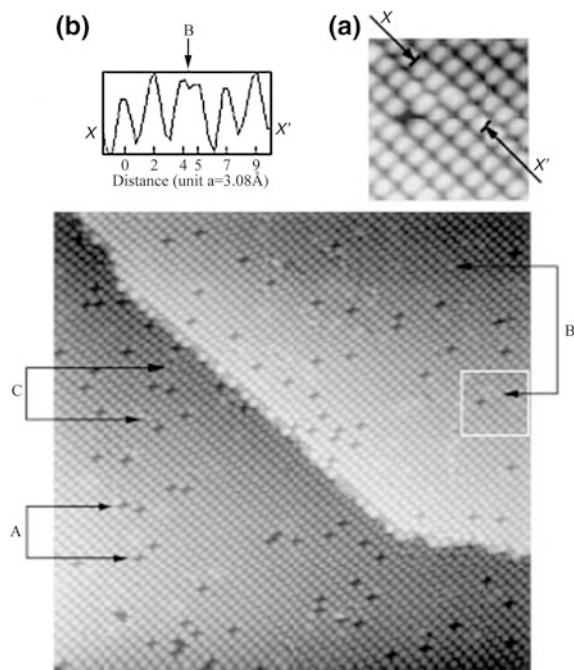


Fig. 2.92 $40 \times 40 \text{ nm}$ STM image (*filled states*) of the 3C-SiC(100)- (3×2) surface with A , B , and C denoting three types of defects. **a** Magnified image of the area having type A (*missing dimer*) and B (*dimer pair*) defects. **b** Atomic profile of dimers along the xx' -axis displaying the two components of a dimer pair (marked by B). Reprinted with permission from [172]. Copyright 1996, American Physical Society

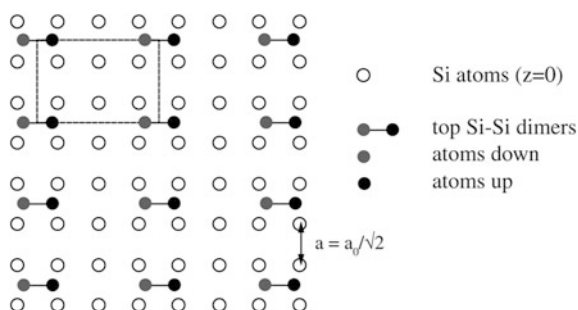


Fig. 2.93 Schematic of the 3×2 Si-Si dimers on a nonreconstructed 3C-SiC(100) surface. The surface primitive unit cell parameter is $a = a_0/\sqrt{2}$, and a_0 (4.36 \AA) is the 3C-SiC lattice constant. The dashed line refers to the (3×2) unit cell. Reprinted with permission from [172]. Copyright 1996, American Physical Society

Si dimers formed by annealing of the primary 3C-SiC(100)- (3×2) structure at above $1,000^\circ \text{C}$ (Fig. 2.95). The number and spacing of the Si atomic lines can be controlled by the annealing time and temperature. The density of the Si atomic lines

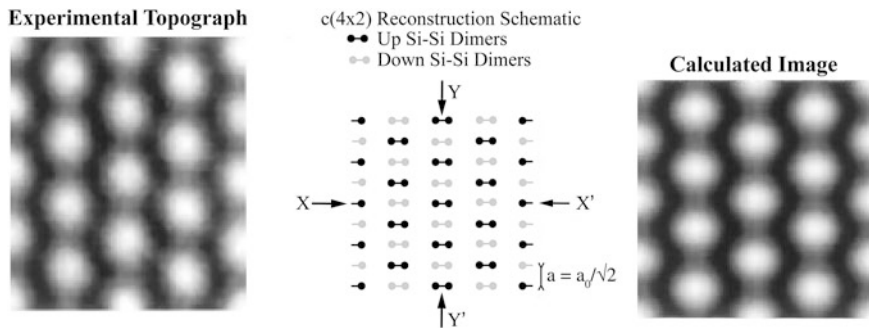


Fig. 2.94 Experimental STM topographical image (filled electronic states) of the Si-terminated 3C-SiC(100)- $c(4 \times 2)$ surface showing the Si dimers (*left panel*) and schematic of this surface showing the alternating up and down dimers (*middle panel*). The unreconstructed surface primitive lattice parameter is $a = a_0/\sqrt{2}$, where $a_0 = 4.36 \text{ \AA}$ is the 3C-SiC lattice constant. The right panel shows the calculated STM image. Reprinted with permission from [174]. Copyright 1997, American Physical Society

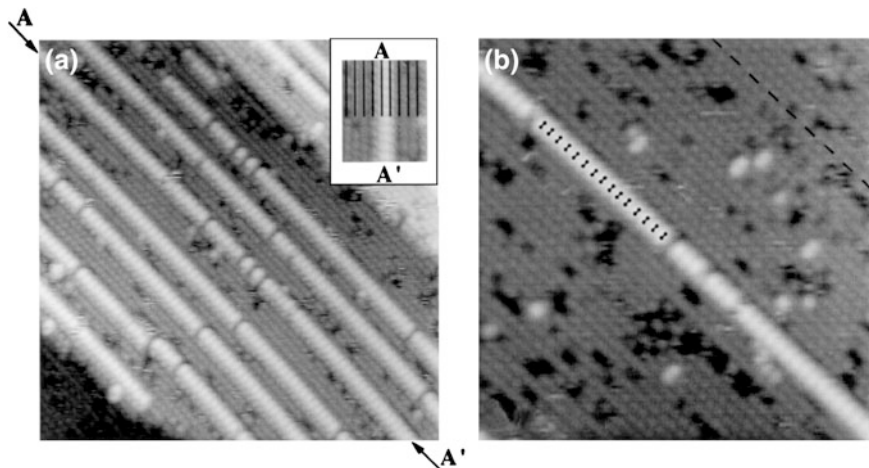
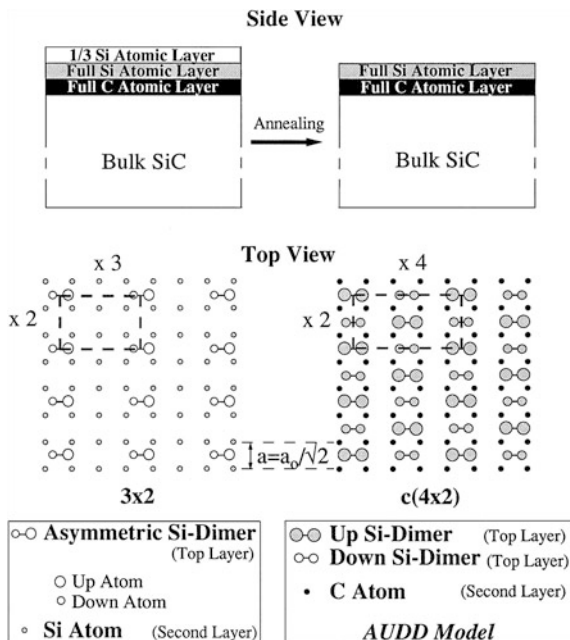


Fig. 2.95 **a** $32 \times 32 \text{ nm}$ STM topographical image of the 3C-SiC(100)- (3×2) surface after annealing at $1,100^\circ\text{C}$. There are Si atomic lines along with $c(4 \times 2)$ surface reconstruction between them. **b** $20 \times 20 \text{ nm}$ STM topographical image of 3C-SiC(100)- (3×2) surface after annealing at $1,150^\circ\text{C}$. A single Si-dimer line is displayed. The dark dashed line in the top right corner denotes the $c(4 \times 2)$ dimer-row direction. Reprinted with permission from [175]. Copyright 1997, American Physical Society

decreases with temperature until the isolated Si atomic lines are observed. The phase transition is observed with annealing. The 3C-SiC(100)- (3×2) surface transforms to the 3C-SiC(100)- $c(4 \times 2)$ surface on which the Si atomic lines site. These atomic channels form upon the phase transition between the (3×2) and $c(4 \times 2)$ reconstruction by selective Si atom organization. Figure 2.96 describes

Fig. 2.96 Schematic of the 3C-SiC(100)-(3 × 2) and 3C-SiC(100)-c(4 × 2) reconstructed surfaces. Annealing induces phase transition between them. Reprinted with permission from [175]. Copyright 1997, American Physical Society



these two surface reconstructions. The Si atomic lines result in a lateral mismatch between the $c(4 \times 2)$ Si-dimer rows. Formation of the carbon atomic chains is also observed from the C-terminated 3C-SiC(100) surfaces by atom-resolved STM [176]. These carbon atom lines are thermally stable up to 1,200 °C. They comprise buckled single bond sp^3 C-C dimers with the direction perpendicular to the sp C \equiv C triple bond dimers forming a $c(2 \times 2)$ surface reconstruction. Their density increases with annealing time, and they do not cause or come from surface anti-phase boundaries. The anisotropic tensile or compressive surface stress is proposed as a leading driving force in this carbon $sp \rightarrow sp^3$ diamond-like transformation.

The atomic structure of the 3C-SiC(100)- $c(2 \times 2)$ surface is studied using dynamic calculation of low-energy electron diffraction intensities [177]. The $c(2 \times 2)$ surface is prepared in an ultrahigh vacuum by removal of surface silicon in high-temperature annealing or deposition of surface carbon by exposing the stoichiometric (2×1) surface at 1,125 K to C_2H_4 . Both samples contain surfaces terminated with C_2 groups in staggered silicon bridge sites (Fig. 2.97). The difference is that the surface created by silicon sublimation contains weak silicon dimer bonds in the second atomic layer of the $c(2 \times 2)$ surface, whereas the C_2H_4 -generated $c(2 \times 2)$ surface has no such dimer bonds. Thermal decomposition of C_2H_4 yields hydrogen that saturates silicon dangling bonds in the second atomic layer, thus prohibiting the formation of the Si dimers. Ab initio calculation of the reconstruction of the 3C-SiC(100) surfaces confirms that the lowest energy $c(2 \times 2)$ reconstructed surface comprises triply bonded carbon dimers in a

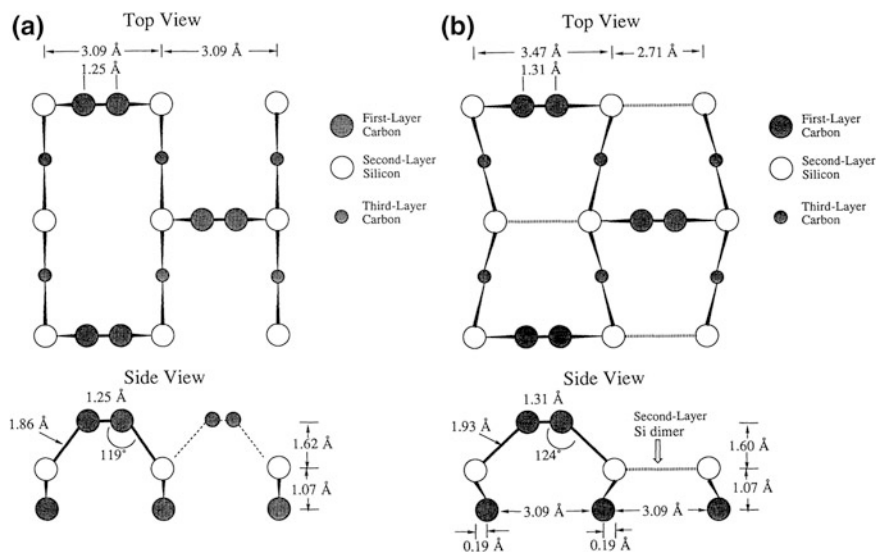


Fig. 2.97 Schematic of the best fit structure of the 3C-SiC(100)- $c(2 \times 2)$ surface produced by **a** C_2H_4 exposure and **b** Si sublimation. Reprinted with permission from [177]. Copyright 1991, American Physical Society

bridging position between neighboring underlying silicon dimers [178]. Additionally, the most stable structure of the (3×2) reconstructed surface with a $1/3$ monolayer excess of silicon is an alternate dimer-row structure. In another study, the single-domain 3C-SiC(100)- $c(2 \times 2)$ surface structure is investigated utilizing the polarization dependence of two C-1s and Si-2p absorption as revealed by near edge X-ray absorption fine structure combined with molecular orbital cluster calculation [179]. The surface is terminated with staggered rows of unusual, nearly triply bonded C dimers bridging underlying Si dimers. The electronic structure of the C dimers is determined by resonant valence-band photoemission accompanying C-1s exciton auto-ionization. The ab initio molecular dynamics simulation indicates that under different preparation conditions and thermal treatment, the C-terminated (001) surfaces of 3C-SiC can have different $c(2 \times 2)$ and $p(2 \times 1)$ reconstructions [180]. The atomic structure of the C-terminated 3C-SiC(100)- $c(2 \times 2)$ reconstructed surface is investigated by STM and surface-core-level-resolved photoelectron diffraction [181]. This surface is found to consist of anomalous bridge-bonded C dimers with a C-C bond length of 1.22 \AA . The angle-resolved photoemission study identifies two occupied π state bands attributed to the normal and parallel p orbitals of the triple-bonded C dimers, and this explains the stability of the triple-bonded surface reconstruction.

There are fewer reports on the 3C-SiC(111)- (3×3) -reconstructed surfaces, although this surface structure has been investigated by STM, conventional low-energy electron diffraction (LEED), LEED holography, and density functional theory [182]. STM reveals a single adatom per unit cell. LEED and density

functional theory results reveal a Si tetramer on a twisted Si adlayer with clover-like rings. This twist model with one dangling bond left per unit cell is a novel $(n \times n)$ -reconstruction mechanism for group IV (111) surfaces.

Hexagonal SiC may also exhibit the (3×3) reconstruction. The drastic (3×3) reconstructions of 3C-SiC(111), 4H-SiC(0001), and 6H-SiC(0001) surfaces are identified by quantitative LEED and holographic interpretation of diffraction intensities, STM, and Auger electron spectroscopy [183]. This observed (3×3) reconstruction is a new type of semiconductor $(n \times n)$ surface reconstruction, showing the feature of considerable reduction of surface dangling-bonds. A modified version of the (3×3) reconstruction, that is, the 6H-SiC(0001)- (3×3) -Si reconstruction, is observed by STM [184]. The surface has a hexagonal structure with one Si adatom per unit cell. A reconstruction model in which the unit cell comprises 11 Si atoms is proposed. There are three dimers and three rest atoms in the first layer and one adatom in the second layer. In the first layer, the dimers and other atoms form six- and nine-atom rings that surround unoccupied sites of the outermost silicon atoms of the substrate. For the three dangling bonds in a unit cell, one belongs to the adatom and the other two belong to the silicon atoms of the substrate. STM conducted on the 6H-SiC Si-terminated (0001) and C-terminated (000 $\bar{1}$) surfaces [185] shows that the (3×3) reconstruction arises after annealing at 850 °C followed by transformation to the $(\sqrt{3} \times \sqrt{3})$ reconstruction after further annealing at 950 °C. The (3×3) surface has a 4/9 monolayer of adatoms, and the $(\sqrt{3} \times \sqrt{3})$ surface has a 1/3 monolayer of adatoms. A new (9×9) reconstruction on the (0001) surface is observed after further annealing the (3×3) surface at 900 °C under a silicon flux. A graphitized surface with a (6×6) reconstruction is observed from the (0001) surface when the temperature is suddenly raised to 1,150 °C without a silicon flux.

Oxidation and HF etching of the 6H-SiC (0001) surface can produce an atomically flat surface on a 100-nm scale with bulk-like periodicity and stoichiometry [186]. The surface dangling-bonds are terminated by hydroxyl groups. Thermal treatment can remove the remaining oxygen from the surface and yield the carbon $\sqrt{3} \times \sqrt{3}$ $R30^\circ$ reconstructed surface where carbon-carbon bonds are present on the surface. The $\sqrt{3} \times \sqrt{3}$ reconstruction of the Si-terminated 6H-SiC(0001) surface is investigated by STM [187]. The STM images are consistent with a structural model composed of 1/3 layer of Si or C adatoms in threefold symmetry sites on top of the outermost Si-C bilayer. Several types of defects are observed from the $\sqrt{3} \times \sqrt{3}$ surfaces. The first-principle total energy calculation determines the chemical identity and adsorption site of the adatoms on the SiC(0001) $\sqrt{3} \times \sqrt{3}$ surface [188]. Over the entire range of thermodynamically allowed chemical potentials, Si adatoms are preferred over C adatoms. The adatoms prefer the T_4 site over the H_3 site for both Si and C. The calculation shows that in the Si- T_4 model, there is a half-filled adatom dangling-bond band at 1.2 eV above the valence-band maximum with a bandwidth of 0.35 eV. The SiC(0001) $\sqrt{3} \times \sqrt{3}$ surface is studied by angle-resolved photoemission spectroscopy [189].

The 6H and 4H polytypes show similar results. A surface state band with semi-conducting occupation at around 1.0 eV above the valence-band maximum with a width of about 0.2 eV is observed. The 6H-SiC(0001) $\sqrt{3} \times \sqrt{3}$ $R30^\circ$ and $6\sqrt{3} \times 6\sqrt{3}$ $R30^\circ$ reconstructed surfaces are studied by photoemission spectroscopy [190]. The reconstructed surfaces are fabricated by heating the unreconstructed 1×1 surface to 950 and 1,150 °C, respectively. These surfaces show no oxygen-related signals. The spectral features for the $\sqrt{3}$ reconstruction cannot be explained by a structural model composed of Si or C adatoms on top of a Si–C bilayer. The $6\sqrt{3}$ reconstructed surface contains a larger amount of carbon atoms. The carbon is not graphitic, and graphitization is observed only after the surface is heated to a high temperature. The relaxed and $\sqrt{3} \times \sqrt{3}$ $R30^\circ$ reconstructed 6H-SiC(0001) surfaces are investigated by ab initio calculation in the framework of the density functional theory with the local density approximation [191]. Both the Si- and C-terminated reconstructed surfaces are examined. Eight structural models are optimized for the reconstructed surfaces with Si or C adatoms and Si or C trimers adsorbed in threefold-symmetric T_4 or H_3 positions. For the Si-terminated surface, the optimal surface structure involves Si adatoms in T_4 sites and it is consistent with experimental results. For the C-terminated surface, none of the investigated $\sqrt{3} \times \sqrt{3}$ adatom or trimer configurations is the optimal configuration. STM conducted on the 6H-SiC(0001) $\sqrt{3} \times \sqrt{3}$ surfaces of both *n*- and *p*-type materials with low tunnel currents reveals distinct bands of empty and filled states [192]. The density of states with semiconductor features contains a state about 1 eV above the Fermi level and another state 1 eV below the Fermi level. STM images of the surface taken at positive and negative polarities indicate that these two states are localized in the same spatial position, thus supporting a silicon adatom model that predicts a Mott-Hubbard-type density of states.

2.7.2 SiC–SiO₂ Interface

Silicon carbide has a native oxide on the surface, and this is a big advantage for application in electronic devices. However, in practice, there may be many active defects at the interface between the SiC wafer and surface silicon dioxide layer. The defects significantly degrade the performance of SiC-based electronic devices and much work has been done to investigate SiC/SiO₂ interfaces both experimentally and theoretically. Several types of defects are supposed to be responsible for the degradation of the SiC-based devices, including carbon clusters, silicon suboxides, and Si–C–O clusters. Researchers have also thought of some efficient approaches to mitigate these unfavorable defects.

In hexagonal SiC, the Si-terminated surface has a slower oxidation rate compared to the C-terminated surface and this difference is caused by an unknown interface compound. The angle-resolved XPS study of the oxidized Si-(0001) and

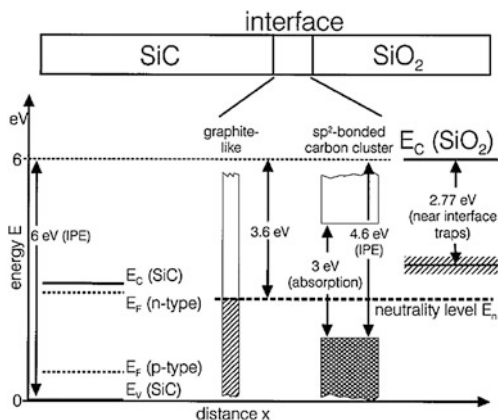


Fig. 2.98 Schematic of the carbon cluster model of the interface states in the SiC/SiO₂ metal-oxide-semiconductor structures. The dominant interface states are the sp²-bonded carbon clusters with wide energy gaps (3 eV) and graphite-like carbon clusters. The near-interface oxide traps are located at 2.77 eV below the conduction-band minimum of SiO₂. Reprinted with permission from [195]. Copyright 1997, Wiley-VCH Verlag GmbH & Co. KGaA

C-(000 $\bar{1}$) surfaces of 6H-SiC reveals the interfacial oxide Si₄C_{4-x}O₂ ($x < 2$) [193]. The slow oxidizing Si-(0001) surface has this oxide with a large thickness (1 nm), whereas the C-(000 $\bar{1}$) surface has smaller one and it diminishes quickly upon oxidation above 1,000 K. The electronic structure of the SiC/SiO₂ interfaces for different SiC polytypes (3C, 4H, 6H, 15R) is investigated by internal photoemission of electrons [194]. The SiC valence-band maximum is located at 6 eV below the oxide conduction-band edge for all polytypes. The interface states are found in the energy range up to 1.5 eV above the top of the SiC valence band. The electron spectrum is similar to that of sp²-bonded carbon clusters, demonstrating the existence of elemental carbon at the SiC/SiO₂ interface. Using electrical analysis and internal photoemission spectroscopy, the energy distribution of the electron states at the SiC/SiO₂ interfaces produced by oxidation of various SiC polytypes (3C, 4H, 6H) is determined [195]. Different polytypes show similar distributions of interface traps over the SiC bandgap indicative of a common nature of the interfacial defects. The major defects are proposed to be the carbon clusters at the SiC/SiO₂ interface and near-interfacial defects in SiO₂ (Fig. 2.98). In contrast, no signals from the dopant-related defects and dangling bonds at the SiC surface are observed. A large density of interface states at around 0.1 eV below the conduction band of 4H-SiC at the SiC/SiO₂ interface is revealed in low-temperature electrical measurements and photon-stimulated electron tunneling experiments [196]. These states are ascribed to the defects in the near-interfacial oxide layer, and they can significantly trap the electrons from the SiC. These states may cause degradation of the electron mobility observed from the surface channel of the 4H-SiC/SiO₂ electronic devices.

Electron energy loss spectroscopy (EELS) conducted on the thermally grown SiO₂/6H-SiC (0001) interfaces reveals high carbon concentrations at distinct

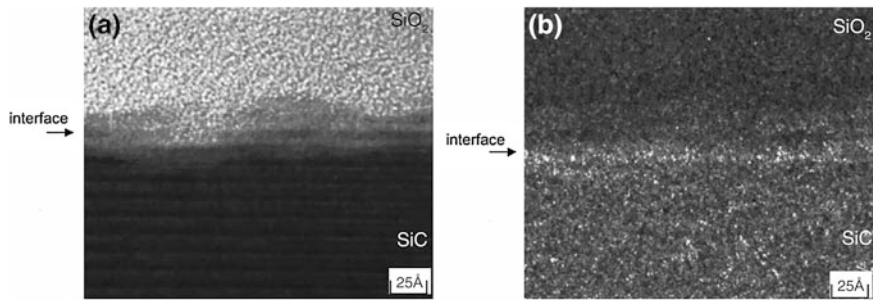


Fig. 2.99 **a** HRTEM image and **b** corresponding electron energy loss spectroscopy map of C at a thermally grown SiO₂/6H-SiC (0001) interface. Reprinted with permission from [197]. Copyright 2000, AIP Publishing LLC

interface regions [197]. These C-rich regions have a thickness of about 1.0–1.5 nm (Fig. 2.99). The oxides are grown on clean *n*-type 6H-SiC at 1,100 °C in a wet oxygen ambient. EELS shows that the CVD-deposited SiO₂/SiC interfaces have no C-rich regions. The interface state density in the metal-oxide-SiC diodes with thermally grown SiO₂ is about $9 \times 10^{11} \text{ cm}^{-2} \text{ eV}^{-1}$ at $E - E_v = 2.0 \text{ eV}$. This is consistent with the experimental value for the SiC metal-oxide-semiconductor (MOS) diodes without post-oxidation annealing. These C-rich regions may contribute to the low channel mobility in the SiC-based metal-oxide-semiconductor field-effect transistors (MOSFETs). Density functional calculation is employed to study the possible defect structures arising from the interaction between O₂ molecules and an ideal portion of the SiC/SiO₂ interface [198]. The defect structures produced along the calculated oxidation routes remain at the interface in a significant concentration as oxidation ceases. The carbon–carbon bonds can explain most of the observed interfacial states but not the large density near the conduction band of 4H-SiC. These electron traps with very high density near the conduction band of 4H-SiC in the metal-silicon dioxide-SiC structures are called near-interface traps (NIT). By means of capacitance–voltage and thermal dielectric relaxation current analysis, the near-interfacial traps close to the 4H-SiC conduction-band edge in the 4H-SiC-based MOS structures with either thermal or deposited oxide are investigated [199]. The signals corresponding to two groups of trap levels are detected, and the total trapped charge exceeds $1 \times 10^{13} \text{ cm}^{-2}$. The observed density and energy distribution of these traps are nearly identical in all thermal and deposited oxides, suggesting that they are intrinsic defects at the SiO₂/SiC interface. The high-resolution electron microscopy combined with electron energy loss spectroscopy show no sign of graphitic region at the SiO₂/SiC interface or in the bulk SiO₂ at a detection limit of 0.7 nm in samples after re-oxidation. No amorphous carbon is observed near the SiO₂/SiC interface, suggesting that the near-interface traps close to the 4H-SiC conduction band are not related to the carbon structures at the interface. Sometimes, the near-interface traps are assumed to originate from oxides near the interface. The positions of the intrinsic and carbon defects in SiO₂ are investigated by density functional calculation [200].

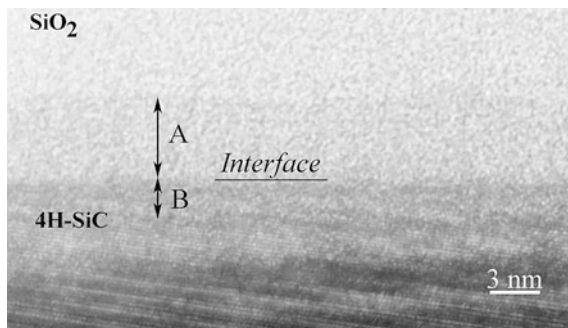


Fig. 2.100 HRTEM image of the SiO_2 /4H-SiC interface showing the transition layers A (4.8 nm) and B (3.3 nm) on either side of the interface. Reprinted with permission from [201]. Copyright 2008, AIP Publishing LLC

The vacancies and oxygen interstitials can be excluded as the origin of the near-interface traps, whereas silicon interstitials and carbon dimers generate gap levels in the energy range inferred from experiments. Using TEM and EELS, the structure and chemistry of the interface of the thermally grown SiO_2 /4H-SiC heterostructure are analyzed [201]. Distinct layers several nanometers thick on each side of the interface as well as partial amorphization of the SiC surface are observed (Fig. 2.100). These interfacial layers are ascribed to the formation of a ternary Si-C-O phase during thermal oxidation.

Some efficient methods have been exploited to diminish the surface defects at the SiC/SiO₂ interface so as to improve the performance of the SiC-based MOS devices. Pre-oxidation cleaning of SiC (3C, 4H, 6H polytypes) surfaces by exposing to ultraviolet radiation and oxygen is found to result in significant improvement in the electronic properties of SiC/SiO₂ interfaces [202]. This treatment removes the defect species that are otherwise present at the interface after thermal oxidation of SiC. Carbon clusters are suggested as the diminished defect species responsible for a substantial part of the SiC/SiO₂ interface states. Nitridation is another efficient way to mitigate the defects at the SiC/SiO₂ interface. Analysis of fast and slow traps at the interface of 4H-SiC with oxide grown in O₂, N₂O, and NO indicates that the major positive effect of nitridation is the dramatic reduction of the slow electron trap density [203]. These traps may be the defects in the near-interfacial oxides. This study confirms that nitridation also reduces the fast interface states associated with clustered carbon. Although nitridation has a positive effect in improving the SiC/SiO₂ interface quality, this effect can be saturated. Nitridation with NO significantly reduces the interfacial trap density near the conduction band, but this effect is saturated at $2.5 \times 10^{14} \text{ cm}^{-2}$ of nitrogen leaving a trap density that is still higher than that in silicon [204]. Nitrogen passivation results in dissolution of the defects leading to lowered trap energy in the bandgap. This behavior is consistent with a model in which the energy of the trap of carbon clusters or silicon suboxide depends on the defect size. The nitrogen and hydrogen effects on the SiC-SiO₂ interfaces have

been investigated both experimentally and theoretically [205]. The system studied is the Si-terminated SiC faces in metal-oxide-semiconductor structures. H_2 shows no effect on the density of electrically active interface defects, but in contrast, nitridation followed by hydrogenation yields complementary passivation and substantial reduction in the interface defects. First-principle calculation indicates that isolated C dangling bonds can be passivated by H_2 , whereas correlated C dangling bonds on neighboring threefold-coordinated C atoms can only be passivated by monatomic H. Different from previous viewpoints regarding the carbon clusters as the SiC–SiO₂ interface defects, carbon is proposed to exist as a bonded Si–C–O interlayer (one to two atomic layers) and the correlated C dangling bonds are supposed to be the major origin of the observed interface defects. The effect of nitridation is proposed to convert the Si–C–O bond into a Si–C–O–N bond along with reduction in threefold C atoms (N replaces threefold C). The hydrogen atoms result in the conversion of Si–C–O–N to Si–C–O–N–H, thus reducing the interfacial states. The residual interface states are ascribed to the Si–Si defects at the interface. Detailed calculation performed on the 4H-SiC/SiO₂ interface by density functional theory [206] reveals that the hole traps near the valence-band edge stem from carbon–carbon bonds, whereas the amphoteric states deep in the bandgap arise from the dangling bonds. The chemical disorder contributes interfacial states with energies close to both band edges. However, the observed electron traps with a large density near the conduction band are proposed to be defects in the oxide near the interface. Silicon interstitials are found to yield a broad distribution of electron traps slightly farther from the conduction-band edge, whereas the carbon dimers substituting for two nearby oxygen atoms in the silica network may give rise to the sharp peak of electron traps with critically high density at about 0.1 eV below the conduction-band edge of 4H-SiC. The analysis also shows that NO or N atoms attack the carbon dimers at the interface, thereby eliminating carbon.

The transconductance of 4H-SiC MOSFETs is typically much lower compared to the 6H-SiC-based devices. Using a modified capacitance–voltage technique, the large area 4H-SiC MOSFETs are studied and the relationship between the SiC/SiO₂ interface trap density and energy in the bandgap is investigated [207]. The interfacial trap density increases toward the conduction-band edge in both polytypes and it is much higher in 4H-SiC compared to 6H-SiC for devices fabricated in the same lot. As a result, the 4H-SiC-based devices will trap more inversion electrons, thus resulting in the lower transconductance with respect to the 6H-SiC-based devices.

There is a question on whether the SiC/SiO₂ interface can be prepared without many interface defects. The highly ordered monolayers of silicon dioxide have been prepared on the hexagonal (0001) 4H and 6H silicon carbide surfaces by hydrogen plasma or etching in hydrogen [208]. Low-energy electron diffraction and Auger electron spectroscopy reveal that the bond angles and distances of the surfaces are in agreement with those of bulk SiO₂. The semiconductor surface is passivated as a result of saturation of all the dangling bonds and it preserves the perfect order also in air. These ideal oxide monolayers may act as a seed for fabricating epitaxial oxides with a small defect density.

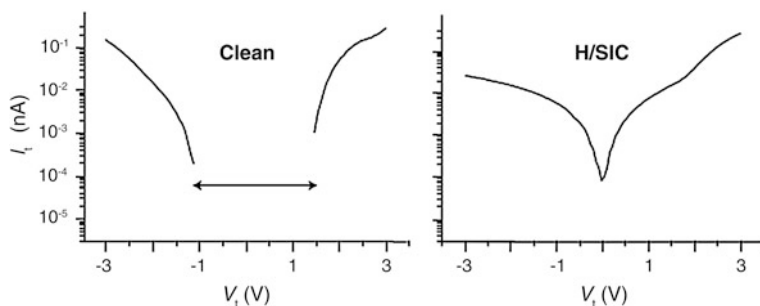


Fig. 2.101 Electronic structure of the clean and H-exposed β -SiC(100) 3×2 surface obtained by surface tunneling spectroscopy. The spectra show gap closing of the H-treated β -SiC(100) 3×2 surface. Reprinted with permission from [211]. Copyright 2003, Macmillan Publishers Ltd

2.7.3 Other Types of Surface Treatment

Surface functionalization of silicon carbide with species other than oxygen has been pursued. Atomically flat surfaces are fabricated by hydrogen etching of 6H- and 4H-SiC (0001) surfaces at 1,600–1,700 °C [209]. Etching eliminates scratches on the polished substrates and atomic force microscopy images disclose periodic arrays of atomically flat terraces that are a few hundred nanometers wide. The terraces are separated by 1.5-nm-tall steps in the $\langle 1100 \rangle$ directions. Hydrogenated 6H-SiC (0001) and (000 $\bar{1}$) surfaces are also obtained by high-temperature hydrogen treatment [210]. The samples exhibit unreconstructed surfaces with a high crystallographic order as revealed by low-energy electron diffraction. Sharp Si–H stretching modes are observed from the SiC (0001) surfaces. The *n*- and *p*-type samples show no surface band bending, indicating that the surfaces are electronically passivated, and densities of charged surface states in the gap are below $7 \times 10^{10} \text{ cm}^{-2}$ for *p*-type and $1.7 \times 10^{12} \text{ cm}^{-2}$ for *n*-type samples. No surface oxide is detected by X-ray photoelectron spectroscopy after the samples are kept in air for two days. Atomic hydrogen can induce surface metallization on the SiC surface [211]. This is realized on the surface of the single-domain β -SiC(100) thin film prepared on a silicon substrate (Fig. 2.101). Photoelectron and photoabsorption spectroscopies and scanning tunneling techniques show that metallization takes place in the subsurface region of the 3×2 reconstruction. Metallization is proposed to arise from the competition between hydrogen termination of surface-dangling bonds and hydrogen-generated steric hindrance below the surface.

Ab initio molecular dynamic simulation shows that water molecules interact differently with Si- and C-terminated 3C-SiC(001) surfaces [212]. The water coverage is selected to be 1/4 to 1 monolayer and water molecules tend to dissociate on the Si-terminated surface leading to the formation of Si–H and Si–OH bonds on the surface. In contrast, the C-terminated surface that does not react with water molecules is hydrophobic.

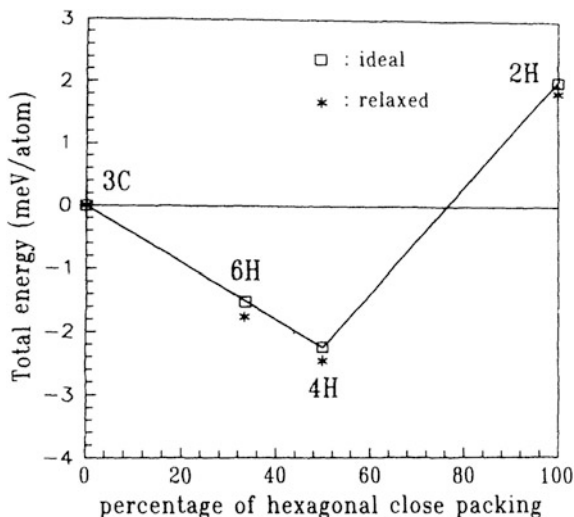
Organic molecules can be attached to the silicon carbide surface and this type of passivation is often necessary for biological applications of silicon carbide. The alkyl monolayers can be covalently bound to the 3C-SiC surface via a thermal reaction with 1-alkene [213]. The SiC wafer is first treated in a diluted HF solution to remove the native SiO₂ layer and provide a reactive hydroxyl surface. Attachment of ω -functionalized 1-alkene produces a well-defined surface that is covalently bound by the alkyl monolayer. The attached monolayers are covalently attached and the resulting surface is stable under both acidic and alkaline conditions. The alkyl monolayers can also be formed on 3C-SiC by UV irradiation in the presence of alkenes at room temperature [214]. Methyl undec-10-enoate and 2,2,2-trifluoroethyl undec-10-enoate can be bonded to the SiC surfaces, and the ester-terminated surfaces allow for further attachment of amine compounds. Using the density functional simulation, molecular sensitization of the nonpolar SiC(110) surface is studied [215]. Aromatic fragments up to a full porphyrin molecule are considered and the result shows that there is a relatively low affinity between aromatic rings and SiC surface. The only exception is the pyrrole ring that produces an exothermic reaction leading to the stable hybrid interfaces. Functionalization of *n*-type (100) and (111) 3C-SiC surfaces with organosilanes has been reported [216]. The wet chemical technique produces self-assembled monolayers of amino-propyldiethoxymethylsilane and octadecyltrimethoxysilane on the 3C-SiC surfaces. The reaction on the hydroxylated surfaces with organosilane diminishes the surface band bending, suggesting that functionalization results in partial passivation of electrically active surface states.

2.8 Polytypic Transformation

Silicon carbide has many polytypes having different stacking sequences of Si-C double-atomic layers. This property renders silicon carbide a very special semiconductor but what is so special about the material that so many crystal structures exist in nature? Much work has been done with the intention to clarify this mystery. The study also reveals that one polytype of silicon carbide can transform into another polytype under appropriate conditions such as under pressure and there have been many investigations concerning the phase transformation between different polytypes of silicon carbide.

In general, theoretical calculation is utilized to explore the origin of polytypism and structural and electronic differences among different polytypes of silicon carbide. Cheng, Needs, and Heine have presented a model to account for the origin of polytypism in silicon carbide [217]. Ab initio quantum mechanical calculation of the total energies of five simple SiC polytypes with norm-conserving pseudopotentials shows that the system is extremely close to a multiphase degeneracy between all the considered structures. Two mechanisms can split the infinite multiphase degeneracy and give an infinite number of regular SiC structures. The first is a result of the presence of phonons. The second depends on two aspects, an

Fig. 2.102 Calculated crystal total energies of the SiC polytypes with respect to that of the 3C structure as a function of the hexagonal close packing percentage. Reprinted with permission from [28]. Copyright 1994, American Physical Society



electronically mediated interaction between planes that need not be long ranged but depends on their separation, thus giving forces on the layers, and the longitudinal relaxation of the interlayer spacings in response to the above forces. There is a paradox regarding the growth of SiC polytypes from the vapor or the melt [218]. Since cubic silicon carbide is not the structure with the lowest energy as shown by calculation, it is perplexing why the cubic structure is preferred. This is explained by calculations as due to the constrained equilibrium when adding one atomic double layer at a time to the growing crystal in the hexagonal direction without allowing rearrangement of the lower layers. The different roles of donor and acceptor impurities have been discussed. The electronic structure calculation indicates that the valence-band offset between different polytypes is small, and therefore, there should be large offsets between the conduction bands due to the different bandgap values. As a result, the acceptors do not favor any particular polytype and donors favor the cubic form since it has the smallest bandgap.

The structural and electronic properties of various polytypes (3C, 2H, 4H, 6H) of SiC have been determined by ab initio pseudopotential calculation [28]. All the polytypes show similar equilibrium lattice constants and bulk moduli. The calculated total energies of the polytypes are very close and the difference is within 4.3 meV/atom (Fig. 2.102). The small difference may account for the polytypism of silicon carbide. 2H-SiC is found to be the most unstable, whereas 4H-SiC has the lowest energy due to the attractive interactions between the alternating cubic and hexagonal stacking layers. The asymmetric charge distribution for a Si-C bond is found to be on the boundary separating the zinc-blende and wurtzite phases and suggested to be related to the polytypism of silicon carbide. The ground-state properties of cubic and hexagonal SiC polytypes are investigated by the softened ab initio pseudopotentials and a total energy minimization procedure [219]. Atomic relaxation within the hexagonal unit cells plays an important role in

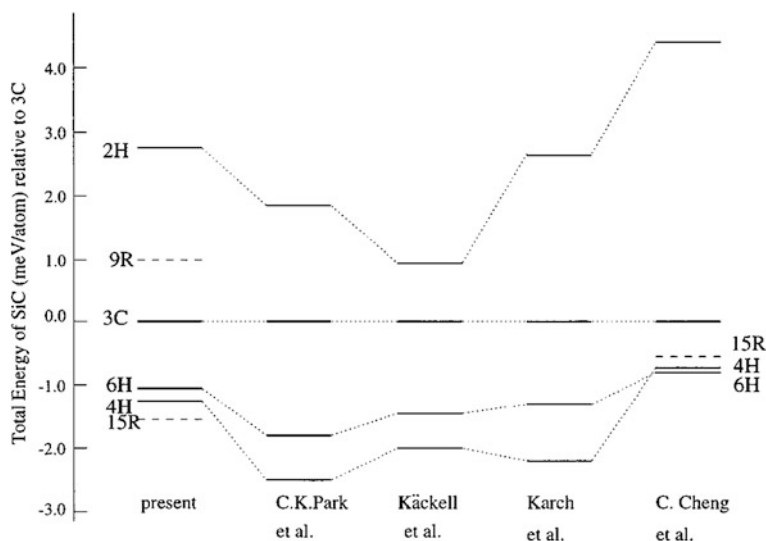


Fig. 2.103 Total energy differences among the various polytypes of SiC calculated by different groups. Reprinted with permission from [220]. Copyright 1998, American Physical Society

yielding the correct structural properties. Calculations using unrelaxed and relaxed geometries give rise to distinct orders of cohesive energies versus percentage of hexagonality in SiC structures. Calculation based on the relaxed structures yields similar results to those in Ref. [28]. The largest difference between the cohesive energies is 3 meV/atom, and the differences in the cohesive energies of different SiC polytypes are smaller than the thermal energies under reasonable crystal growth conditions. Therefore, nonequilibrium effects related to the details of the growth and effects of the vibrating lattice are proposed to be the major forces, driving polytypism during growth of SiC crystals. The zero-temperature total energy differences between more polytypes of SiC (3C, 6H, 4H, 2H, 15R, and 9R) are determined by well-converged all-electron density functional calculation [220]. The order of total energies for different polytypes is consistent with previous calculated results, and the results obtained by different groups are summarized in Fig. 2.103, and these different groups of data show qualitative agreement. The total energies of a variety of silicon carbide polytypes are calculated using the nonorthogonal tight-binding method [221]. The energies of the polytypes computed with up to 62 atoms per unit cell show that the hexagonal wurtzite structure has the highest energy and the 4H structure has the smallest energy while the cubic zinc-blende structure has intermediate energy.

Since the total energy varies only slightly among different polytypes of silicon carbide, as indicated by the aforementioned theoretical calculations, the polytypic transformation between different polytypes takes place relatively readily under various conditions. Synthesis of silicon carbide from silica and carbon as well as silicon and carbon under different conditions is investigated [222]. The primary

synthesized SiC is always β -SiC that can be formed at as low as 525 °C when carbon and silicon are contained in a low melting alloy of aluminum and zinc. β -SiC is stable up to 2,100 °C and starts to morph into α -SiC slowly and monotropically at 2,100 °C until completion at 2,400 °C. The 3C-SiC single crystals in an argon atmosphere transform into 6H-SiC at temperature above 2,150 °C [223]. Raman scattering is performed to determine the spatial distribution and depth profile of the phase-transformed 6H-SiC region in the annealed cubic samples. The phase transformation is explained by the displacement of the atomic double layers. Cubic silicon carbide crystals transform partially into the noncubic stacking sequence at 1,400 °C [224]. The 2H-SiC crystals undergo phase transformation at temperature as low as 400 °C, some form a structure with one-dimensional disorder along the crystal c -axis and others become the faulted cubic/6H structure. Dislocations significantly enhance this transformation that takes place through a slip process perpendicular to the c -axis. The β to α transformation in conventionally sintered, hot-pressed, and reaction-sintered polycrystalline SiC has been studied. Optical and transmission electron microscopies reveal that the transformation takes place via the rapid growth of composite grains comprising α -SiC plates sandwiched between recrystallized β -SiC envelopes [225]. Growth of these composite grains into the fine-grained β matrix occurs more quickly than thickening of the α plates into the β envelopes. The composite plates are formed by the extreme anisotropy of the interfacial energy between the two polytypes of SiC. That is, the $(111)_{\beta}|| (0001)_{\alpha}$ interfaces have energies several orders of magnitude smaller than the random β/α interfaces [226]. The interface between the β and α regions of partially transformed grains always contains thin α lamellae adjacent and parallel to coherent β twins or at stacking faults [227]. These planar defects are nucleation sites for the transformation and growth of the α phase results from the motion of partial dislocations nucleated at the intersection of coherent and incoherent twin boundaries. However, the initial stages of the β to α transformation have a different mechanism, dominated by elimination of high-energy β/α interfaces [228]. The phase transformation from β to α SiC in sintered SiC shows a dependence on the initial β ratio and sintering atmosphere [229]. The transformation rate decreases with increasing initial β ratio in the starting powder and in the presence of nitrogen. No transformation occurs for the initial pure β -SiC powders with 10.34 wt% Y_2O_3 and 2.95 wt% AlN as additives. The materials without phase transformation have a homogeneous microstructure with equiaxed grains. In contrast, the SiC powders with a large initial α/β ratio experience phase transformation containing elongated grains.

The α -to- β transformation in silicon carbide has been observed, although the latter may have a little higher total energy. On account of Si enrichment on the 6H-SiC (0001) surfaces during the formation of the $\sqrt{3} \times \sqrt{3}$ $R30^\circ$ reconstructed phase, a cubic stacking sequence appears at the surface [230]. LEED crystallography shows that the ultimate reconstructed surface consists of Si adatoms in T_4 sites and STM discloses mesa-like structures with various atomic periodicities before the formation of the $\sqrt{3} \times \sqrt{3}$ $R30^\circ$ phase. This Si-enriched state provides

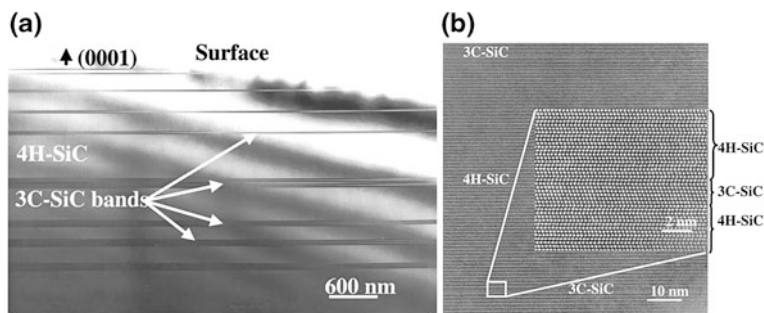
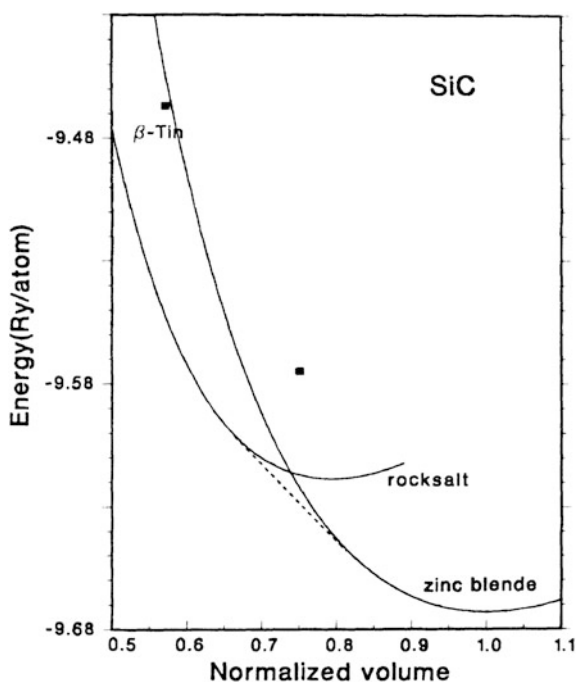


Fig. 2.104 **a** Cross-sectional TEM image of the oxidized 4H-SiC epilayer. The 3C-SiC bands are parallel to the 8° -tilted basal plane. **b** HRTEM image of 4H-SiC and 3C-SiC within a band showing two 3C-SiC sub-bands spaced by 4H-SiC. Higher magnification image in the *inset* indicates that this 3C-SiC sub-band is composed of seven Si-C bilayers. Reprinted with permission from [231]. Copyright 2001, AIP Publishing LLC

atoms for the formation of the modified stacking sequence. Dry thermal oxidation of a highly doped ($1.7 \times 10^{19} \text{ cm}^{-3}$) *n*-type 4H-SiC epilayer induces the formation of single and multiple stacking faults, which sometimes give rise to 3C-SiC bands [231]. The single stacking faults and bands of 3C-SiC in a 4H-SiC matrix in the oxidized 4H-SiC epilayer are observed by transmission electron microscopy (Fig. 2.104). These bands are parallel to the 4H-SiC(0001) basal plane but the unoxidized control sample does not show the bands. The cathodoluminescence spectrum (at 300 K) obtained from the oxidized materials shows a new peak at 2.5 eV in addition to the 3.22 eV one belonging to 4H-SiC. This 2.5 eV peak is absent from the sample without oxidation indicating its origin of stacking faults. The motion of Shockley partial dislocations on the parallel (0001) slip planes is supposed to be responsible for the polytypic transformation. The appearance and displacement of the partials are suggested to be caused by stresses induced by the heavy doping in the epilayer or nucleation from defects. However, a study of the 4H-SiC *p-i-n* diodes by emission microscopy and TEM indicates that the properties of the partial dislocations and stacking fault expansion are inconsistent with stress as the driving force [102]. The thermodynamic free-energy difference between the perfect and faulted structures is suggested to be the driving force in the diodes, implying that the hexagonal polytypes of SiC are metastable at room temperature and would transform to a faulted structure when the activation energy of the partial dislocation slip is achieved. The electron-hole recombination during operation of the diodes may offer this activation energy. Calculation predicts that 4H is the most stable polytype at least among 3C, 2H, 4H, 6H, and 15R polytypes, but the energy differences among them are so small that 4H may also convert to other polytypes under certain conditions.

At high pressure, silicon carbide crystals may morph into the rock salt-type structure. The high-pressure properties of SiC are calculated by the *ab initio* pseudopotential method [232]. Figure 2.105 displays the calculated total energies of the zinc-blende, rock salt, and β -Sn structures of silicon carbide. The zinc-blende

Fig. 2.105 Calculated crystal total energy as a function of volume normalized to the calculated equilibrium volume of 1.0369 nm^3 per atom of the zinc-blende phase of SiC. The dashed line denotes the common tangent of the two curves and solid squares are the energies of the β -Sn phase. Reprinted with permission from [232]. Copyright 1987, American Physical Society



structure is stable up to 660 kbar, above which it transforms into the rock salt phase. The rock salt structure of SiC is more stable than the β -Sn structure. Other possible phases like the B-8 structure are not calculated, and therefore, the calculated threshold transition pressure represents only an upper limit for the transition pressure from zinc-blende to another structure. The calculation also indicates that the indirect bandgap of cubic SiC decreases with increasing pressure. This tendency is similar to that of silicon but not diamond. X-ray diffraction is employed to study the 3C and 6H polytypes of SiC at pressures up to 105 and 95 GPa, respectively [233]. 3C-SiC undergoes phase transition into the rock salt phase at above 100 GPa together with a volume reduction of 20.3 %, whereas 6H-SiC remains stable up to the highest applied pressure but exhibits a premonition of phase transition above 90 GPa. The ab initio density functional theory is also applicable to the determination of the ultrahigh pressure dependence of materials. The pressure-dependent properties of cubic and hexagonal polytypes of SiC are calculated based on the density functional theory using the plane-wave pseudopotential approach [234]. NaCl, NiAs, CsCl, and β -Sn structures of SiC are considered as potential high-pressure phases and the calculation predicts a pressure-induced phase transition from zinc-blende to rock salt at a critical pressure of 0.67 Mbar. However, the calculated transition pressure is lower than the experimental value. The high-pressure transition to the NaCl structure is predicted for 3C-, 2H-, and 4H-SiC.

Isothermal-isobaric molecular dynamics simulation is performed to investigate the pressure-induced structural transformation in SiC [235]. The simulation

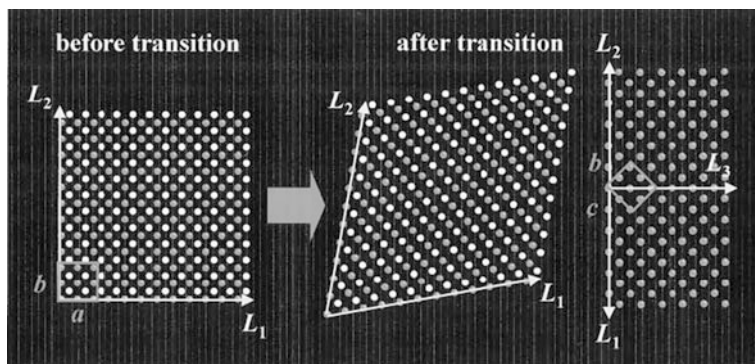


Fig. 2.106 Average atom positions in the molecular dynamics cell prior to and after the zinc-blende to rock salt transition in silicon carbide. The *gray* and *white* balls separately mark the positions of the silicon and carbon atoms. The *square box* shows the unit cell of each structure. Reprinted with permission from [235]. Copyright 2000, American Physical Society

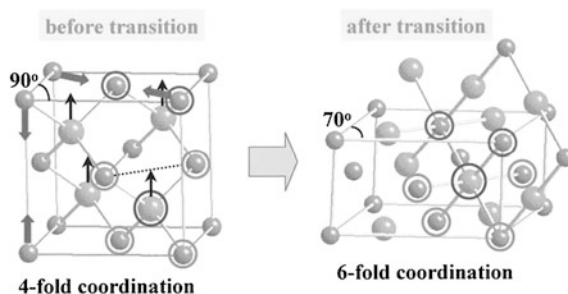


Fig. 2.107 Schematic of mechanism of the SiC phase transformation from the zinc-blende structure to rock salt structure. The *big* and *small* balls show separately the positions of the silicon and carbon atoms. The *arrows* mark the directions along which the atoms move during the phase transformation. Reprinted with permission from [235]. Copyright 2000, American Physical Society

reproduces the reversible transformation between the fourfold coordinated zinc-blende structure and sixfold coordinated rock salt structure. The molecular dynamics cell of the system changes from cubic to monoclinic after the onset of phase transformation from zinc-blende to rock salt (Fig. 2.106). During the cubic-to-monoclinic conversion, the silicon and carbon sublattices shift relatively to each other along the (100) direction in the zinc-blende structure (Fig. 2.107). This direction is the (110) direction in the resultant rock salt structure. The calculated volume changes at the transition and hysteresis agree well with the experimental values. A unified mechanism of high-pressure transformation of the various tetrahedrally bonded polytypes of SiC to the rock salt structure is proposed [236]. It involves several strains and intersublattice motions. Calculation of the energy barriers associated with these transition paths using first-principle pseudopotential method indicates that the 3C transition has a lower enthalpy barrier than the other

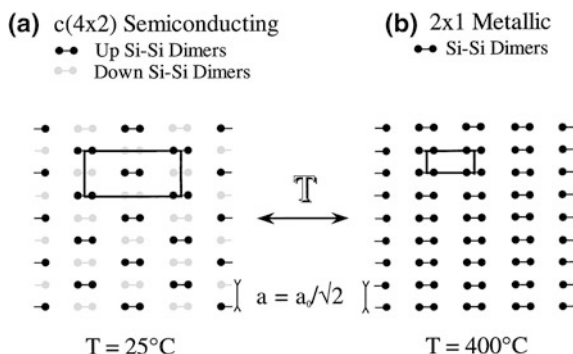


Fig. 2.108 Schematic of the reversible 3C-SiC(100) surface phase transition from a semiconducting $c(4 \times 2)$ reconstruction with alternatively up and down dimmers to a (2×1) metallic reconstruction with all dimers of the same height. The surface unit cells are marked. Reprinted with permission from [238]. Copyright 1997, American Physical Society

polytypes at pressure above the equilibrium transition pressure. Using the proposed effective interatomic interaction potential for SiC, molecular dynamics simulation gives rise to the structural energies in several SiC polytypes [237]. The cubic structure has the lowest energy, followed by the wurtzite and rock salt structures. The pressure for the 3C-to-rock salt transformation from the common tangent is derived to be 90 GPa.

By means of variable temperature scanning tunneling microscopy and angle-resolved photoemission spectroscopy, the transition between two β -SiC(100) surface structures has been observed [238]. There is a reversible temperature-dependent phase transition from a semiconducting $c(4 \times 2)$ surface at 25°C to a metallic (2×1) structure at 400°C (Fig. 2.108). This transition stems from the temperature-induced disruption of the $c(4 \times 2)$ structure composed of alternately up and down dimmers into the (2×1) structure with all dimers of the same height. This (2×1) structure gives rise to electronic orbital overlap between the top surface Si atoms leading to surface metallization.

References

1. Harris GL (ed) (1995) Properties of silicon carbide. INSPEC, London
2. Sadow SE, Agarwal A (eds) (2004) Advances in silicon carbide processing and applications. Artech House, Norwood
3. Shur M, Rummyantsev S, Levinshtein M (eds) (2006/2007) SiC materials and devices (vols 1 and 2). World Scientific, Singapore
4. Nicolussi GK, Davis AM, Pellin MJ, Lewis RS, Clayton RN, Amari S (1997) s-Process zirconium in presolar silicon carbide grains. *Science* 277:1281–1283
5. Huss GR, Lewis RS (1995) Presolar diamond, SiC, and graphite in primitive chondrites: abundances as a function of meteorite class and petrologic type. *Geochim Cosmochim Acta* 59:115–160

6. Huss GR, Meshik AP, Smith JB, Hohenberg CM (2003) Presolar diamond, silicon carbide, and graphite in carbonaceous chondrites: implications for thermal processing in the solar nebula. *Geochim Cosmochim Acta* 67:4823–4848
7. Nicolussi GK, Pellin MJ, Lewis RS, Davis AM, Clayton RN, Amari S (1998) Strontium isotopic composition in individual circumstellar silicon carbide grains: a record of *s*-process nucleosynthesis. *Phys Rev Lett* 81:3583–3586
8. Daulton TL, Bernatowicz TJ, Lewis RS, Messenger S, Stadermann FJ, Amari S (2002) Polytype distribution in circumstellar silicon carbide. *Science* 296:1852–1855
9. Gallino R, Raiteri CM, Busso M (1993) Carbon stars and isotopic Ba anomalies in meteoritic SiC grains. *Astrophys J* 410:400–411
10. Hoppe P, Amari S, Zinner E, Ireland T, Lewis RS (1994) Carbon, nitrogen, magnesium, silicon, and titanium isotopic compositions of single interstellar silicon carbide grains from the Murchison carbonaceous chondrite. *Astrophys J* 430:870–890
11. Amari S, Nittler LR, Zinner E, Lodders K, Lewis RS (2001) Presolar SiC grains of type A and B: their isotopic compositions and stellar origins. *Astrophys J* 559:463–483
12. Lugaro M, Davis AM, Gallino R, Pellin MJ, Straniero O, Käppeler F (2003) Isotopic compositions of strontium, zirconium, molybdenum, and barium in single presolar SiC grains and asymptotic giant branch stars. *Astrophys J* 593:486–508
13. Clément D, Mutschke H, Klein R, Henning Th (2003) New laboratory spectra of isolated β -SiC nanoparticles: comparison with spectra taken by the *Infrared Space Observatory*. *Astrophys J* 594:642–650
14. Speck AK, Barlow MJ, Skinner CJ (1997) The nature of the silicon carbide in carbon star outflows. *Mon Not R Astron Soc* 288:431–456
15. Amari S, Hoppe P, Zinner E, Lewis RS (1992) Interstellar SiC with unusual isotopic compositions: grains from a supernova. *Astrophys J* 394:L43–L46
16. Nittler LR, Amari S, Zinner E, Woosley SE, Lewis RS (1996) Extinct ^{44}Ti in presolar graphite and SiC: proof of a supernova origin. *Astrophys J* 462:L31–L34
17. Hoppe P, Strebel R, Eberhardt P, Amari S, Lewis RS (1996) Small SiC grains and a nitride grain of circumstellar origin from the Murchison meteorite: implications for stellar evolution and nucleosynthesis. *Geochim Cosmochim Acta* 60:883–907
18. Clayton DD, Arnett D, Kane J, Meyer BS (1997) Type X silicon carbide presolar grains: type Ia supernova condensates. *Astrophys J* 486:824–834
19. Junginger HG, van Haeringen W (1970) Energy band structures of four polytypes of silicon carbide calculated with the empirical pseudopotential method. *Phys Stat Sol* 37:709–719
20. Hemstreet LA Jr, Fong CY (1972) Electronic band structure and optical properties of 3C-SiC, BP, and BN. *Phys Rev B* 6:1464–1480
21. Choyke WJ, Hamilton DR, Patrick L (1964) Optical properties of cubic SiC: luminescence of nitrogen-exciton complexes, and interband absorption. *Phys Rev* 133:A1163–A1166
22. Backes WH, Bobbert PA, van Haeringen W (1994) Energy-band structure of SiC polytypes by interface matching of electronic wave functions. *Phys Rev B* 49:7564–7568
23. Lubinsky AR, Ellis DE, Painter GS (1975) Electronic structure and optical properties of 3C-SiC. *Phys Rev B* 11:1537–1546
24. Rohlfling M, Krüger P, Pollmann J (1993) Quasiparticle band-structure calculations for C, Si, Ge, GaAs, and SiC using Gaussian-orbital basis sets. *Phys Rev B* 48:17791–17805
25. Käckell P, Wenzien B, Bechstedt F (1994) Electronic properties of cubic and hexagonal SiC polytypes from *ab initio* calculations. *Phys Rev B* 50:10761–10768
26. Persson C, Lindefelt U (1996) Detailed band structure for 3C-, 2H-, 4H-, 6H-SiC, and Si around the fundamental band gap. *Phys Rev B* 54:10257–10260
27. Persson C, Lindefelt U (1997) Relativistic band structure calculation of cubic and hexagonal SiC polytypes. *J Appl Phys* 82:5496–5508
28. Park CH, Cheong B-H, Lee K-H, Chang KJ (1994) Structural and electronic properties of cubic, 2H, 4H, and 6H SiC. *Phys Rev B* 49:4485–4493
29. Wenzien B, Käckell P, Bechstedt F, Cappellini G (1995) Quasiparticle band structure of silicon carbide polytypes. *Phys Rev B* 52:10897–10905

30. Lambrecht WRL, Limpijumrong S, Rashkeev SN, Segall B (1997) Electronic band structure of SiC polytypes: a discussion of theory and experiment. *Phys Stat Sol (b)* 202:5–33
31. Dalibor T, Pensl G, Matsunami H, Kimoto T, Choyke WJ, Schöner A, Nordell N (1997) Deep defect centers in silicon carbide monitored with deep level transient spectroscopy. *Phys Stat Sol (a)* 162:199–225
32. Itoh H, Hayakawa N, Nashiyama I, Sakuma E (1989) Electron spin resonance in electron-irradiated 3C-SiC. *J Appl Phys* 66:4529–4531
33. Itoh H, Yoshikawa M, Nashiyama I, Okumura H, Misawa S, Yoshida S (1995) Photoluminescence of radiation induced defects in 3C-SiC epitaxially grown on Si. *J Appl Phys* 77:837–842
34. Wimbauer T, Meyer BK, Hofstaetter A, Scharmann A, Overhof H (1997) Negatively charged Si vacancy in 4H SiC: a comparison between theory and experiment. *Phys Rev B* 56:7384–7388
35. Sörman E, Son NT, Chen WM, Kordina O, Hallin C, Janzén E (2000) Silicon vacancy related defect in 4H and 6H SiC. *Phys Rev B* 61:2613–2620
36. Torpo L, Nieminen RM, Laasonen KE, Pöykkö S (1999) Silicon vacancy in SiC: a high-spin state defect. *Appl Phys Lett* 74:221–223
37. Fan J, Chu PK (2010) Group IV nanoparticles: synthesis, properties, and biological applications. *Small* 6:2080–2098
38. Kurtsiefer C, Mayer S, Zarda P, Weinfurter H (2000) Stable solid-state source of single photons. *Phys Rev Lett* 85:290–293
39. Mizuochi N, Makino T, Kato H, Takeuchi D, Ogura M, Okushi H, Nothhaft M, Neumann P, Gali A, Jelezko F, Wrachtrup J, Yamasaki S (2012) Electrically driven single-photon source at room temperature in diamond. *Nat Photonics* 6:299–303
40. Baranov PG, Bundakova AP, Soltamova AA, Orlinskii SB, Borovykh IV, Zondervan R, Verberk R, Schmidt J (2011) Silicon vacancy in SiC as a promising quantum system for single-defect and single-photon spectroscopy. *Phys Rev B* 83:125203
41. Soltamov VA, Soltamova AA, Baranov PG, Proskuryakov II (2012) Room temperature coherent spin alignment of silicon vacancies in 4H- and 6H-SiC. *Phys Rev Lett* 108:226402
42. Son NT, Hai PN, Janzén E (2001) Carbon vacancy-related defect in 4H and 6H SiC. *Phys Rev B* 63:201201(R)
43. Danno K, Kimoto T (2006) Investigation of deep levels in n-type 4H-SiC epilayers irradiated with low-energy electrons. *J Appl Phys* 100:113728
44. Eberlein TAG, Jones R, Briddon PR (2003) Z_1/Z_2 defects in 4H-SiC. *Phys Rev Lett* 90:225502
45. Dannefaer S, Craigen D, Kerr D (1995) Carbon and silicon vacancies in electron-irradiated 6H-SiC. *Phys Rev B* 51:1928–1930
46. Aboelfotoh MO, Doyle JP (1999) Defect energy levels in electron-irradiated and deuterium-implanted 6H silicon carbide. *Phys Rev B* 59:10823–10829
47. Zywiez A, Furthmüller J, Bechstedt F (1999) Vacancies in SiC: influence of Jahn-Teller distortions, spin effects, and crystal structure. *Phys Rev B* 59:15166–15180
48. Choyke J, Patrick L (1971) Photoluminescence of radiation defects in cubic SiC: localized modes and Jahn-Teller effect. *Phys Rev B* 4:1843–1847
49. Patrick L, Choyke J (1972) Photoluminescence of radiation defects in ion-implanted 6H SiC. *Phys Rev B* 5:3253–3259
50. Haberstroh Ch, Helbig R, Stein RA (1994) Some new features of the photoluminescence of SiC(6H), SiC(4H), and SiC(15R). *J Appl Phys* 76:509–513
51. Hemmingsson CG, Son NT, Ellison A, Zhang J, Janzén E (1998) Negative-U centers in 4H silicon carbide. *Phys Rev B* 58:R10119–R10122
52. Son NT, Carlsson P, ul Hassan J, Janzén E, Umeda T, Isoya J, Gali A, Bockstedte M, Morishita N, Ohshima T, Itoh H (2006) Divacancy in 4H-SiC. *Phys Rev Lett* 96:055501
53. Torpo L, Staab TEM, Nieminen RM (2002) Divacancy in 3C- and 4H-SiC: an extremely stable defect. *Phys Rev B* 65:085202

54. Koehl WF, Buckley BB, Heremans FJ, Calusine G, Awschalom DD (2011) Room temperature coherent control of defect spin qubits in silicon carbide. *Nature* 479:84–88
55. Falk AL, Buckley BB, Calusine G, Koehl WF, Dobrovitski VV, Politi A, Zorman CA, Feng PX-L, Awschalom DD (2013) Polytype control of spin qubits in silicon carbide. *Nat Commun* 4:1819
56. Kawasuso A, Itoh H, Okada S, Okumura H (1996) Annealing processes of vacancy-type defects in electron-irradiated and as-grown 6H-SiC studied by positron lifetime spectroscopy. *J Appl Phys* 80:5639–5645
57. Hiyoshi T, Kimoto T (2009) Elimination of the major deep levels in n- and p-Type 4H-SiC by two-step thermal treatment. *Appl Phys Exp* 2:091101
58. Nagesh V, Farmer JW, Davis RF, Kong HS (1987) Defects in neutron irradiated SiC. *Appl Phys Lett* 50:1138–1140
59. Torpo L, Pöykkö S, Nieminen RM (1998) Antisites in silicon carbide. *Phys Rev B* 57:6243–6246
60. Egilsson T, Henry A, Ivanov IG, Lindström JL, Janzén E (1999) Photoluminescence of electron-irradiated 4H-SiC. *Phys Rev B* 59:8008–8014
61. Eberlein TAG, Fall CJ, Jones R, Briddon PR, Öberg S (2002) Alphabet luminescence lines in 4H-SiC. *Phys Rev B* 65:184108
62. Gali A, Deák P, Rauls E, Son NT, Ivanov IG, Carlsson FHC, Janzén E, Choyke WJ (2003) Correlation between the antisite pair and the D_1 center in SiC. *Phys Rev B* 67:155203
63. Eberlein TAG, Jones R, Öberg S, Briddon PR (2006) Density functional theory calculation of the D_1 optical center in SiC. *Phys Rev B* 74:144106
64. Patrick L, Choyke WJ (1973) Localized vibrational modes of a persistent defect in ion-implanted SiC. *J Phys Chem Solids* 34:565
65. Freitas JA, Bishop SG, Edmond JA, Ryu J, Davis RF (1987) Photoluminescence spectroscopy of ion-implanted 3C-SiC grown by chemical vapor deposition. *J Appl Phys* 61:2011–2016
66. Mattausch A, Bockstedte M, Pankratov O (2004) Carbon antisite clusters in SiC: a possible pathway to the D_{II} center. *Phys Rev B* 69:045322
67. Lingner Th, Greulich-Weber S, Spaeth J-M, Gerstmann U, Rauls E, Hajnal Z, Frauenheim Th, Overhof H (2001) Structure of the silicon vacancy in 6H-SiC after annealing identified as the carbon vacancy–carbon antisite pair. *Phys Rev B* 64:245212
68. Umeda T, Son NT, Isoya J, Janzén E, Ohshima T, Morishita N, Itoh H, Gali A, Bockstedte M (2006) Identification of the carbon antisite-vacancy pair in 4H-SiC. *Phys Rev Lett* 96:145501
69. Steeds JW (2009) Photoluminescence study of the carbon antisite-vacancy pair in 4H- and 6H-SiC. *Phys Rev B* 80:245202
70. Castelletto S, Johnson BC, Ivády V, Stavrias N, Umeda T, Gali A, Ohshima T (2014) A silicon carbide room-temperature single-photon source. *Nat Mater* 13:151–156
71. Wang C, Bernholc J, Davis RF (1988) Formation energies, abundances, and the electronic structure of native defects in cubic SiC. *Phys Rev B* 38:12752–12755
72. Torpo L, Marlo M, Staab TEM, Nieminen RM (2001) Comprehensive *ab initio* study of properties of monovacancies and antisites in 4H-SiC. *J Phys: Condens Matter* 13:6203–6231
73. Storasta L, Bergman JP, Janzén E, Henry A, Lu J (2004) Deep levels created by low energy electron irradiation in 4H-SiC. *J Appl Phys* 96:4909–4915
74. Devanathan R, Weber WJ, Gao F (2001) Atomic scale simulation of defect production in irradiated 3C-SiC. *J Appl Phys* 90:2303–2309
75. Gao F, Bylaska EJ, Weber WJ, Corrales LR (2001) *Ab initio* and empirical-potential studies of defect properties in 3C-SiC. *Phys Rev B* 64:245208
76. Gao F, Weber WJ, Posselt M, Belko V (2004) Atomistic study of intrinsic defect migration in 3C-SiC. *Phys Rev B* 69:245205
77. Bockstedte M, Mattausch A, Pankratov O (2003) *Ab initio* study of the migration of intrinsic defects in 3C-SiC. *Phys Rev B* 68:205201

78. Bockstedte M, Mattausch A, Pankratov O (2004) *Ab initio* study of the annealing of vacancies and interstitials in cubic SiC: vacancy-interstitial recombination and aggregation of carbon interstitials. *Phys Rev B* 69:235202
79. Gali A, Deák P, Ordejón P, Son NT, Janzén E, Choyke WJ (2003) Aggregation of carbon interstitials in silicon carbide: a theoretical study. *Phys Rev B* 68:125201
80. Rauls E, Frauenheim Th, Gali A, Deák P (2003) Theoretical study of vacancy diffusion and vacancy-assisted clustering of antisites in SiC. *Phys Rev B* 68:155208
81. Amelinckx S, Strumane G, Webb WW (1960) Dislocations in silicon carbide. *J Appl Phys* 31:1359–1370
82. Ha S, Mieszkowski P, Skowronski M, Rowland LB (2002) Dislocation conversion in 4H silicon carbide epitaxy. *J Cryst Growth* 244:257–266
83. Blumenau AT, Fall CJ, Jones R, Öberg S, Frauenheim T, Briddon PR (2003) Structure and motion of basal dislocations in silicon carbide. *Phys Rev B* 68:174108
84. Heindl J, Strunk HP, Heydemann VD, Pensl G (1997) Micropipes: hollow tubes in silicon carbide. *Phys Stat Sol (a)* 162:251–262
85. Neudeck PG, Powell JA (1994) Performance limiting micropipe defects in silicon carbide wafers. *IEEE Electron Device Lett* 15:63–65
86. Heindl J, Dorsch W, Strunk HP, Müller G, Eckstein R, Hofmann D, Winnacker A (1998) Dislocation content of micropipes in SiC. *Phys Rev Lett* 80:740–741
87. Pirouz P (1998) On micropipes and nanopipes in SiC and GaN. *Philos Mag* 78:727–736
88. Dudley M, Huang XR, Huang W, Powell A, Wang S, Neudeck P, Skowronski M (1999) The mechanism of micropipe nucleation at inclusions in silicon carbide. *Appl Phys Lett* 75:784–786
89. Huang XR, Dudley M, Vetter WM, Huang W, Wang S, Carter CH (1999) Direct evidence of micropipe-related pure superscrew dislocations in SiC. *Appl Phys Lett* 74:353–355
90. Stevens R (1972) Defects in silicon carbide. *J Mater Sci* 7:517–521
91. Koumoto K, Takeda S, Pai CH, Sato T, Yanagida H (1989) High-resolution electron microscopy observations of stacking faults in β -SiC. *J Am Ceram Soc* 72:1985–1987
92. Pujar VV, Cawley JD (1995) Effects of stacking faults on the X-ray diffraction profiles of β -SiC powders. *J Am Ceram Soc* 78:774–782
93. Hong MH, Samant AV, Pirouz P (2000) Stacking fault energy of 6H-SiC and 4H-SiC single crystals. *Philos Mag* 80:919–935
94. Liu JQ, Skowronski M, Hallin C, Söderholm R, Lendenmann H (2002) Structure of recombination-induced stacking faults in high-voltage SiC p-n junctions. *Appl Phys Lett* 80:749–751
95. Twigg ME, Stahlbush RE, Fatemi M, Arthur SD, Fedison JB, Tucker JB, Wang S (2003) Structure of stacking faults formed during the forward bias of 4H-SiC *p-i-n* diodes. *Appl Phys Lett* 82:2410–2412
96. Jacobson H, Bergman JP, Hallin C, Janzén E, Tuomi T, Lendenmann H (2004) Properties and origins of different stacking faults that cause degradation in SiC PiN diodes. *J Appl Phys* 95:1485–1488
97. Izumi S, Tsuchida H, Kamata I, Tawara T (2005) Structural analysis and reduction of in-grown stacking faults in 4H-SiC epilayers. *Appl Phys Lett* 86:202108
98. Fujiwara H, Kimoto T, Tojo T, Matsunami H (2005) Characterization of in-grown stacking faults in 4H-SiC (0001) epitaxial layers and its impacts on high-voltage Schottky barrier diodes. *Appl Phys Lett* 87:051912
99. Feng G, Suda J, Kimoto T (2008) Characterization of stacking faults in 4H-SiC epilayers by room-temperature microphotoluminescence mapping. *Appl Phys Lett* 92:221906
100. Liu JQ, Chung HJ, Kuhr T, Li Q, Skowronski M (2002) Structural instability of 4H-SiC polytype induced by n-type doping. *Appl Phys Lett* 80:2111–2113
101. Kuhr TA, Liu JQ, Chung HJ, Skowronski M, Szmulowicz F (2002) Spontaneous formation of stacking faults in highly doped 4H-SiC during annealing. *J Appl Phys* 92:5863–5871
102. Ha S, Skowronski M, Sumakeris JJ, Paisley MJ, Das MK (2004) Driving force of stacking-fault formation in SiC *p-i-n* diodes. *Phys Rev Lett* 92:175504

103. Galeckas A, Linnros J, Pirouz P (2006) Recombination-induced stacking faults: evidence for a general mechanism in hexagonal SiC. *Phys Rev Lett* 96:025502
104. Sridhara SG, Carlsson FHC, Bergman JP, Janzén E (2001) Luminescence from stacking faults in 4H SiC. *Appl Phys Lett* 79:3944–3946
105. Fissel A, Kaiser U, Schröter B, Richter W, Bechstedt F (2001) MBE growth and properties of SiC multi-quantum well structures. *Appl Surf Sci* 184:37–42
106. Bai S, Devaty RP, Choyke WJ, Kaiser U, Wagner G, MacMillan MF (2003) Determination of the electric field in 4H/3C/4H-SiC quantum wells due to spontaneous polarization in the 4H SiC matrix. *Appl Phys Lett* 83:3171–3173
107. Ding Y, Park K-B, Pelz JP, Palle KC, Mikhov MK, Skromme BJ, Meidia H, Mahajan S (2004) Quantum well state of self-forming 3C-SiC inclusions in 4H SiC determined by ballistic electron emission microscopy. *Phys Rev B* 69:041305(R)
108. Galeckas A, Hallén A, Majdi S, Linnros J, Pirouz P (2006) Combined photoluminescence-imaging and deep-level transient spectroscopy of recombination processes at stacking faults in 4H-SiC. *Phys Rev B* 74:233203
109. Miao MS, Limpijumngong S, Lambrecht WRL (2001) Stacking fault band structure in 4H-SiC and its impact on electronic devices. *Appl Phys Lett* 79:4360–4362
110. Lambrecht WRL, Miao MS (2006) Electronic driving force for stacking fault expansion in 4H-SiC. *Phys Rev B* 73:155312
111. Iwata H, Lindefelt U, Öberg S, Briddon PR (2001) Localized electronic states around stacking faults in silicon carbide. *Phys Rev B* 65:033203
112. Lindefelt U, Iwata H, Öberg S, Briddon PR (2003) Stacking faults in 3C-, 4H-, and 6H-SiC polytypes investigated by an *ab initio* supercell method. *Phys Rev B* 67:155204
113. Iwata H, Lindefelt U, Öberg S, Briddon PR (2003) Cubic polytype inclusions in 4H-SiC. *J Appl Phys* 93:1577–1585
114. Woodbury HH, Ludwig GW (1961) Electron spin resonance studies in SiC. *Phys Rev* 124:1083–1089
115. Suttrop W, Pensl G, Choyke WJ, Stein R, Leibenzeder S (1992) Hall effect and infrared absorption measurements on nitrogen donors in 6H-silicon carbide. *J Appl Phys* 72:3708–3713
116. Götz W, Schöner A, Pensl G, Suttrop W, Choyke WJ, Stein R, Leibenzeder S (1993) Nitrogen donors in 4H-silicon carbide. *J Appl Phys* 73:3332–3338
117. Schneider J, Müller HD, Maier K, Wilkening W, Fuchs F, Dörnen A, Leibenzeder S, Stein R (1990) Infrared spectra and electron spin resonance of vanadium deep level impurities in silicon carbide. *Appl Phys Lett* 56:1184–1186
118. Choyke WJ, Devaty RP, Clemen LL, Yoganathan M, Pensl G, Hässler Ch (1994) Intense erbium-1.54- μ m photoluminescence from 2 to 525 K in ion-implanted 4H, 6H, 15R, and 3C SiC. *Appl Phys Lett* 65:1668–1670
119. Aradi B, Gali A, Deák P, Lowther JE, Son NT, Janzén E, Choyke WJ (2001) *Ab initio* density-functional supercell calculations of hydrogen defects in cubic SiC. *Phys Rev B* 63:245202
120. Greulich-Weber S (1997) EPR and ENDOR investigations of shallow impurities in SiC polytypes. *Phys Stat Sol (a)* 162:95–151
121. Vetelino JF, Mitra SS (1969) Lattice dynamics of cubic SiC. *Phys Rev* 178:1349–1352
122. Feldman DW, Parker JH, Choyke WJ, Patrick L (1968) Raman scattering in 6H SiC. *Phys Rev* 170:698–704
123. Feldman DW, Parker JH, Choyke WJ, Patrick L (1968) Phonon dispersion curves by Raman scattering in SiC, polytypes 3C, 4H, 6H, 15R, and 21R. *Phys Rev* 173:787–793
124. Hofmann M, Zywiets A, Karch K, Bechstedt F (1994) Lattice dynamics of SiC polytypes within the bond-charge model. *Phys Rev B* 50:13401–13411
125. Karch K, Pavone P, Windl W, Schütt O, Strauch D (1994) *Ab initio* calculation of structural and lattice-dynamical properties of silicon carbide. *Phys Rev B* 50:17054–17063
126. Spitzer WG, Kleinman D, Walsh D (1959) Infrared properties of hexagonal silicon carbide. *Phys Rev* 113:127–132

127. Spitzer WG, Kleinman DA, Frosch CJ (1959) Infrared properties of cubic silicon carbide films. *Phys Rev* 113:133–136
128. Patrick L, Choyke WJ (1961) Lattice absorption bands in SiC. *Phys Rev* 123:813–815
129. Holm RT, Klein PH, Nordquist PER (1986) Infrared reflectance evaluation of chemically vapor deposited β -SiC films grown on Si substrates. *J Appl Phys* 60:1479–1485
130. Engelbrecht F, Helbig R (1993) Effect of crystal anisotropy on the infrared reflectivity of 6H-SiC. *Phys Rev B* 48:15698–15707
131. Tiwald TE, Woollam JA, Zollner S, Christiansen J, Gregory RB, Wetteroth T, Wilson SR, Powell AR (1999) Carrier concentration and lattice absorption in bulk and epitaxial silicon carbide determined using infrared ellipsometry. *Phys Rev B* 60:11464–11474
132. Nakashima S, Katahama H, Nakakura Y, Mitsuishi A (1986) Relative Raman intensities of the folded modes in SiC polytypes. *Phys Rev B* 33:5721–5729
133. Okumura H, Sakuma E, Lee JH, Mukaida H, Misawa S, Endo K, Yoshida S (1987) Raman scattering of SiC: application to the identification of heteroepitaxy of SiC polytypes. *J Appl Phys* 61:1134–1136
134. Nakashima S, Tahara K (1989) Raman scattering determination of structures for SiC polytypes: quantitative evaluation with a revised model of lattice dynamics. *Phys Rev B* 40:6339–6344
135. Burton JC, Sun L, Long FH, Feng ZC, Ferguson IT (1999) First- and second-order Raman scattering from semi-insulating 4H-SiC. *Phys Rev B* 59:7282–7284
136. Olego D, Cardona M, Vogl P (1982) Pressure dependence of the optical phonons and transverse effective charge in 3C-SiC. *Phys Rev B* 25:3878–3888
137. Olego D, Cardona M (1982) Pressure dependence of Raman phonons of Ge and 3C-SiC. *Phys Rev B* 25:1151–1160
138. Debernardi A, Ulrich C, Syassen K, Cardona M (1999) Raman linewidths of optical phonons in 3C-SiC under pressure: first-principles calculations and experimental results. *Phys Rev B* 59:6774–6783
139. Liu J, Vohra YK (1994) Raman modes of 6H polytype of silicon carbide to ultrahigh pressures: a comparison with silicon and diamond. *Phys Rev Lett* 72:4105–4108
140. Olego D, Cardona M (1982) Temperature dependence of the optical phonons and transverse effective charge in 3C-SiC. *Phys Rev B* 25:3889–3896
141. Rohmfeld S, Hundhausen M, Ley L (1998) Raman scattering in polycrystalline 3C-SiC: influence of stacking faults. *Phys Rev B* 58:9858–9862
142. Colwell PJ, Klein MV (1972) Raman scattering from electronic excitations in *n*-type silicon carbide. *Phys Rev B* 6:498–515
143. Klein MV, Ganguly BN, Colwell PJ (1972) Theoretical and experimental study of Raman scattering from coupled LO-phonon-plasmon modes in silicon carbide. *Phys Rev B* 6:2380–2388
144. Harima H, Nakashima S, Uemura T (1995) Raman scattering from anisotropic LO-phonon-plasmon-coupled mode in *n*-type 4H- and 6H-SiC. *J Appl Phys* 78:1996–2005
145. Burton JC, Sun L, Pophristic M, Lukacs SJ, Long FH, Feng ZC, Ferguson IT (1998) Spatial characterization of doped SiC wafers by Raman spectroscopy. *J Appl Phys* 84:6268–6273
146. Choyke WJ, Patrick L (1957) Absorption of light in alpha SiC near the band edge. *Phys Rev* 105:1721–1723
147. Choyke WJ, Patrick L (1968) Higher Absorption Edges in 6H-SiC. *Phys Rev* 172:769–772
148. Sridhara SG, Devaty RP, Choyke WJ (1998) Absorption coefficient of 4H silicon carbide from 3900 to 3250 Å. *J Appl Phys* 84:2963–2964
149. Sridhara SG, Eperjesi TJ, Devaty RP, Choyke WJ (1999) Penetration depths in the ultraviolet for 4H, 6H and 3C silicon carbide at seven common laser pumping wavelengths. *Mater Sci Eng B* 61–62:229–233
150. Choyke WJ, Patrick L (1970) Luminescence of donor-acceptor pairs in cubic SiC. *Phys Rev B* 2:4959–4965
151. Hopfield JJ, Thomas DG, Gershenzon M (1963) Pair spectra in GaP. *Phys Rev Lett* 10:162–164

152. Suzuki A, Matsunami H, Tanaka T (1977) Photoluminescence due to Al, Ga, and B acceptors in 4H-, 6H-, and 3C-SiC grown from a Si melt. *J Electrochem Soc* 124:241–246
153. Ikeda M, Matsunami H, Tanaka T (1980) Site effect on the impurity levels in 4H, 6H, and 15R SiC. *Phys Rev B* 22:2842–2854
154. Hagen SH, Van Kemenade AWC, van der Does de Bye JAW (1973) Donor-acceptor pair spectra in 6H and 4H SiC doped with nitrogen and aluminium. *J Lumin* 8:18–31
155. Kamiyama S, Maeda T, Nakamura Y, Iwaya M, Amano H, Akasaki I, Kinoshita H, Furusho T, Yoshimoto M, Kimoto T, Suda J, Henry A, Ivanov IG, Bergman JP, Monemar B, Onuma T, Chichibu SF (2006) Extremely high quantum efficiency of donor-acceptor-pair emission in N-and-B-doped 6H-SiC. *J Appl Phys* 99:093108
156. Ou Y, Jokubavicius V, Kamiyama S, Liu C, Berg RW, Linnarsson M, Yakimova R, Syväjärvi M, Ou H (2011) Donor-acceptor-pair emission characterization in N-B doped fluorescent SiC. *Optic Mater Exp* 1:1439–1446
157. Lampert MA (1958) Mobile and immobile effective-mass-particle complexes in nonmetallic solids. *Phys Rev Lett* 1:450–453
158. Haynes JR (1960) Experimental proof of the existence of a new electronic complex in silicon. *Phys Rev Lett* 4:361–363
159. Choyke WJ, Patrick L (1962) Exciton recombination radiation and phonon spectrum of 6H SiC. *Phys Rev* 127:1868–1877
160. Hamilton DR, Choyke WJ, Patrick L (1963) Photoluminescence of nitrogen-exciton complexes in 6H SiC. *Phys Rev* 131:127–133
161. Patrick L, Hamilton DR, Choyke WJ (1963) Optical properties of 15R SiC: luminescence of nitrogen-exciton complexes, and interband absorption. *Phys Rev* 132:2023–2031
162. Patrick L, Choyke WJ, Hamilton DR (1965) Luminescence of 4H SiC, and location of conduction-band minima in SiC polytypes. *Phys Rev* 137:A1515–A1520
163. Patrick L, Hamilton DR, Choyke WJ (1966) Growth, luminescence, selection rules, and lattice sums of SiC with wurtzite structure. *Phys Rev* 143:526–536
164. Ivanov IG, Hallin C, Henry A, Kordina O, Janzén E (1996) Nitrogen doping concentration as determined by photoluminescence in 4H- and 6H-SiC. *J Appl Phys* 80:3504–3508
165. Dean PJ, Herbert DC, Bimberg D, Choyke WJ (1976) Donor exciton satellites in cubic silicon carbide: multiple bound excitons revisited. *Phys Rev Lett* 37:1635–1638
166. Kuwabara H, Yamada S (1975) Free-to-bound transition in β -SiC doped with boron. *Phys Stat Sol (a)* 30:739–746
167. Clemen LL, Devaty RP, MacMillan MF, Yoganathan M, Choyke WJ, Larkin DJ, Powell JA, Edmond JA, Kong HS (1993) Aluminum acceptor four particle bound exciton complex in 4H, 6H, and 3C SiC. *Appl Phys Lett* 62:2953–2955
168. Sridhara SG, Clemen LL, Devaty RP, Choyke WJ, Larkin DJ, Kong HS, Troffer T, Pensl G (1998) Photoluminescence and transport studies of boron in 4H SiC. *J Appl Phys* 83:7909–7919
169. Egilsson T, Bergman JP, Ivanov IG, Henry A, Janzén E (1999) Properties of the D_1 bound exciton in 4H-SiC. *Phys Rev B* 59:1956–1963
170. Lüth H (2010) Solid surfaces, interfaces and thin films, 5th edn. Springer, Berlin
171. Hara S, Misawa S, Yoshida S, Aoyagi Y (1994) Additional dimer-row structure of 3C-SiC(001) surfaces observed by scanning tunneling microscopy. *Phys Rev B* 50:4548–4553
172. Semond F, Soukiassian P, Mayne A, Dujardin G, Douillard L, Jaussaud C (1996) Atomic structure of the β -SiC(100)-(3 \times 2) surface. *Phys Rev Lett* 77:2013–2016
173. Sabisch M, Krüger P, Mazur A, Rohlfing M, Pollmann J (1996) First-principles calculations of β -SiC(001) surfaces. *Phys Rev B* 53:13121–13132
174. Soukiassian P, Semond F, Douillard L, Mayne A, Dujardin G, Pizzagalli L, Joachim C (1997) Direct observation of a β -SiC(100)-c(4 \times 2) surface reconstruction. *Phys Rev Lett* 78:907–910
175. Soukiassian P, Semond F, Mayne A, Dujardin G (1997) Highly stable Si atomic line formation on the β -SiC(100) surface. *Phys Rev Lett* 79:2498–2501

176. Derycke V, Soukiasian P, Mayne A, Dujardin G, Gautier J (1998) Carbon atomic chain formation on the β -SiC(100) surface by controlled $sp \rightarrow sp^3$ transformation. *Phys Rev Lett* 81:5868–5871
177. Powers JM, Wander A, Rous PJ, Van Hove MA, Somorjai GA (1991) Structural analysis of the β -SiC(100)- $c(2 \times 2)$ surface reconstruction by automated tensor low-energy electron diffraction. *Phys Rev B* 44:11159–11166
178. Yan H, Smith AP, Jónsson H (1995) Atomic structure of β -SiC(100) surfaces: an ab initio study. *Surf Sci* 330:265–275
179. Long JP, Bermudez VM, Ramaker DE (1996) Structural determination of β -SiC(100)- $c(2 \times 2)$ from C-1s surface-core-exciton and Si-2p absorption. *Phys Rev Lett* 76:991–994
180. Catellani A, Galli G, Gygi F (1996) Reconstruction and thermal stability of the cubic SiC (001) surfaces. *Phys Rev Lett* 77:5090–5093
181. Yeom HW, Shimomura M, Kitamura J, Hara S, Tono K, Matsuda I, Mun BS, Huff WAR, Kono S, Ohta T, Yoshida S, Okushi H, Kajimura K, Fadley CS (1999) Atomic and electronic-band structures of anomalous carbon dimers on 3C-SiC(001)- $c(2 \times 2)$. *Phys Rev Lett* 83:1640–1643
182. Starke U, Schardt J, Bernhardt J, Franke M, Reuter K, Wedler H, Heinz K, Furthmüller J, Käckell P, Bechstedt F (1998) Novel reconstruction mechanism for dangling-bond minimization: combined method surface structure determination of SiC(111)- (3×3) . *Phys Rev Lett* 80:758–761
183. Schardt J, Bernhardt J, Starke U, Heinz K (2000) Crystallography of the (3×3) surface reconstruction of 3C-SiC(111), 4H-SiC(0001), and 6H-SiC(0001) surfaces retrieved by low-energy electron diffraction. *Phys Rev B* 62:10335–10344
184. Kulakov MA, Henn G, Bullemer B (1996) SiC(0001) 3×3 -Si surface reconstruction—a new insight with a STM. *Surf Sci* 346:49–54
185. Li L, Tsong IST (1996) Atomic structures of 6H-SiC (0001) and $(000\bar{1})$ surfaces. *Surf Sci* 351:141–148
186. Starke U, Bram Ch, Steiner P-R, Hartner W, Hammer L, Heinz K, Müller K (1995) The (0001)-surface of 6H-SiC: morphology, composition and structure. *Appl Surf Sci* 89:175–185
187. Owman F, Mårtensson P (1995) STM study of the SiC(0001) $\sqrt{3} \times \sqrt{3}$ surface. *Surf Sci* 330:L639–L645
188. Northrup JE, Neugebauer J (1995) Theory of the adatom-induced reconstruction of the SiC(0001) $\sqrt{3} \times \sqrt{3}$ surface. *Phys Rev B* 52:R17001–R17004
189. Johansson LI, Owman F, Mårtensson P (1996) Surface state on the SiC(0001)- $(\sqrt{3} \times \sqrt{3})$ surface. *Surf Sci* 360:L478–L482
190. Johansson LI, Owman F, Mårtensson P (1996) High-resolution core-level study of 6H-SiC(0001). *Phys Rev B* 53:13793–13802
191. Sabisch M, Krüger P, Pollmann J (1997) Ab initio calculations of structural and electronic properties of 6H-SiC(0001) surfaces. *Phys Rev B* 55:10561–10570
192. Ramachandran V, Feenstra RM (1999) Scanning tunneling spectroscopy of Mott-Hubbard states on the 6H-SiC(0001) $\sqrt{3} \times \sqrt{3}$ Surface. *Phys Rev Lett* 82:1000–1003
193. Hornetz B, Michel H-J, Halbritter J (1994) ARXPS studies of SiO₂-SiC interfaces and oxidation of 6H SiC single crystal Si-(001) and C-($00\bar{1}$) surfaces. *J Mater Res* 9:3088–3094
194. Afanas'ev VV, Bassler M, Pensl G, Schulz MJ, von Kamienski ES (1996) Band offsets and electronic structure of SiC/SiO₂ interfaces. *J Appl Phys* 79:3108–3114
195. Afanas'ev VV, Bassler M, Pensl G, Schulz M (1997) Intrinsic SiC/SiO₂ interface states. *Phys Stat Sol (a)* 162:321–337
196. Afanas'ev VV, Stesmans A, Bassler M, Pensl G, Schulz MJ (2000) Shallow electron traps at the 4H-SiC/SiO₂ interface. *Appl Phys Lett* 76:336–337
197. Chang KC, Nuhfer NT, Porter LM, Wahab Q (2000) High-carbon concentrations at the silicon dioxide-silicon carbide interface identified by electron energy loss spectroscopy. *Appl Phys Lett* 77:2186–2188

198. Knaup JM, Deák P, Frauenheim T, Gali A, Hajnal Z, Choyke WJ (2005) Theoretical study of the mechanism of dry oxidation of 4H-SiC. *Phys Rev B* 71:235321
199. Pippel E, Woltersdorf J, Ólafsson HÓ, Sveinbjörnsson EÖ (2005) Interfaces between 4H-SiC and SiO₂: microstructure, nanochemistry, and near-interface traps. *J Appl Phys* 97:034302
200. Knaup JM, Deák P, Frauenheim Th, Gali A, Hajnal Z, Choyke WJ (2005) Defects in SiO₂ as the possible origin of near interface traps in the SiC/SiO₂ system: a systematic theoretical study. *Phys Rev B* 72:115323
201. Zheleva T, Lelis A, Duscher G, Liu F, Levin I, Das M (2008) Transition layers at the SiO₂/SiC interface. *Appl Phys Lett* 93:022108
202. Afanas'ev VV, Stesmans A, Bassler M, Pensl G, Schulz MJ, Harris CI (1996) Elimination of SiC/SiO₂ interface states by preoxidation ultraviolet-ozone cleaning. *Appl Phys Lett* 68:2141–2143
203. Afanas'ev VV, Stesmans A, Ciobanu F, Pensl G, Cheong KY, Dimitrijević S (2003) Mechanisms responsible for improvement of 4H-SiC/SiO₂ interface properties by nitridation. *Appl Phys Lett* 82:568–570
204. McDonald K, Weller RA, Pantelides ST, Feldman LC, Chung GY, Tin CC, Williams JR (2003) Characterization and modeling of the nitrogen passivation of interface traps in SiO₂/4H-SiC. *J Appl Phys* 93:2719–2722
205. Wang S, Dhar S, Wang S, Ahly AC, Franceschetti A, Williams JR, Feldman LC, Pantelides ST (2007) Bonding at the SiC–SiO₂ interface and the effects of nitrogen and hydrogen. *Phys Rev Lett* 98:026101
206. Deák P, Knaup JM, Hornos T, Thill C, Gali A, Frauenheim T (2007) The mechanism of defect creation and passivation at the SiC/SiO₂ interface. *J Phys D: Appl Phys* 40:6242–6253
207. Saks NS, Mani SS, Agarwal AK (2000) Interface trap profile near the band edges at the 4H-SiC/SiO₂ interface. *Appl Phys Lett* 76:2250–2252
208. Bernhardt J, Schardt J, Starke U, Heinz K (1999) Epitaxially ideal oxide-semiconductor interfaces: silicate adlayers on hexagonal (0001) and (000 $\bar{1}$) SiC surfaces. *Appl Phys Lett* 74:1084–1086
209. Ramachandran V, Brady MF, Smith AR, Feenstra RM, Greve DW (1998) Preparation of atomically flat surfaces on silicon carbide using hydrogen etching. *J Electron Mater* 27:308–312
210. Sieber N, Mantel BF, Seyller Th, Ristein J, Ley L, Heller T, Batchelor DR, Schmeißer D (2001) Electronic and chemical passivation of hexagonal 6H-SiC surfaces by hydrogen termination. *Appl Phys Lett* 78:1216–1218
211. Derycke V, Soukiassian PG, Amy F, Chabal YJ, D'angelo MD, Enriquez HB, Silly MG (2003) Nanochemistry at the atomic scale revealed in hydrogen-induced semiconductor surface metallization. *Nat Mater* 2:253–258
212. Cicero G, Catellani A, Galli G (2004) Atomic control of water interaction with biocompatible surfaces: the case of SiC(001). *Phys Rev Lett* 93:016102
213. Rosso M, Arafat A, Schroën K, Giesbers M, Roper CS, Maboudian R, Zuilhof H (2008) Covalent attachment of organic monolayers to silicon carbide surfaces. *Langmuir* 24:4007–4012
214. Rosso M, Giesbers M, Arafat A, Schroën K, Zuilhof H (2009) Covalently attached organic monolayers on SiC and Si_xN₄ surfaces: formation using UV light at room temperature. *Langmuir* 25:2172–2180
215. Catellani A, Calzolari A (2012) Functionalization of SiC(110) surfaces via porphyrin adsorption: ab initio results. *J Phys Chem C* 116:886–892
216. Schoell SJ, Sachsenhauser M, Oliveros A, Howgate J, Stutzmann M, Brandt MS, Frewin CL, Sadow SE, Sharp ID (2013) Organic functionalization of 3C-SiC surfaces. *ACS Appl Mater Interfaces* 5:1393–1399

217. Cheng C, Needs RJ, Heine V (1988) Inter-layer interactions and the origin of SiC polytypes. *J Phys C: Solid State Phys* 21:1049–1063
218. Heine V, Cheng C, Needs RJ (1991) The preference of silicon carbide for growth in the metastable cubic form. *J Am Ceram Soc* 74:2630–2633
219. Käckell P, Wenzien B, Bechstedt F (1994) Influence of atomic relaxations on the structural properties of SiC polytypes from *ab initio* calculations. *Phys Rev B* 50:17037–17046
220. Limpijumngong S, Lambrecht WRL (1998) Total energy differences between SiC polytypes revisited. *Phys Rev B* 57:12017–12022
221. Bernstein N, Gotsis HJ, Papaconstantopoulos DA, Mehl MJ (2005) Tight-binding calculations of the band structure and total energies of the various polytypes of silicon carbide. *Phys Rev B* 71:075203
222. Baumann HN (1952) The relationship of alpha and beta silicon carbide. *J Electrochem Soc* 99:109–114
223. Yoo WS, Matsunami H (1991) Solid-state phase transformation in cubic silicon carbide. *Jpn J Appl Phys* 30:545–553
224. Powell JA, Will HA (1972) Low-temperature solid-state phase transformations in 2H silicon carbide. *J Appl Phys* 43:1400–1408
225. Heuer AH, Fryburg GA, Ogbuji LU, Mitchell TE (1978) $\beta \rightarrow \alpha$ transformation in polycrystalline SiC: I, microstructural aspects. *J Am Ceram Soc* 61:406–412
226. Mitchell TE, Ogbuji LU, Heuer AH (1978) $\beta \rightarrow \alpha$ transformation in polycrystalline SiC: II, interfacial energetics. *J Am Ceram Soc* 61:412–413
227. Ogbuji LU, Mitchell TE, Heuer AH (1981) The $\beta \rightarrow \alpha$ transformation in polycrystalline SiC: III, the thickness of α plates. *J Am Ceram Soc* 64:91–99
228. Ogbuji LU, Mitchell TE, Heuer AH, Shinozaki S (1981) The $\beta \rightarrow \alpha$ transformation in polycrystalline SiC: IV, a comparison of conventionally sintered, hot-pressed, reaction-sintered, and chemically vapor-deposited samples. *J Am Ceram Soc* 64:100–105
229. Nader M, Aldinger F, Hoffmann MJ (1999) Influence of the α/β -SiC phase transformation on microstructural development and mechanical properties of liquid phase sintered silicon carbide. *J Mater Sci* 34:1197–1204
230. Starke U, Schardt J, Bernhardt J, Franke M, Heinz K (1999) Stacking transformation from hexagonal to cubic SiC induced by surface reconstruction: a seed for heterostructure growth. *Phys Rev Lett* 82:2107–2110
231. Okojie RS, Xhang M, Pirouz P, Tumakha S, Jessen G, Brillson LJ (2001) Observation of 4H-SiC to 3C-SiC polytypic transformation during oxidation. *Appl Phys Lett* 79:3056–3058
232. Chang KJ, Cohen ML (1987) *Ab initio* pseudopotential study of structural and high-pressure properties of SiC. *Phys Rev B* 35:8196–8201
233. Yoshida M, Onodera A, Ueno M, Takemura K, Shimomura O (1993) Pressure-induced phase transition in SiC. *Phys Rev B* 48:10587–10590
234. Karch K, Bechstedt F, Pavone P, Strauch D (1996) Pressure-dependent properties of SiC polytypes. *Phys Rev B* 53:13400–13413
235. Shimojo F, Ebbsjö I, Kalia RK, Nakano A, Rino JP, Vashishta P (2000) Molecular dynamics simulation of structural transformation in silicon carbide under pressure. *Phys Rev Lett* 84:3338–3341
236. Miao MS, Lambrecht WRL (2003) Unified path for high-pressure transitions of SiC polytypes to the rocksalt structure. *Phys Rev B* 68:092103
237. Vashishta P, Kalia RK, Nakano A, Rino JP (2007) Interaction potential for silicon carbide: a molecular dynamics study of elastic constants and vibrational density of states for crystalline and amorphous silicon carbide. *J Appl Phys* 101:103515
238. Aristov VYu, Douillard L, Fauchoux O, Soukiassian P (1997) Temperature-induced semiconducting $c(4 \times 2) \rightleftharpoons$ metallic (2×1) reversible phase transition on the β -SiC(100) surface. *Phys Rev Lett* 79:3700–3703

Silicon Carbide Nanostructures
Fabrication, Structure, and Properties
Fan, J.; Chu, P.K.-H.
2014, IX, 330 p. 355 illus., Hardcover
ISBN: 978-3-319-08725-2